Graz University of Technology

Romuald Franklin Ngamga

Electrochemical reaction of the Zn/Zincate/ZnO System

(Application in rechargeable alkaline batteries)

DISSERTATION

Thesis submitted in partial fulfillment of requirements for the degree of

Doctor of Engineering Sciences

Ao.Univ.-Prof. Dipl.-Ing. Dr.techn. Leo Binder

Institute of Inorganic Chemistry, Graz University of Technology, Austria

(*Sponsored by Revolt Technology AS*)

November 2011

TU Graz
Graz University of Technology

Deutsche Fassung:
Beschluss der Curricula-Kommission für Bachelor-, Master- und Diplomstudien vom 10.11.2008
Genehmigung des Senates am 1.12.2008

EIDESSTATTLICHE ERKLÄRUNG

Ich erkläre an Eides statt, dass ich die vorliegende Arbeit selbstständig verfasst, andere als die angegebenen Quellen/Hilfsmittel nicht benutzt, und die den benutzten Quellen wörtlich und inhaltlich entnommene Stellen als solche kenntlich gemacht habe.

Graz, am …………………………… ………………………………………………..
(Unterschrift)

Englische Fassung:

STATUTORY DECLARATION

I declare that I have authored this thesis independently, that I have not used other than the declared sources / resources, and that I have explicitly marked all material which has been quoted either literally or by content from the used sources.

…………………………… ………………………………………………..
date (signature)

Acknowledgments

This work was carried out at the Department of Inorganic Chemistry in the period from October 2008 to January 2012, under the supervision of Prof. Leo Binder and co-supervision of Dr. Trygve Burchardt. The latter is CSO and founder of Revolt Technology AS, my employer. It was a privilege to be allowed to pursue my PhD education while working fulltime for the company. I am humbled and I thank GOD for giving me such an opportunity.

I would like to acknowledge the advice and guidance of Pr. Leo Binder. His outstanding aptitude to convey knowledge and his suggestions always spot-on were indispensable. Pr. Leo Binder is now retiring and it is an honor for me to write with this thesis the last chapter of his rich and remarkable life career.

I owe my deepest gratitude to Dr. Trygve Burchardt for his constant support and recommendations for the realization of this project. Special thanks go to Prof. Fruhwirth Otto, Prof. Taucher-Mautner Waltraud and Prof. Bernhard Gollas for the fruitful discussions that helped me understand some key elements of batteries at a fundamental level.

I am profoundly grateful to Revolt Technology AS for its financial support and for providing the major experiment materials and equipments for this project. I am indebted to my colleagues and managers for their encouragement and consideration during the period of the program. I also would like to thank all fellow students of my research group at TUGraz and those who supported me in any respect during the completion of the project.

Finally, I am heartily thankful to my parents and to my wife, Kiumi Nam, for their prayers. I would not have completed the degree without my wife’s care and patience.

Summary

Study of some characteristics of the electrochemical reaction of the Zn-Zincates-ZnO system in alkaline solution has been carried out in this work within the scope of application in batteries. The most important findings are presented here.

- Half-cell as well as full cell setups were designed and used to demonstrate the effect of some well-known phenomena associated with the rechargeability of zinc electrodes in alkaline solutions. The impact of the discharge and charge on the alloys such as Pb and In, two metals used to suppress the corrosion of zinc, was examined and their instability was ascertained. It was found that while Pb tends to dissolve during the discharge and does not replenish during the charge, In hardly goes into the solution. Assuring a homogeneous redistribution of the alloys across the surface upon subsequent cycles is a major challenge.

- A simple method was developed to investigate the inefficiency of the zinc electrodeposition onto a copper substrate, a metal generally used for the current collection. The method proved to give out a quite good mechanistic explanation of the reaction by revealing some key aspects of the zinc recrystallization. A different technique was used in parallel to consolidate the findings. The efficiency of the zinc electrodeposition depends on the current density. At very low current densities the hydrogen overpotential of copper predominates as zinc crystal fails to rapidly grow. The hydrogen overpotential of zinc accounts for the reaction inefficiency at high drain rates.

- The inhibiting effect of indium on the electrode corrosion was assessed. It was found that the corrosion rate of the zinc electrode can be tremendously reduced without causing appreciable increase in the cell internal impedance by coating the copper current collector with indium. However, the thickness of the protective indium-film ought to be optimized in the case of rechargeable electrodes as indium tends to oxidize

with repeated cycles. Indium being a rather expensive metal, its use in battery should be kept to minimum.

- The impact of $In(OH)_3$ on the zinc reaction kinetics in 7M KOH solution was studied. $In(OH)_3$ significantly diminishes the corrosion rate of zinc electrode and has a positive impact on the charge transfer constant of the electrodeposition reaction. An optimal concentration somewhere in the range from $2.4x10^{-3}$M to $3.0x10^{-3}$M was suggested and it was argued to be the solubility limitation. These effects were attributed to the surface modification of the zinc electrode in presence of $In(OH)_3$.

- Sonication was used to characterize in-situ the growth of the oxide film responsible for the passivation of zinc in alkaline solution. The investigation proved that both the duration and the potential have an effect on the passive film structure and growth. The method was also used to demonstrate the formation sequences of the different oxide layers during the process of the surface passivation. Further study showed that the impact of the passive film on the electrodeposition reaction of zinc in highly concentrated KOH solutions is not significant. However, the effect may be enhanced in batteries where drop in the performance was observed.

Contents

Acknowledgment **v**

Summary **vii**

List of Tables **xiii**

List of Figures **xv**

Nomenclature **xxi**

1 Introduction 1
- 1.1 Background 1
- 1.2 History of alkaline rechargeable zinc cells 2
  - 1.2.1 Zinc-nickel oxide cell 3
  - 1.2.2 Zinc-silver oxide cell 4
  - 1.2.3 Rechargeable zinc-air cell 6
  - 1.2.4 Rechargeable alkaline manganese oxide cell 8

2 Review of the failure mechanisms 11
- 2.1 Hydrogen evolution reaction 11
  - 2.1.1 Zinc corrosion 12
  - 2.1.2 Zinc hydrogen overpotential 15
  - 2.1.3 Galvanic coupling 17
  - 2.1.4 Effect of KOH concentration on the HER of zinc electrode 20
  - 2.1.5 Hydrogen recombination catalyst 21
- 2.2 Passivation 22
  - 2.2.1 Theory 22
  - 2.2.2 Discussion 24
- 2.3 Shape change 25
  - 2.3.1 Theory 25
  - 2.3.2 Discussion 28
- 2.4 Dendrite formation 31
  - 2.4.1 Theory 31
  - 2.4.2 Discussion 34

3 Experimental 37
- 3.1 Chemicals and apparatus 37
  - 3.1.1 Button cell 37

3.1.2 Electrochemical cell setup 38
3.1.3 Zinc half-cell setup 39
3.2 Electrochemical measurement 39
3.2.1 Steady state polarization 40
3.2.2 Cyclic voltammetry 41
3.2.3 AC impedance 42
3.2.4 Quartz crystal microbalance 46

4 Zinc alloys stability in rechargeable electrodes 49
4.1 Introduction 50
4.2 Experimental 50
4.3 Result and discussion 51
4.3.1 Surface analysis 52
4.3.2 Electrolyte analysis 54
4.4 Summary 55

5 Hydrogen Overpotential during the zinc electrodeposition on copper 57
5.1 Introduction 58
5.2 Experimental 59
5.2.1 Electrode and cell preparation 59
5.2.2 Polarization techniques 59
5.2.3 Electrochemical quartz microbalance 60
5.2.4 Electrochemical Impedance Spectroscopy 60
5.3 Result and discussion 60
5.4 Summary 69

6 Study of the stability and effect of indium coat on the zinc reaction 71
6.1 Introduction 72
6.2 Experimental 72
6.2.1 Preparation of the porous zinc paste and electrode 72
6.2.2 Gas volumetric measurement in vessel 73
6.2.3 Investigation of gassing in rechargeable zinc-air cell 73
6.2.4 Qualitative and semi-qualitative analysis 73
6.2.5 Measurement of the electrochemical performances 74
6.3 Result and discussion 74
6.3.1 Corrosion test 74
6.3.2 Cyclic voltammetry 76
6.3.3 Electrochemical performance 78
6.3.4 Surface analysis 82
6.4 Summary 83

7 $In(OH)_3$ effect on zinc reaction in concentrated KOH solution 85
7.1 Introduction 86

7.2 Experimental 86
    7.2.1 Corrosion test 86
    7.2.2 Cyclic voltammetry 87
    7.2.3 AC. Impedance technique 87
7.3 Result and discussion 87
    7.3.1 Zinc corrosion 87
    7.3.2 Cyclic voltammetry 89
    7.3.3 Electrochemical impedance analysis 94
7.4 Summary 96

8 Characterization of zinc passive film by sonication in 7M KOH solution 97
8.1 Introduction 98
8.2 Experimental 99
    8.2.1 Material preparation 99
    8.2.2 Apparatus 99
    8.2.3 Electrochemical measurement 100
    8.2.4 Surface characterization 100
8.3 Result and discussion 100
    8.3.1 Effect of sonication on the surface passivity 100
    8.3.2 Characterization of the passive film growth 104
    8.3.3 Investigation of the potential effect on the oxide layer structure 105
8.4 Summary 106

9 Impact of the passivation on the zinc electrode charge performance 107
9.1 Introduction 108
9.2 Experimental 108
    9.2.1 Material preparation 108
    9.2.2 Apparatus 109
    9.2.3 Electrical performance measurement 109
9.3 Result and discussion 109
    9.3.1 Discharge voltage sweep analysis 109
    9.3.2 Effect of the passive film on the electrodeposition kinetics 110
    9.3.3 Effect of the passive film thickness on the electrodeposition potential 113
    9.3.4 Effect of the passivation on the charge voltage of the 675 button cell 115
9.4 Summary 116

10 Conclusion 117

Bibliography 121

List of Tables

1.1 Rechargeable nickel zinc battery characteristics. 4

1.2 Rechargeable silver oxide zinc battery characteristics. 6

1.3 Rechargeable zinc-air battery characteristics. 7

1.4 Rechargeable alkaline manganese dioxide battery characteristics. 9

2.1 Tafel slopes and exchange current densities for hydrogen reduction on zinc in aqueous solutions [32]. 17

2.2 Overvoltage during the electrodeposition reaction. 33

2.3 Basic requirements for battery separators, from Cook et al. 36

3.1 Criteria for reversible reactions without diffusion limitations. 42

3.2 Equivalent circuit elements. 44

4.1 Table summary of the results from the ICPMS analysis of indium and lead alloys in the zinc mass and electrolyte. 54

6.1 Life time of the fresh and cycled button cells under the conditions of 70°C and 50%RH. 75

7.1 Anodic and cathodic characteristics of charge-transfer constant (k_{ct}) and the diffusion controlled constant (k_{diff}) of the cyclic voltammogram for ZnO in 7M KOH and in 7M KOH + 3.10-3 M $In(OH)_3$. 94

7.2 Values of the electrical circuit components to fit the impedance spectra of the zinc deposition in 7M KOH. 95

9.1 Current density peak and overvoltage performances summary. 112

List of Figures

1.1 Comparison of energy densities for various battery technologies. 2

1.2 Cut-away view of Nickel-Zinc battery (Source: Evyonix Corp.). 4

1.3 Schematic representation of species involved in the nickel-zinc reaction. 4

1.4 Cross sectional view of a silver-zinc battery (source: Battery Association of Japan). 5

1.5 Exploded view of prismatic zinc-air battery (Source: Revolt Technology LLC). 7

1.6 Schematic representation of species involved in the zinc-air reaction (source: Revolt technology LLC). 7

1.7 Cut-away view of an alkaline manganese dioxide cell. 9

2.1 Volcano-type correlation of catalytic activity of different metals and the M-H binding energy [16]. 12

2.2 Comparison plot of the hydrogen evolution rate between fine (1) and coarse (2) zinc powder fractions. 14

2.3 Hydrogen overpotential on Zn in 6M KOH; After Lee [31]. 16

2.4 Surface of the copper mesh screen before (left) and after (right) contacting with a zinc paste. 18

2.5 Hydrogen evolution rate as a function of time of the zinc paste solely (1) and zinc electrode (2) in 7M KOH solution. Test performed at 70°C. 19

2.6 Area of a copper current collector of a rechargeable zinc electrode where the spontaneous zinc film deposit was stripped off upon repeated cycles. Source: Revolt Technology LLC. 20

2.7 Variation of the hydrogen evolution rate as a function of time of a zinc electrode in 2, 7 and 11M KOH solutions at 70°C. 21

2.8 Schematic illustration of the films formed on zinc electrodes in 7M KOH under different convection conditions. After Powers [44]. 23

2.9 Proposed scheme for the processes associated with the anodic passivation of zinc in alkaline solutions. After Liu et al. [46]. 23

2.10 Variation of the specific capacity of zinc electrode in KOH solutions with current density and KOH concentration: (●) 2M KOH; (o) 6M KOH; (∆) 11M KOH (Source: Revolt technology LLC). 25

2.11 Morphology of prismatic zinc electrode after the 5th cycle (left) and 80th cycle (right) at 50% depth of discharge (source: Revolt Technology LLC.). 26

2.12 Distribution of local charge transfer current, j (mA/cm^2), for type I membrane boundary (I = 50mA/cm^2, L = 0.1cm, and A, B, C and D represent 0%, 10%, 20%, and 40% depth of discharge, respectively) [56]. 27

2.13 Distribution of Zn and ZnO as volume fraction (left) for type I membrane and (right) for solution boundary (I = 50mA/cm^2, and A, B, C and D represent 0%, 10%, 20%, and 40% depth of discharge, respectively) [56]. 28

84 Distribution of Zn and ZnO as volume fractions during two cycles for type I membrane (I = 50mA/cm^2, L = 0.1cm) [56]. 29

2.15 Variation of the capacity of a zinc-air cell with cycle number and depth of discharge at 0.8V cutoff voltage. Source: Revolt Technology LLC. 30

2.16 Migration of hydrated metal ions to a cathode, surrender of the hydration sheath, formation of ad-atoms, and formation of crystal nuclei at the cathode surface [70]. . . . 32

3.1 Cutaway view of a zinc-air button cell. 38

9 Three-electrode electrochemical cell. 38

3.3 Half-cell setup for the porous zinc electrode: (a) PVC test vehicle; (b) complete test setup. 39

3.4 Complex plan plot. 43

105 Sinus variation of E and I as a function of time. 43

116 Randles equivalent circuit model. 44

3.7 Nyquist plot. 45

12 Bode plot. 45

3.9 Quartz crystal microbalance apparatus. 48

3.10 Components of the quartz crystal holder. 48

4.1 Zinc particle morphology. 51

4.2 Incrusted In and Pb precipitates in the grain boundaries of zinc particle. 51

133 EDX spectrum for specimen consisting of zinc powder alloyed with In and Pb. Index: (a) grain boundary (b) center of grain. 52

4.4 SEM picture of zinc after a full discharge of the cell: (1) etched surface, (2) porous and flocculent zinc oxide, (3) layered structure of particle. 53

4.5 EDX analysis of the zinc discharge product: (a) zinc oxide, (b) alloy precipiates. 53

4.6 Morphology of the zinc deposits in charge. 54

4.7 SEM picture of the surface of freshly deposited zinc in charge. 54

5.1 Electrochemical performance at 50mV overpotential, (a) Voltage and current curve variation, (b) capacity variation as a function of the test time. 61

5.2 Electrochemical performance at 300mV overpotential, (a) Voltage and current curve variation, (b) capacity variation as a function of the test time. 61

5.3 Tafel polarization curve for the HER during the Zn electrodepositon on copper in 7MKOH solution containing 0.25M ZnO at 24°C. 62

14 Tafel polarization curve for HER on copper substrate in 7M KOH solution at 24°C. 62

15 Tafel polarization curve comparison between the hydrogen overpotential on Cu surface in 7M KOH solution and that during the Zn electrodepositon on copper in 7MKOH solution containing 0.25M ZnO at 24°C. 63

5.6 Variation of the resonance frequency and deposited mass on the EQCM quartz crystal at 0.2mA/cm2 (a) and 6mA/cm2 (b) deposition rate. 65

16 Efficiency curve of the Zn electrodeposition on a 5MHz-QCM crystal in 7MKOH containing 0.25M ZnO at 24°C. 66

5.8 Zinc crystal surface coverage variation on a copper substrate as a function of the overpotential in 7M KOH solution containing 0.25M dissolved ZnO at 24°C. 68

6.1 Corrosion of zinc paste rolled within a copper mesh with and without an indium coat in 7M KOH solution. 73

6.2 Bare anode cup (right) and indium-plated anode cup (left). 75

6.3 Cyclic voltammogram of indium in 7M KOH; scan rate = 100mVs^{-1}; between 0 and 950mV vs. Zn RE. 76

6.4 Cyclic voltammogram of ZnO in 7M KOH; scan rate = 100mVs^{-1}; between -200 and 500mV vs. Zn RE. 77

6.5 Charge voltage variation with time and cycle number of rechargeable button cell comprising a bare copper cup and indium plated cup for the anode. 79

176 Discharge and charge voltage variation as a function of time at 15mA/cm2 of button cell with the bare anode cup. 80

6.7 Discharge and charge voltage variation as a function of time at 15mA/cm2 of button cell with indium-plated anode cup. 80

18.8 Steady state polarization curve of zinc-air 675 button cell: (o) with indium plated anode cup; (●) with bare anode cup. 81

6.9 Steady state polarization curve of zinc-air 675 button cell with indium plated anode cup: (o) fresh anode cup; (●) cycled anode cup. 81

6.10 Surface morphology of anode cup of zinc-air 675 button cell cycled 10 times: (A-B) with bare anode cup; (B) with indium-plated anode cup. 82

6.11 SEM image of the cross-section of freshly indium-plated anode cup of zinc-air 675 button cell. 83

6.12 SEM image (left) and EDS analysis (right) of the cross-section of cycled zinc air 675 button cell with indium-plated anode cup. 83

19 Dependence of zinc electrode hydrogen evolution rate with time in 7M KOH with and without indate additives. Index: Plain 7M KOH (1), plain + 0.6x10^{-3} M (2), plain + 1.2x10^{-3} M (3), plain + 1.8x10^{-3} M (4), plain + 2.4x10^{-3} M (5), plain + 3.0x10^{-3} M (6); at 70°C and 50%RH. 88

20 Variation of the zinc electrode hydrogen evolution rate with indate concentration after 180 hours of storage at 70°C and 50%RH. 88

21 Cyclic voltammogram of ZnO in 7M KOH with and without indate additives. Index: Plain 7M KOH (1), plain + 0.6x10^{-3} M (2), plain + 1.2x10^{-3} M (3), plain + 1.8x10^{-3} M (4), plain + 2.4x10^{-3} M (5), plain + 3.0x10^{-3} M (6); scan rate = 10mVs^{-1}; between -200 and 500mV vs. Zn RE at 25°C. 90

22 Effect of the indate concentration on the anodic (——) and cathodic (----) potential peaks of the cyclic voltammogram for ZnO in 7M KOH at 25°C. 90

23 Effect of the indate concentration on the anodic peak current of the cyclic voltammogram of ZnO in 7M KOH at 25°C. 91

24 Effect of the indate concentration on the cathodic peak current of the cyclic voltammogram of ZnO in 7M KOH at 25°C. 91

25 Cyclic voltammogram in 7M KOH with and without indate additives. Index: Plain 7M KOH (1), plain + 3.0x10^{-3} M (2); scan rate = 10mVs^{-1}; between -200 and 500mV vs. Zn RE. 93

26 Cyclic voltammogram of ZnO at various scan rates; between -200 and 500mV Vs Zn RE at 25°C. Index: (1)10mVs^{-1}, (2) 20mVs^{-1}, (3) 50mVs^{-1}, (4) 100mVs^{-1}; (a) in 7M KOH and (b) in 7M KOH + 3.10^{-3} M $In(OH)_3$. 93

27 Plot of anodic and cathodic peak currents i_p vs. $v^{1/2}$ for ZnO in 7M KOH and in 7MKOH + 3.0x10^{-3} M $In(OH)_3$ at 25°C; anodic (——) and cathodic sweep (----).. 94

28 Complex impedance spectra (Nyquist plot) of the zincate reduction in 7M KOH with and without indate additives; between 0.1 and 1MHz at 20mA cathodic current and 10mA AC amplitude at 25°C. 95

29 Effect of the indate concentration on solution resistance Rs (----) and the charge transfer resistance R_{ct} (——) of the impedance spectroscopy of zincate reduction in 7M KOH at 25°C. 96

8.1 Polarization curve of zinc in 7M KOH in silent and irradiated conditions. 101

8.2 SEM micrograph and EDS Spectrum of zinc surface polarized at 350mV constant voltage for 5min under silent conditions. 102

30 SEM micrograph and EDS Spectrum of zinc surface polarized at 350mV constant voltage for 5min under irradiation conditions. 103

8.4 SEM micrographs of the cavities on the zinc after an anodic polarization at 350mV constant voltage for 5 min: (a) under silent conditions; (b) under ultrasound irradiation 103

8.5 Current spectrum of zinc electrodes at a passive potential of 400mV under sonication conditions (40 KHz). Prior to the sonication exposure, the electrode surfaces were passivated for: 60, 120, 300 and 600s. 104

31.6 Current spectrum of zinc electrodes at various passive potentials (350, 400, 450 and 500mV) under sonication conditions (40 KHz). Prior to the sonication exposure, the electrode surfaces were passivated for 300s. 105

9.1 I-E curve of zinc electrode in KOH solution in various concentrations. 110

9.2 Current density variation as a function of time of the zinc plate electrode anodically polarized at 100mV and 400mV overpotential in 6M KOH. 111

323 Surface morphology of the zinc plate before (a) and after (b) the anodic polarization at 100mV overpotential in 6M KOH. 111

9.4 I-E curve of cathodic polarization sweep in zincate-saturated 2M KOH at $5mV.s^{-1}$ scan rate. 111

9.5 I-E curve of cathodic polarization sweep in zincate-saturated 6M KOH at $5mV.s^{-1}$ scan rate. 112

9.6 I-E curve of cathodic polarization sweep in zincate-saturated 11M KOH at $5mV.s^{-1}$ scan rate. 112

9.7 I-E curve of the cathodic polarization sweep of the zinc electrodes of various discharge states in zincate-saturated 11M KOH. 114

9.8 Variation of the peak current density I_p and overvoltage η (at $45mA/cm^2$) as a function of the discharge capacity of the zinc electrode. 114

9.9 Plot of the charge current density peak I_p vs. $v^{-1/2}$ of zinc electrodes with passive and active surface in 11M KOH saturated with zincates. 115

9.10 Charge potential curve of zinc-air 675 button cells discharged at a constant potential of 0.5V (1) and at a constant drain rate of $15mA.cm^{-2}$ (2). The charge current density is $15mA.cm^{-2}$ and the discharge capacity is 20mAh. 116

Nomenclature

List of Symbols

A	Surface area	m^2
b	Tafel slope	$mV.dec^{-1}$
C	Capacitance	F
D	Diffusion coefficient	$m^2.s^{-1}$
f	Frequency	Hz
F	Faraday's constant	$96500C.mol^{-1}$
E_a	Activation Energy in Arrhenius equation	$kJ.mol^{-1}$
i_o	Exchange current density	$A.cm^{-2}$
i	Applied current density	$A.cm^{-2}$
Jo	Exchange current density	$A.cm^{-2}$
k	Reaction rate constant	various
L	Inductance	H
k	Boltzmann's constant	$eV.K^{-1}$
N_k	Rate of crystal nucleation	various
Q	Quantity of electricity	C
R	Universal gas constant	$8.314J.(mol.K)^{-1}$
r*	Critical radius of the crystal nucleus	m
R	Ohmic resistance	Ω
t	Time	s
T	Temperature (degrees Kelvin)	K
W	Warburg coefficient	$\Omega.s^{-0.5}$
Z	Impedance	Ω
z	Number of transferred electrons	-
α	Symmetric factor for the charge transfer	-
α	Coefficient of the CPE	-
γ	Surface energy	J
δ	Diffusion layer	m

Δm	Mass change	$g.cm^{-2}$
Δg	Gibbs energy	J
$\Delta G*$	Critical free energy needed corresponding to that of the critical radius	J
η	Overpotential	V
μ_q	Shear modulus of quartz	GPa
ν	Potential scan rate	$mV.s^{-1}$
ω	Angular frequency	$rad.s^{-1}$
ρ_q	Density of the quartz	$g.cc^{-1}$
θ	Phase angle	rad
θ	Surface coverage	-

Acronyms

CPE	Constant phase element
DoD	Depth of discharge
EDS	Energy dispersive X-ray scanner
EQCM	Electrochemical quartz crystal microbalance
HER	Hydrogen evolution reaction
RH	Relative humidity
SEM	Scanning electron microscope

Chapter 1

Introduction

1.1 Background

In general, zinc is widely used in multiple applied fields such as electronics (its oxide displays n-type characteristics), mechanic (die casting), electrochemistry (anti-corrosion coating and batteries), metallurgy (brass production), Pharmaceutical and cosmetic, etc…

The use of zinc in the field of electrochemistry has always been of particular interest as it is a preferred anode material for high energy density batteries and sacrificial electrodes to protect other metallic components against the corrosion.

Besides their high energy density, batteries using zinc anodes in alkaline mediums have received considerable research attention because of zinc low cost, ease of handling, non-toxicity and abundance. Zinc ranks fourth among the metals in worldwide production and consumption [1].

Most of alkaline zinc batteries are primarily non-rechargeable (e.g., MnO2/Zn, Zn/air, Ag/Zn, etc…). The non flammability of the alkaline medium makes these batteries intrinsically safe. The zinc-manganese dioxide battery is the most commercialized of all zinc cells. It remains a dominant product in the consumer battery markets, and its world average annual growth rate was estimated at 5-8% in 2006 [2], while zinc-air has the particularity to deliver the highest energy density of any commercially available system.

In the past decades, substantial efforts have been devoted in exploring and developing electrically rechargeable zinc cells in order to respond to the increasing demand in energy consumption in the fast-growing market of electronic devices and automotive industry. But so far, despite the progress made in material science and cell design over the years, only a little success has been achieved in developing a system that is capable to replace other commercial rechargeable batteries.

The emergence of secondary zinc batteries has partly been slowed down by the lack of successfully overcoming the inherent problems associated with the zinc anode. In fact, rechargeable zinc anodes generally face poor cycle life. Upon subsequent charge and discharge cycles, the uncontrolled electrochemical dissolution and deposition of zinc proceed non-uniformly on the surface and in the bulk of the electrode, resulting in some structural shape change, capacity loss, dendrite formation and undesirable gassing. Thus, most activities related to rechargeable zinc battery systems remain under development.

1.2 History of alkaline rechargeable zinc cell

Rechargeable zinc cells can be used for the storage of electrical energy for applications that range from portable consumer electronic devices to bulk electricity storage at power stations and electric transportation. The main alkaline zinc cell types are described in this section, including some of the important features that characterize their chemistries. The gravimetric and volumetric energy densities of some of these batteries make them very competitive compared to other systems, as illustrated in Figure 1.1.

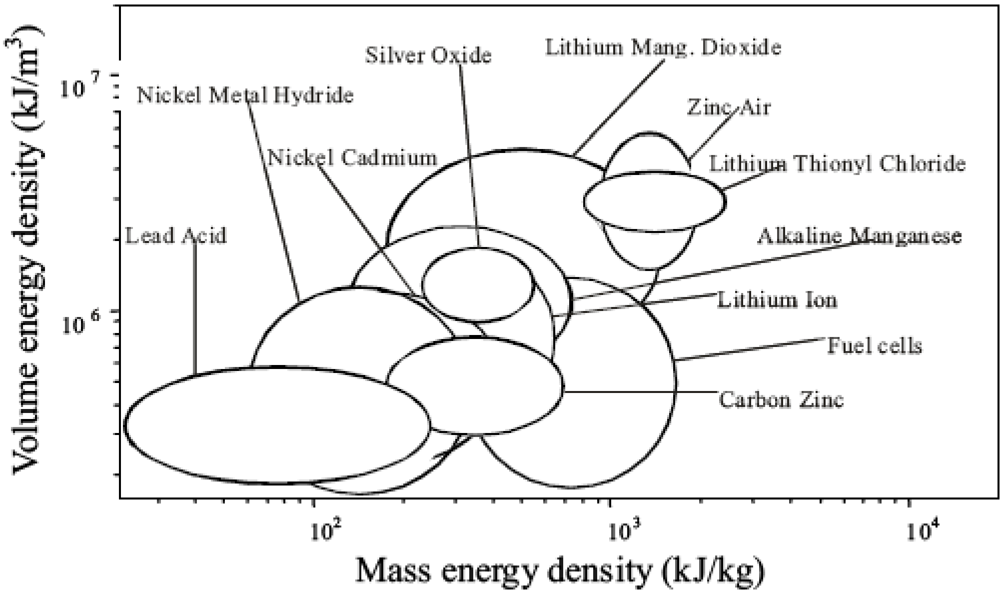

Figure 1.33: Comparison of energy densities for various battery technologies.

1.2.1 Zinc-nickel oxide cell

a. Historical

The first work on Ni-Zn dates back at least to 1887 when Dun & Haslacher [3] patented a number of systems based on nickel-potassium hydroxide batteries. A Russian patent by Michaelowski reports early NiZn development work in the late 1890s, too. In the early 20th century the Swedish Waldemar and the American Thomas Alva Edison investigated the secondary Ni/Zn system, but no commercial product emerged [4]. Since then research into Ni-Zn has been cyclic with some findings in advanced materials that led to the production of large and small format cells. The system development has been plagued for many years by the limited cycle life associated with the zinc electrode. In more recent years, various types of battery design and construction have been developed to power devices such as electric bicycles, electric lawn and garden equipment and electric scooters. To date, NiZn batteries are produced by several companies around the globe among which PowerGenix, Evercel, Evyonix and SCPS are the major players. The cell characteristics are shown in Table 1.1.

b. Chemistry

NiZn battery system uses the nickel-hydroxide/ nickel-oxyhydroxide electrode as the cathode and a porous zinc/zinc oxide as the anode with an incorporated filling and venting cap, as shown in Figure 1.2. During the discharge, nickel(III)-oxyhydroxide is reduced to nickel(II)-hydroxide, while metallic zinc is oxidized to zinc(II) oxide, and the reverse reaction takes place during the charge. Figure 1.3 illustrates the different reactions. The simplified electrochemical reactions are as follows:

Anode: $Zn + 4OH^{-} \leftrightarrow Zn(OH)_4^{2-} + 2e^{-}$ ($E_0 = 1.24$ V) (1.1)
$Zn(OH)_4^{2-} \leftrightarrow ZnO + H_2O + 2OH^{-}$

Cathode: $2NiOOH + 2H_2O + 2e^{-} \leftrightarrow 2Ni(OH)_2 + 2OH^{-}$ ($E_0 = 0.49$ V) (1.2)

Overall: $Zn + 2NiOOH + H_2O \leftrightarrow 2Ni(OH)_2 + ZnO$ ($E_0 = 1.73$ V) (1.3)

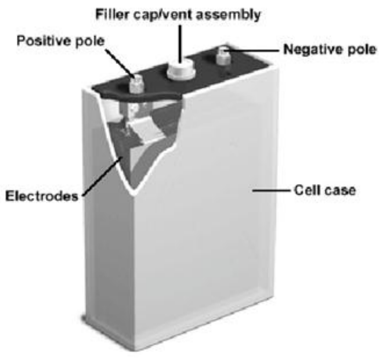

Figure 1.34: Cut-away view of Nickel-Zinc battery (Source: Evyonix Corp.).

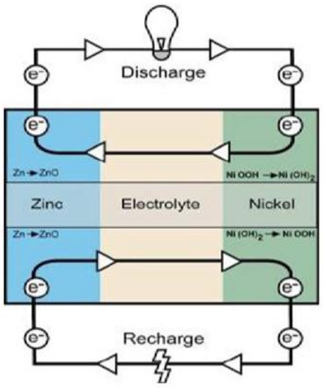

Figure 1.35: Schematic representation of species involved in the nickel-zinc reaction.

Advantages	Disadvantages
- Good specific energy ranging from 80 to 100Wh.kg-1	- Relatively low volumetric energy density (80 to 120 Wh.L^{-1}).
- Fast recharge capability	- High cost of nickel
- Low environmental impact Abundant raw material	
- Good cycle life (500 cycles at 100% DoD)	

Table 1.1: Rechargeable nickel zinc battery characteristics.

1.2.2 Zinc-silver oxide cell

a. Historical

Volta introduced the first silver battery using zinc as an anode in 1800 [5]. These batteries were of the primary type and they dominated the scene in the early nineteenth century. It is only in the late 1880s that Jungner reported the first workable secondary silver battery using other metal than zinc though (cadmium, iron) [6]. However, these batteries became commercially unattractive due to their short cycle life and high cost. A breakthrough was made in 1941 by a French professor Henri Andre as he provided the solution to the practical rechargeable silver-zinc cells [7, 8] based on the use of semipermeable membrane-cellophane as a separator. The membrane-cellophane proved to retard the migration of the soluble silver oxide to the anodic electrode and also impeded the formation of zinc dendrites, the major causes of cell failures.

Rechargeable silver-zinc batteries were first commercialized by Yardney International Corporation [9]. Despite the attractive characteristics exhibited by silver-zinc batteries, as shown in Table 1.2, the high cost of the silver electrode has limited their use to applications where high specific energy or power density are needed, such as torpedoes, submarines and space applications, portable industrial instrumentation and medical instrumentation. ZPower, RBS Technologies and SAFT are among the largest companies producing silver-zinc batteries.

b. Chemistry

The silver-zinc battery positive electrodes are made with divalent (AgO) or monovalent silver oxide (Ag_2O) and the negative electrodes are mostly made of metallic zinc. Figure 1.4 shows the stack composition of a silver-zinc typical cell. The silver oxide electrode can undergo up to two reductions which is characterized by two discrete steps in the charge and discharge curves. The different reactions at the electrodes in the silver-zinc system can be summarized as follows:

Anode: $Zn + 4OH^- \leftrightarrow Zn(OH)_4^{2-} + 2e^-$ ($E_0 = 1.25$ V) (1.1)
$Zn(OH)_4^{2-} \leftrightarrow ZnO + H_2O + 2OH^-$

Cathode: $2AgO + H_2O + 2e- \leftrightarrow Ag_2O + 2OH^-$ (1.4)
$Ag_2O + H_2O + 2e- \leftrightarrow 2Ag + 2OH^-$
Overall: $AgO + Zn \leftrightarrow Ag + ZnO$ (1.5)

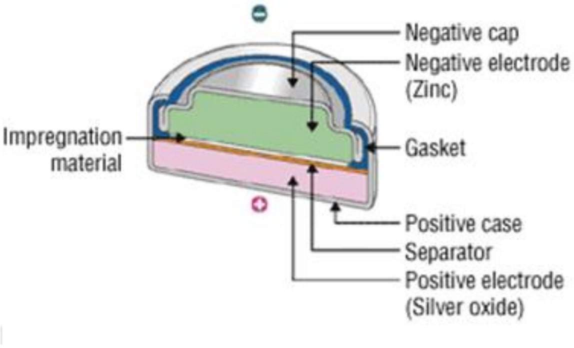

Figure 1.36: Cross sectional view of a silver-zinc battery (source: Battery Association of Japan).

Advantages	Disadvantages
High energy density (300 to 500 Wh.L^{-1}) High specific energy (100 to 130 Wh.kg^{-1}) Good charge retention Low maintenance Low self-discharge Inherently safe flat discharge voltage curve	High cost Relatively low cycle life (10 to 250 deep cycles) Sensitivity to overcharge Decreased performance at low temperature

Table 1.2: Rechargeable silver oxide zinc battery characteristics.

1.2.3 Rechargeable zinc-air cell

a. Historical

The effect of oxygen as a fuel was first observed in the early 19th century. Battery products made on this principle were commercialized in the 1930s. Large format cells were first produced for primary use in Navigation aids and rail transportation. Later on, small button and prismatic cells were commercialized upon the development of thin electrodes in the 1970s. Electrically rechargeable zinc air cells emanate from the bi-functional oxygen electrode development made in the 1980s. The successful development of rechargeable zinc air cell has been mainly hampered by their poor cycle life and their vulnerability to the environment. However, the interest in the system has not suffered at all and has been increasing instead. As, illustrated in Figure 1.1, Zn-air batteries have the highest energy density and are therefore good candidates in prolonging the runtime of any consumer electronic devices. Besides, Zn-air batteries have a very high specific energy for the lowest cost and zinc is one of the most abundant battery metals. Thus, the interest in Zn-air system as a viable contender to power electric vehicles has been increasing recently, due to the urgency to embrace sustainable mobility by the twin exigencies of peak Oil and Global Warming [10].

Intensive research programs have been carried out over the past decades by many companies such as AER Energy Resources, Inc., Electric Fuel Corporation and most recently Revolt Technology AS. Table 1.3 summarizes some characteristics of the rechargeable zinc-air system.

b. Chemistry

A schematic representation of the components of prismatic cell is illustrated in Figure 1.5. The negative electrode consists of zinc which is used in the form of pressed or suspended fine powders. During the discharge and charge processes, the redox reactions of the oxygen take place in the bi-functional air electrode at the cathode, while zinc is transformed into ZnO and vice versa, as shown in Figure 1.6. The main reactions at the electrodes are the following:

Anode: $Zn + 4OH^{-} \leftrightarrow Zn(OH)_4^{2-} + 2e^{-}$ $(E_0 = 1.25\ V)$ (1.1)

$Zn(OH)_4^{2-} \leftrightarrow ZnO + H_2O + 2OH^{-}$

Cathode: $O_2 + 2H_2O + 4e^{-} \leftrightarrow 4OH^{-}$ $(E_0 = 0.4\ V)$ (1.6)

Overall: $2Zn + O_2 \leftrightarrow 2ZnO$ $(E_0 = 1.65\ V)$ (1.7)

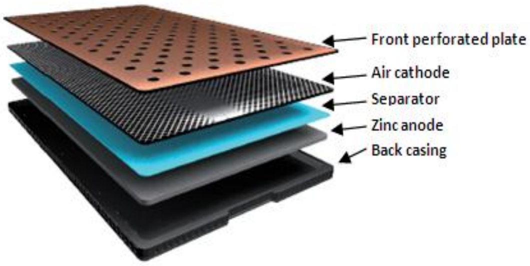

Figure 1.37: Exploded view of prismatic zinc-air battery (Source: Revolt Technology LLC).

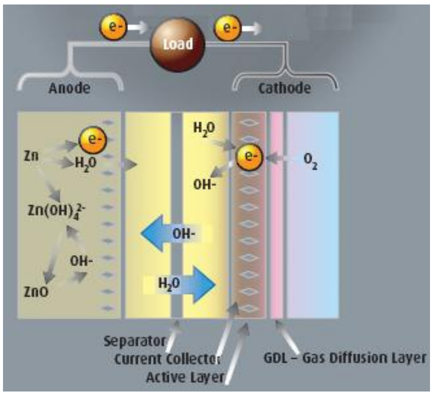

Figure 1.38: Schematic representation of species involved in the zinc-air reaction (source: Revolt technology LLC).

Advantages	Disadvantages
• High specific energy ranging from 300 to 400Wh.kg-1 • Low material cost • Environmentally green • When sealed, the system has excellent shelf life, with a self-discharge rate of only 2 percent per year • Safe chemistry which is abuse-tolerant	• Poor cycle life (<100 cycles at low specific energy) • Sensitivity to the environment after activation • Low C-rate recharge • Relatively high internal resistance

Table 1.3: Rechargeable zinc-air battery characteristics.

1.2.4 Rechargeable alkaline manganese oxide cell

a. Historical

Rechargeable alkaline Manganese oxide Batteries were commercialized by Union Carbide in the 1970s. Despite their low price, their little commercial success resulted from the very poor cycle performance. One problem was that the cells were not zinc-limited. Thus, upon deep discharge Mn(III) was reduced to Mn(II) which is irreversible and causes the manganese oxide electrode to expand. Other problems were the dendritic growth of zinc during the charge and the capability of catalytic hydrogen-gas oxidation was not included in the design.

In the late 1970s and 1980s intensive research lead by Kordesch and carried out at the Technical University of Graz and at Battery Technology Inc (BTI) in Canada resulted in the successful commercialization of what I have been become known as RAM batteries. These cells now have reliable cycle behavior with a good shelf life at elevated temperature. Also, the mercury has been eliminated from the anode paste. Rayovac, Pure Energy and Alcava were among the first companies to manufacture the RAM cells utilizing the BTI's proprietary technology [11].

b. Chemistry

The reaction is a conversion of the cathodic solid structure (MnO_2) into another (MnOOH) in a cell where a suspended zinc powder in a gelled paste serves as the anode. The RAM system is very sensitive to the discharge and charge voltage limits as irreversible manganese oxide products may form and cause the cell to fail. Figure 1.7 shows a cut-away view of a RAM cell including the different components of the system. Some key characteristics of the system are given in Table 1.4. The electrochemical reactions at the anode and cathode are as follows:

Anode: $Zn + 4OH^{-} \leftrightarrow Zn(OH)_4^{2-} + 2e^{-}$ ($E_0 = 1.25$ V) (1.1)

$Zn(OH)_4^{2-} \leftrightarrow ZnO + H_2O + 2OH^{-}$

Cathode: $MnO_2 + H_2O + e^- \leftrightarrow MnOOH + OH^-$ ($E_0 = 0.4$ V) (1.8)

Overall: $Zn + 2MnO_2 + H_2O \leftrightarrow ZnO + 2MnOOH$ ($E_0 = 1.65$ V) (1.9)

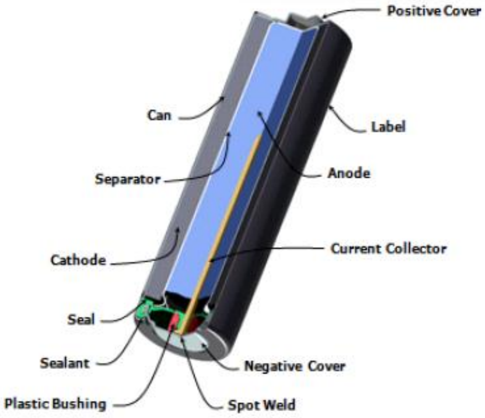

Figure 1.39: Cut-away view of an alkaline manganese dioxide cell.

Advantages	Disadvantages
• Good retention of capacity • Low cost • No ‘memory effect’ problem	• High internal resistance • Limited cycle life (<50 cycles at about 50% DoD)) • Poor utilization at high specific power

Table 1.4: Rechargeable alkaline manganese dioxide battery characteristics.

Chapter 2

Review of the failure mechanisms

2.1 Hydrogen evolution reaction

Hydrogen evolution reaction (HER) is one of the most extensively studied reactions in electrochemistry because it is a phenomenon found in many fields such as corrosion, hydrometallurgy, electrolysis, fuel cells and batteries. The HER takes place at the surface of metals in any aqueous solution and proceeds through a limited number of reaction steps with the involvement of only one reaction intermediate. The ability of a given metal to catalyze the hydrogen evolution reaction is usually measured by the exchange current density, which is the rate of hydrogen evolution per surface area at the electrode potential, where the reaction is at equilibrium [12-15]. The reaction rate is determined by the energy of adsorption and desorption of hydrogen. A low energy of adsorption results in a low reaction rate due to a limited surface coverage. On the other hand, if the adsorption energy is too high, the ability of adsorbed species to desorb is reduced, causing the overall reaction rate to decrease.

Electrode materials for water electrolysis with catalytic properties have been investigated by several authors, and it was found that platinum is very effective [16,17]. This is illustrated in Figure 2.1 by the so-called ‘trasatti volcano plot’ that relates the exchange current density the HER on electrode surface of a series of several metals to their hydrogen bond strength. The pioneering experiments showing the relation between the HER exchange current density and the adsorption enthalpy or the work functions of metal were demonstrated by Conway and Bockris [18] and also by Ruetschi and Delahay [19]. Later on, their work was rationalized by Parsons [20] on a theoretical basis.

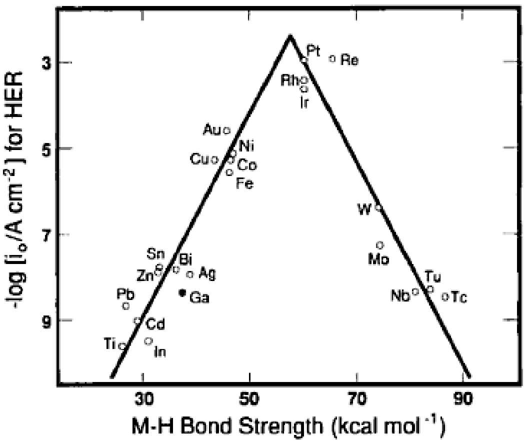

Figure 2.1: Volcano-type correlation of catalytic activity of different metals and the M-H binding energy [16].

In alkaline solution, the reaction path of the HER is classically characterized by (i) a discharge reaction of water molecule on sites at the metal surface (Volmer step) followed by either (ii) a recombination reaction (Tafel step) or (iii) an electrochemical desorption reaction (Heyrovsky step):

i. Volmer reaction

$$M + H_20 + e^- \rightarrow M\text{-}H_{ads} + OH^- \qquad (2.1)$$

ii. Tafel reaction

$$2M\text{-}H_{ads} \rightarrow M + H_2 \qquad (2.2)$$

iii. Heyrovsky reaction

$$M\text{-}H_{ads} + H_20 + e^- \rightarrow M + H_2 + OH^- \qquad (2.3)$$

The resulting hydrogen gas has a very low solubility in water. In the standard conditions (hydrogen pressure of 1 atm), aqueous solutions contain approximately 0.8 x 10^{-3}M H_2 [21]. The solubility of hydrogen tremendously decreases in concentrated alkaline solutions due to salting-out effect [22].

2.1.1 Zinc corrosion

Zinc metal corrodes in alkaline solutions. The corrosion is characterized by the anodic dissolution of zinc with concurrent cathodic hydrogen evolution reaction (HER), as described in reactions (2.4) and (2.5). It is known that zinc anode corrosion leads to the capacity loss, as it results in a formation of an inactive layer of mixed oxide and hydroxide on its surface [23]. In some cases the corrosion of the zinc anode may result in cell overpressure if the hydrogen gas product it not vented out. Therefore, the zinc corrosion is of great importance especially in secondary systems where their effects are often more pronounced due to the long life time of cells as well as the permanent change of the electrode morphological structure upon subsequent cycles and abusive use.

The potential of zinc in KOH solution is a mixed potential [24] determined by the partial oxidation of zinc:

$$Zn + 4OH^- \leftrightarrow Zn(OH)_4^{2-} + 2e^- \tag{2.4}$$

And the reduction of the water molecule:

$$2H_2O + 2e^- \rightarrow H_2 + 2OH^- \tag{2.5}$$

Various methods exist to quantify the amount of hydrogen evolved in a reaction. The volumetric measurement is probably one of the most used. Other techniques such as weight loss and manometric measurements have also been largely utilized.

HER tests can be very lengthy when performed under normal use conditions. Thus, it is very common to carry out the test at elevated temperatures to make predictions about the material's life characteristics in a shorter period of time. Such a test is called 'Accelerated aging' and follows the Arrhenius model described as:

$$Life = Ae^{-\frac{Ea}{KT}} \tag{2.6}$$

Where,

Life: median Life of a population

A: scale factor determined by experiment

e: base of natural logarithms

E_a: Activation Energy

k: Boltzmann's constant = 8.62×10^{-5} eV/K

T: Temperature (degrees Kelvin)

The kinetics of hydrogen reduction of zinc powder can be influenced by a multitude of factors such as, the electrolyte concentration and composition, the shape and size of the zinc particles, the structure and defect of the zinc crystal, as well as the foreign metals and impurities present in the zinc powder.

Figure 2.2 shows the volume variation as a function of time of the evolved hydrogen gas per weight of zinc of a coarse and fine powder fraction aged at 70°C. The kinetic of the HER increases with time probably due to the increase in the concentration of impurity or defect at the metal surface with the advancing dissolution of the base metal. The rate of gassing of the fine powder fraction is higher than that of the coarse powder because of its larger surface area.

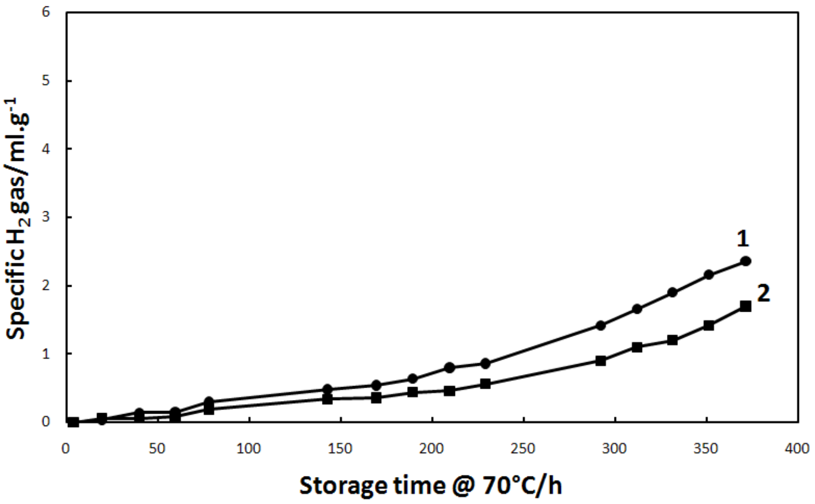

Figure 2.2: Comparison plot of the hydrogen evolution rate between a fine (1) and coarse (2) zinc powder fractions.

Multiple approaches have been investigated over the years to suppress gassing in batteries, including the alloying of zinc or the use of inorganic and organic additives to both the electrolyte and active mass.

a. Alloys inhibitors

Amalgamation has been the most effective way of reducing the corrosion rate of zinc cells in batteries. However, the use of Hg is now limited to very low level owing to environmental concerns. Besides its toxicity, Hg is not a suitable material for rechargeable zinc electrodes because it has the tendency to segregate and form mercury droplet in the electrode bulk upon subsequent cycles. Miura and al. [25] found that alloying zinc with elements such as Cd, Pb, In, Bi and Ti inhibit the corrosion of zinc in 40% KOH solutions. All these approaches involve mostly materials that possess higher hydrogen overpotential than zinc.

One challenge associated with the use of alloy is their surface redistribution and stability over cycling. Indeed, as explained in Chapter 4, the perpetual change of the electrode bulk structure upon repeated cycles may cause an uneven surface distribution of the alloys or their segregation. Some of them may even dissolve during the discharge and not reform during the charge.

b. Inorganic inhibitors

The effects of various metal oxides and hydroxides have also been investigated. Yoshizawa and Muria [26] found that addition of compounds of indium, yttrium and zirconium resulted in significant reduction of the corrosion. The inhibiting mechanism of $In(OH)_3$ is discussed in Chapter 7.

c. Organic inhibitors

It is generally accepted that organic inhibitors reduce the corrosion rate by adsorbing preferentially onto the most active sites of the metal surface. By modifying the surface energy state, organic inhibitors may also alter the passivation and deposition mechanism of zinc crystals. Organic inhibitors have acquired great importance in recent years upon the ban of Mercury. Nartey et al. [27] investigated a multitude of organic corrosion inhibitors suitable for rechargeable alkaline zinc batteries and have found that polyethylene glycol (PEG) 600 and α-Diphenylglyoxime exhibited the best performances. But Dobryszycki and Biallor claimed that PEG400 was more effective than PEG600 [28]. Phosphate ester, sulfonic acid and carboxylate based surfactants have also been claimed as potential inhibitors of zinc corrosion [29-30].

The stability of the inhibitors within the potential window of operation is crucial parameter. The concentration of inhibitors should be maintained low since they generally decrease the activity of the zinc electrochemical reaction.

2.1.2 Zinc hydrogen overpotential

Hydrogen evolution reaction (HER) during the cathodic polarization in aqueous solutions has always been a topic of particular interest, as it is a rather common phenomenon observed in electrowinning and battery technologies. In alkaline secondary zinc cells, the control of the zinc electrodeposition taking place during charge (cathodic polarization) is of prime importance to prevent the hydrogen gas from evolving.

The reduction of the zincate ions to metallic zinc in alkaline solution is generally coupled with that of the water according to the reactions described in (2.4) and (2.5).

The undesired water reduction reaction is one of the root causes to the electrode charge inefficiency since it consumes a fraction of the charge current. Charge inefficiency can be detrimental for the system as it results in capacity decay.

The rate of the hydrogen evolution reaction depends on the electrode overpotential η, the current density distribution and the electrolyte composition.

Once formed, the hydrogen gas may escape or remain trapped at the interface between the anode and the cathode or in the electrode bulk. In any case, gas entrapment can cause the cell to leak due to the pressure build-up. The entrapped gas can also give rise to the formation of resistance pouch inside the cell, resulting in an increase of the system impedance.

The overpotential η is related to the exchange current density *i* and the Tafel slope *b* through the Tafel equation:

$$\eta = a \pm b\log(i) \tag{2.7}$$

$$a = \frac{2.3RT}{\alpha nF}\log(i_o) \quad , \qquad b = \frac{2.3\mathrm{RT}}{\alpha\mathrm{nF}} \tag{2.8}$$

i_o is the exchange current density and n is the number of transferred electrons. R and T denote the molar gas constant and the temperature respectively. α is the charge transfer coefficient and it is usually taken as equal to ½.

Lee [31] demonstrated that HER Tafel plots measured on a zinc electrode in 6M KOH solution are linear and exhibit a slope of 124mV/dec, as illustrated in Figure 2.3.

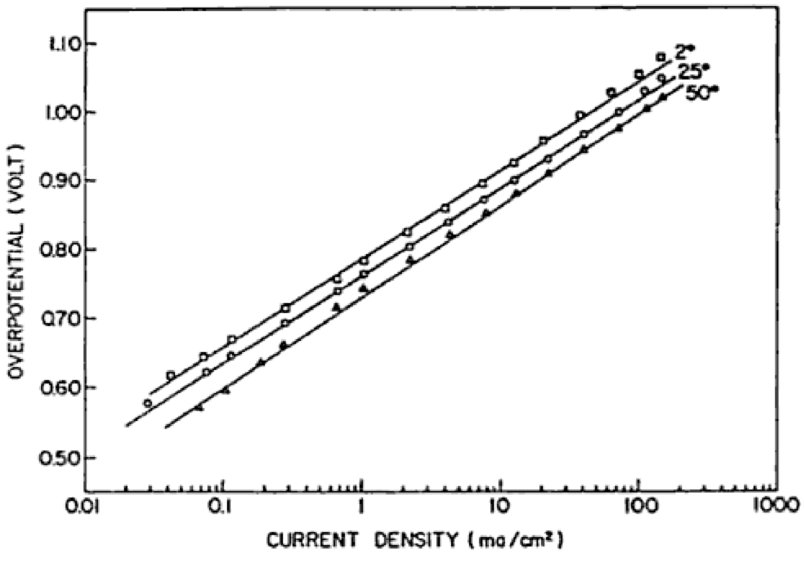

Figure 2.3: Hydrogen overpotential on Zn in 6M KOH; After Lee [31].

In most cases the Tafel slope for hydrogen evolution on metal electrodes in aqueous solutions has a value of about 120mV/dec [32]. The values of the exchange current density and Tafel slope determined in various solutions are listed in Table 2.1.

Solution	b (mV)	log i_0	Reference
1N HCl	232		14
1N H2SO4	124		14
1M NaCL, PH=5.8	200		110
1M NH4Cl, PH=5.8	120		111
1N LiOH	150		311
1N NaOH	120		311
1N KOH	140		311
5N KOH	160		311
6N KOH	124	-9.1	7
9N KOH	145		311
9N KOH	124	-8.2	7

Table 2.1: Tafel slopes and exchange current densities for hydrogen reduction on zinc in aqueous solutions [32].

2.1.3 Galvanic coupling

Galvanic corrosion is the effect resulting from contact between two dissimilar metals or alloys in a conducting corrosive medium. The effect is characterized by a current, which is called 'galvanic current', flowing from the least to the most noble metal. The polarity and direction of the current flow between the two connected metal is determined by the thermodynamic reversible potentials of the metals.

Galvanic corrosion is generally more complex than the normal corrosion as it involves geometry factors in addition to material and environment factors. The fundamental relationship in galvanic corrosion is given by Kirchhoff's second law:

$$\mathrm{E_c - E_a = IR_e + IR_m} \qquad (2.9)$$

Where $\mathrm{R_e}$ is the resistance of the electrolyte portion of the galvanic circuit, $\mathrm{R_m}$ is the resistance of the metallic portion, $\mathrm{E_c}$ is the effective (polarized) potential of the cathodic member of the couple, $\mathrm{E_a}$ is the effective (polarized) potential of the anodic member and I the galvanic current.

In alkaline zinc cells, the anode generally consists of active zinc mass coupled with a more noble metal that serves as a current collector (copper preferably). Consequently, zinc dissolves and the resulting electrons emigrate to the copper where they are consumed by water at the most active sites to produce hydrogen.

The reaction routes are similar to those of the zinc corrosion (2.4 and 2.5) with the only exception that the water reduction takes place on the current collector surface.

a. Porous Zinc anode

In practice, the effect of galvanic coupling between the zinc active mass and the copper substrate is somehow minimized because of a spontaneous deposition of zinc film that protects the substrate surface. Such phenomenon is commonly observed on a metal surface that is in contact with the slurry mixture of Zn and ZnO [33]. Figure 2.4 shows the surface transformation of a copper current collector screen before (a) and after (b) contact with zinc paste. The surface metallization of copper with zinc is possible in these conditions because copper is forced to be at the potential of Zn-$Zn(OH)_4^{2-}$ equilibrium without any external power source. This is thought to be favored by the 0.3 eV work function difference between the two metals [34].

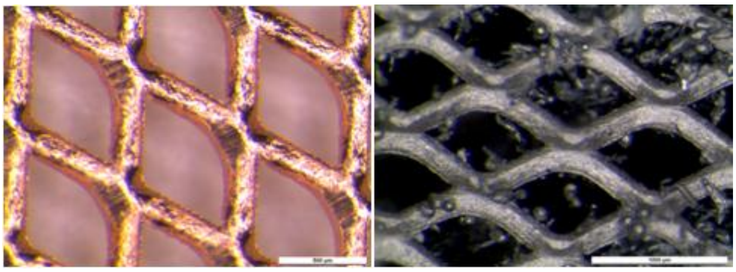

Figure 2.4: Surface of the copper mesh screen before (left) and after (right) contacting with a zinc paste.

The effect of the coupling on the gassing is illustrated in Figure 2.5 where the rate of the HER resulting from the corrosion of zinc is much higher in presence of a copper substrate. For rechargeable zinc electrodes, spontaneous plating of copper surface with zinc is not sufficient alone to tackle the gassing issue resulting from galvanic coupling. In fact, the zinc film deposit can oxidize in presence of oxidative agents such as peroxide and oxygen or may dissolve upon subsequent cycles. Figure 2.6 shows a spot on the copper current collector imbedded in zinc paste and where the protective zinc film has been stripped off the surface. This electrode was cycled only 20 times at 50% depth of discharge. The exposed spot is a potential source for the hydrogen evolution reaction due to galvanic coupling or the corrosion of copper. Note that copper has a lower hydrogen overvoltage than zinc.

Galvanic coupling can be prevented by coating the current collector substrate with a film of a metal possessing higher hydrogen overpotential than zinc.

b. Plating of the current collector

The plating process is generally preceded by a meticulous cleaning of the substrate. The cleaning step involves several stages:

- Removal of grease and oil deposits
- Removal of oxide films
- Etching or activation of the substrate surface with acid so that it is more receptive to the metal being plated.

The protective layer ought to be made of metal that has higher hydrogen overpotential than zinc. It ought to be non-toxic and stable within the potential window of the operation for rechargeable zinc electrodes. Generally, current collectors of zinc anodes in alkaline cells are coated with indium or tin by electroplating or PVD process. Cadmium (Cd) has also been used but has now become less attractive because of its toxicity. The PVD process of tin (Sn) and indium (In) is favored by the low melting point of the two metals.

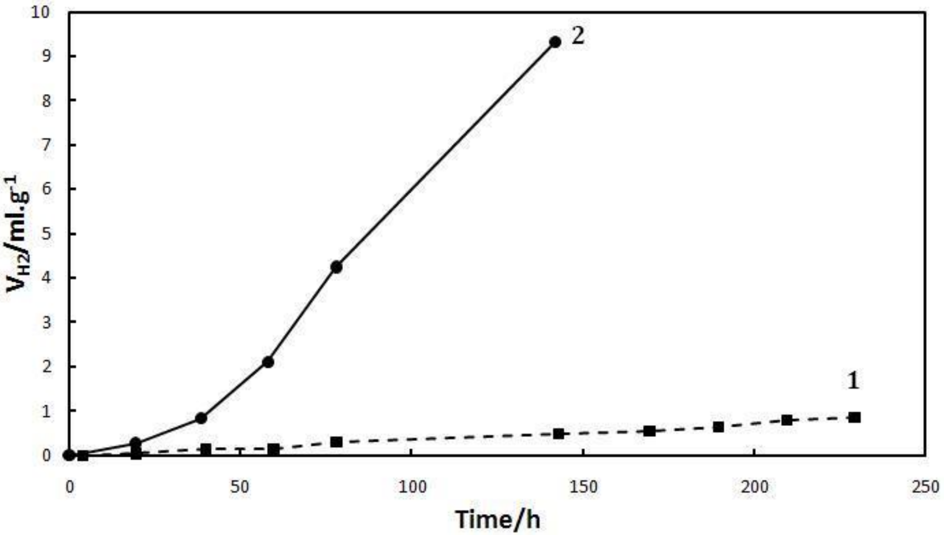

Figure 2.5: Hydrogen evolution rate as a function of time of the zinc paste solely (1) and zinc electrode (2) in 7M KOH solution. Test performed at 70°C. Source: Revolt Technology AS.

Figure 2.6: Area of a copper current collector of a rechargeable zinc electrode where the spontaneous zinc film deposit was stripped off upon repeated cycles. Source: Revolt Technology LLC.

2.1.4 Effect of KOH concentration on HER of zinc electrode

The corrosion rate of zinc depends on the KOH concentration and varies with the test conditions. Three type of relationship between the corrosion rate and KOH concentration have been reported, indicating that different rate-determining reactions may be involved in each case:

(a) Corrosion rate increases with increasing KOH concentration due to the ability of the electrolyte to dissolve the oxide surface film resulting from dissolution [35]. Thus, the rate of corrosion is controlled by the reaction given in (2.4).

(b) Corrosion rate decreases with increasing KOH concentration. Snyder and Lander [36] explained the behavior as a result of the reduced activity of water, implying that the reaction described in (2.5) controls the kinetics. This is concordant with the findings made by Dirkse and Timmer [37].

(c) Corrosion rate decreases with increasing KOH concentration at low concentrations, reaches a minimum, and then increases with concentration at high KOH concentration [38]. This behavior is indicative of change in the rate-determining reaction as solution goes from low to high KOH concentrations. At low KOH concentrations type (b) dominates whereas at high KOH concentrations type (a) is imposed.

The corrosion rate of a porous zinc electrode pressed onto a copper mesh collector in various KOH solutions is shown in Figure 2.7. The result suggests an increase of the rate of corrosion with the KOH concentration.

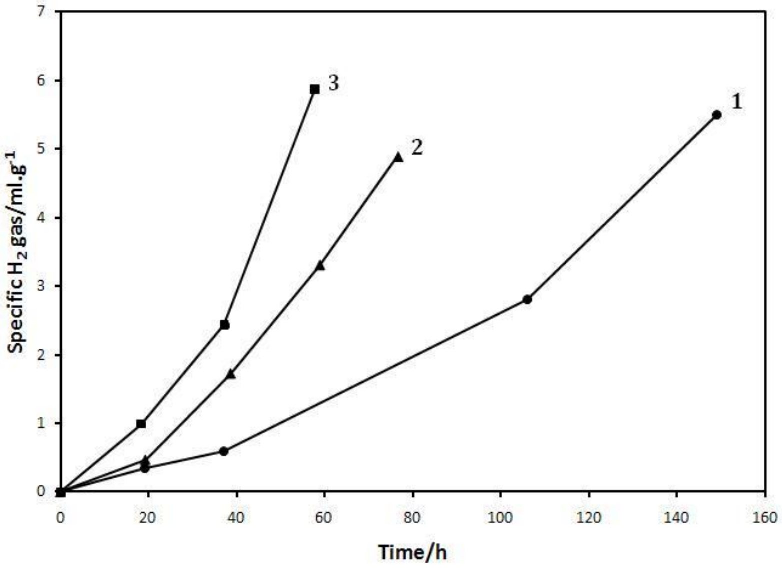

Figure 2.7: Variation of the hydrogen evolution rate as a function of time of a zinc electrode in 2M KOH (1), 7M KOH (2) and 11M KOH (3) solutions at 70°C.

2.1.5 Hydrogen Recombination catalyst

Another alternative to suppressing HER with additives is to consume the formed hydrogen gas away. The hydrogen recombination uses catalytic oxidation to scavenge hydrogen from cells. The H_2 to H_2O fractional conversion depends mainly on the catalyst type, the operating temperature and the hydrogen adsorption rate. Hydrogen removal by catalytic oxidation has the advantage to be a sort of water balance tool for the system as it compensates for the water loss. The water consumption is a direct consequence in the hydrogen evolution reaction, as illustrated in reaction (2.5). The catalytic oxidation of hydrogen on precious metals normally occurs at relatively low temperatures within a wide range of concentration. The catalysts generally contain a single or several noble metals such as Pd, Pt, Ru or salt thereof which are combined to some metal oxides. The catalyst lowers the activation energy of the oxidation process between hydrogen and the metal oxide. The metal oxide is replenished upon the exposure of the metal to oxygen as indicated below.

$$MO + H_2 \xrightarrow{P_tCl_3} H_2O + M \tag{2.10}$$

$$M + \frac{1}{2}O_2 \rightarrow MO \tag{2.11}$$

Several patents [39-40] teach the synthesis and the use of the catalysts based on PtCl3, RuCl3 and PdCl3 salts in metal air batteries. Some promising noble metal-free catalysts have been studied can be found in the literature [41]. K-R Kim et al. [42] claimed that the mixture of Pd/Al_2O_3 is an effective catalyst with a 0.9 fractional conversion.

2.2 Passivation

2.2.1 Theory

The need for developing zinc alkaline batteries that can sustain high discharge drain rate has been increasing over the past decade. Automotive is only one example of application among others where the demand in power consumption is large. Therefore, the passivation of zinc electrode that generally occurs at high drain rates becomes a major issue as its occurrence limits the cell capacity.

Passivation is a well-known phenomenon that has been extensively studied by numerous investigators. The occurrence of passivation of zinc surfaces is determined by the thermodynamic and kinetic conditions for formation of a stable and compact solid surface film [Gregory].

It is generally accepted that zinc passivation proceeds through multiple stages and several mechanism paths have been proposed. Hubert [43] suggested an underlying layer of $Zn(OH)_2$ with an overlayer of ZnO. Powers and Breiter, on the other hand proposed a dual layer of ZnO [44], one formed from the “dissolution-precipitation” to produce a loose flocculent film (Type I), and the other formed by solid-state mechanism beneath it (Type II), as schematized in Figure 2.8. McKubre and Macdonald [45] provide in their paper an explanation for the passivation sequences that is consistent with the dual layer model of Powers and Breiter.

In Figure 2.9, Lui et *al.***[46]** summarize the mechanism of the formation of passive films. In the first stage, the anode is dissolved for a time t_a, producing zincate ions, resulting in a concentration gradient with an accumulation of zincate ions in a fine layer of electrolyte near the electrode surface. When, the layer of electrolyte reaches the supersaturation, the typeI ZnO begins to precipitate. The anodic dissolution continues through the porous film up to a time t_b at which the rate of mass transport of hydroxyl ions falls below that required for the formation of zincate ions causing the onset of the type II ZnO formation. The electrode surface becomes passivated when it is fully covered up with the type II oxide after an additional time t_c. The passivation time t_p can therefore be defined as the sum of t_a, t_b and t_c.

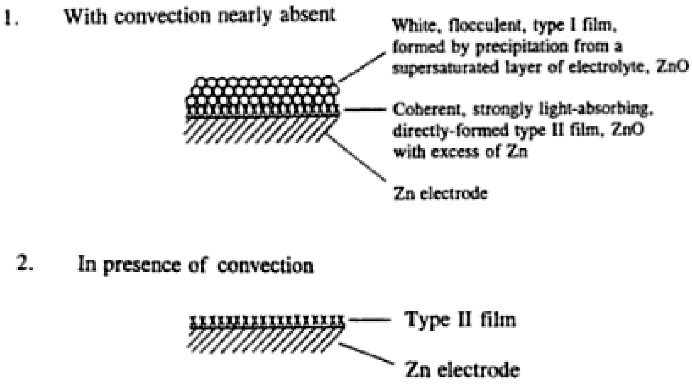

Figure 2.8: Schematic illustration of the films formed on zinc electrodes in 7M KOH under different convection conditions. After Powers [44].

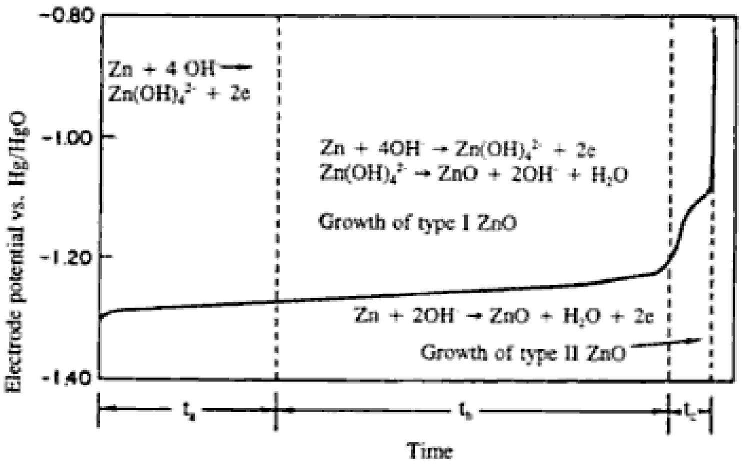

Figure 2.9: Proposed scheme for the processes associated with the anodic passivation of zinc in alkaline solutions. After Liu et al. [46].

A linear relation exists between the current density and the reciprocal of the square root of the passivation time t_p for a wide range of conditions following the equations of type [46, 47]:

$$(i - i_0)t_p^{1/2} = k \tag{2.12}$$

Where i is the applied current density and both i_0 and k are constants whose values depend on the system conditions.

2.2.2 Discussion

The electrode capacity increases when the passivation is delayed. One suggested solution to retarding the passivation is to optimize the overall effective surface contributing to the reaction during the electrode life. Any loss in active surface upon subsequent cycles would cause the effective current density of the electrode to increase giving rise to precocious passivation onset as a result. For rechargeable electrodes, it is therefore necessary to:

- Ensure a good electric conductivity by maintaining the network connectivity of the zinc particles within the electrode body.
- Ensuring a homogeneous distribution of the electrolyte through the bulk surface of the electrode.

  This can be achieved with an appropriate design of the electrode thickness and porosity so to avoid pore plugging that generally leads to the isolation of a fraction of the active surface.

The use of additives to promote the zinc dissolution has been explored. Some studies [48, 49] claim that the presence of Li^+ and SiO_3^{2-} ions may increase the utilization of the zinc anode by retarding the passivation. However, the effect may depend on the electrolyte concentration. For instance, silicate was found to enhance passivation in highly concentrated KOH solutions [50].

Passivation can also be retarded by optimizing the electrolyte concentration. In the present work, the capacity of a porous zinc electrode was investigated in KOH electrolyte of various concentrations over a wide range of current density. The result indicates an increase of the electrode capacity with the electrolyte concentration, as shown in Figure 2.10. It is also suggested that the capacity drops down with increasing the current density. The setup used for the experiment is described in section 3.1.3.

Sunu and Bennion [51] suggested that discharge of the zinc electrode with a given initial porosity could fail due to the decrease in pore size (blockage of the first kind). The primary effect of the decreased pore size is the restricted diffusion of electrolytes into the interior of the porous electrode, causing electrolyte depletion at the reaction sites. If the porosity falls below a certain limit, the resistance across the pore solution rises substantially and serves as a factor in limiting further utilization.

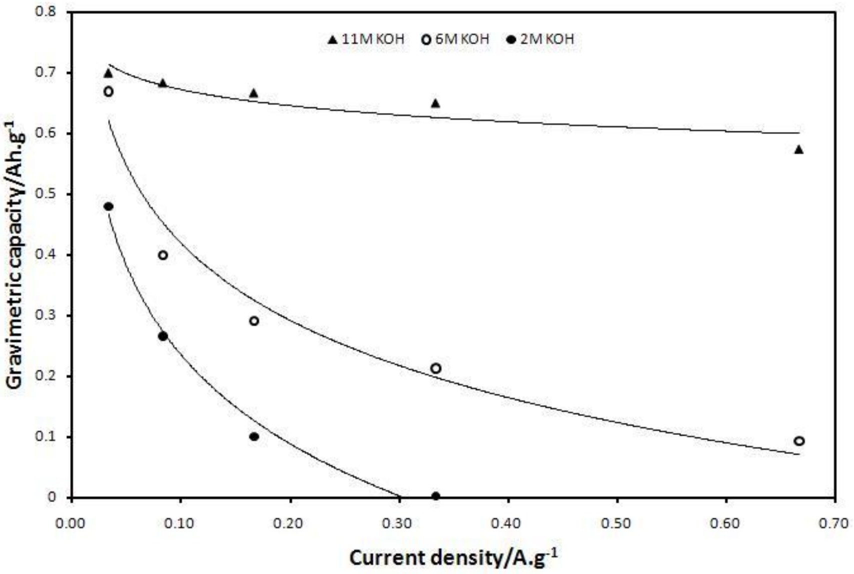

Figure 2.10: Variation of the specific capacity of zinc electrode in KOH solutions with current density and KOH concentration: (●) 2M KOH; (o) 6M KOH; (Δ) 11M KOH (Source: Revolt technology LLC).

2.3 Shape change

2.3.1 Theory

Upon repeated cycles, an inhomogeneous redistribution of the active material over the zinc electrode surface takes place, limiting the cycle performance of cells. Such a transformation is generally called shape change and it is due to the high solubility of the dissolution products of zinc in alkaline solutions. An example is shown in Figure 2.11 where the surface morphology of two prismatic zinc electrodes that were cycled 5 and 100 times are respectively shown in (a) and (b).

Several mechanisms have been proposed to explain the shape change. A mechanism based on gravitational effects was stipulated [52] and ruled out since the shape change is independent of the cell reaction. Mc Breen [53] suggested a concentration cell effect as a mechanism of the shape change. He suggested that the concentration cell is the result of the difference in the current distribution during charge and discharge.

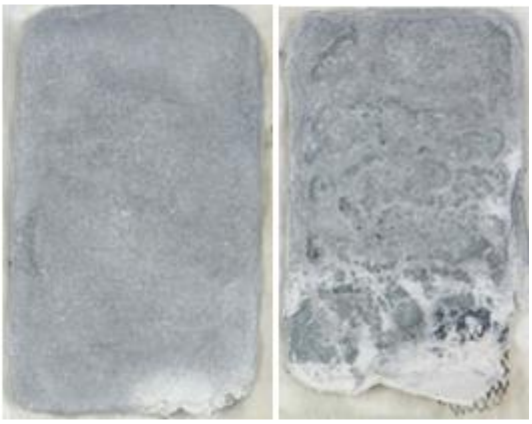

Figure 2.11: Morphology of prismatic zinc electrode after the 5th cycle (left) and 80th cycle (right) at 50% depth of discharge (source: Revolt Technology LLC.).

Choi and al. [54] proposed the concentration cell generated by the difference in convective flow pattern during cycling as the main cause of the shape change. i.e., flow of supersaturated zincate solution toward the zinc electrode center during discharge and flow of unsaturated zincate solution toward the electrode edge or solution reservoir during the charge.

Various mathematical models have been proposed to describe and predict the zinc behavior of porous electrode [55]. Sunu and al. have developed a model to describe the transient behavior of the porous zinc electrode on the basis of concentrated ternary electrolyte theory [56]. The model takes into account the effect of local mass transfer between the electrode active surface and the bulk solution in the pores, changes in porosity, variations of active surface area, and convection arising from the difference in molar volumes of reactants and products. The effect of the membrane separator and the solution reservoir on the zinc electrode performance is also included in the model to simulate conditions similar to a practical battery system. However, other factors such as effects of gas generation and changes in morphologies and the active surface area with cycling were excluded. The results of the numerical solutions suggest certain modes of failure and performance limitations of the zinc electrode, as presented below.

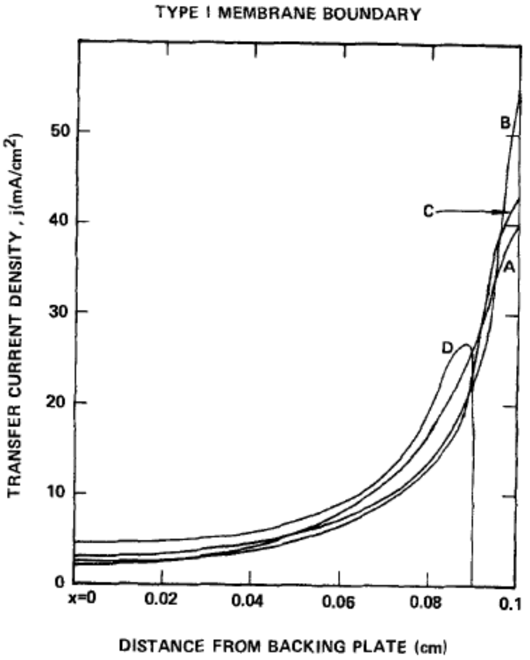

Figure 2.12: Distribution of local charge transfer current, j (mA/cm^2), for type I membrane boundary (I = 50mA/cm^2, L = 0.1cm, and A, B, C and D represent 0%, 10%, 20%, and 40% depth of discharge, respectively) [56].

The charge transfer current, j (mA/cm^2), as a function of distance for various depth of discharge, as predicted by Sunu's model is shown in Figure 2.12. The model suggests that the reaction distribution is maximal at the face of the electrode where the reaction predominately starts off. At 10% DoD, the KOH concentration starvation in the bulk causes the reaction to shift toward the front face where the supply in hydroxide ions is optimal (curve B). When the electrode is beyond 20% depth, the reaction at the electrode front face starts decreasing due to the depleted active zinc metal (curve C). At higher DoD the effective reaction zone move from the front face toward the backing of the electrode due to the complete utilization of initial zinc metal (curve D).

Sunu's model also predicts the distribution of solid zinc and ZnO, in terms of volume fractions, as plotted in Figure 2.13. The total amount of ZnO precipitated, *i.e.,* the integrated area of ZnO profiles, is smaller for the solution case than for the membrane case. For example, after 40% depth of discharge, the amount of precipitated ZnO obtained from cell with and without a separator membrane is 95% and 55%, respectively, for the same total amount of the zinc consumed. The larger amount of ZnO in the cell with membrane is due to the fact that the presence of separator limits the diffusion of zincates into the counter-electrode compartment, causing its precipitation.

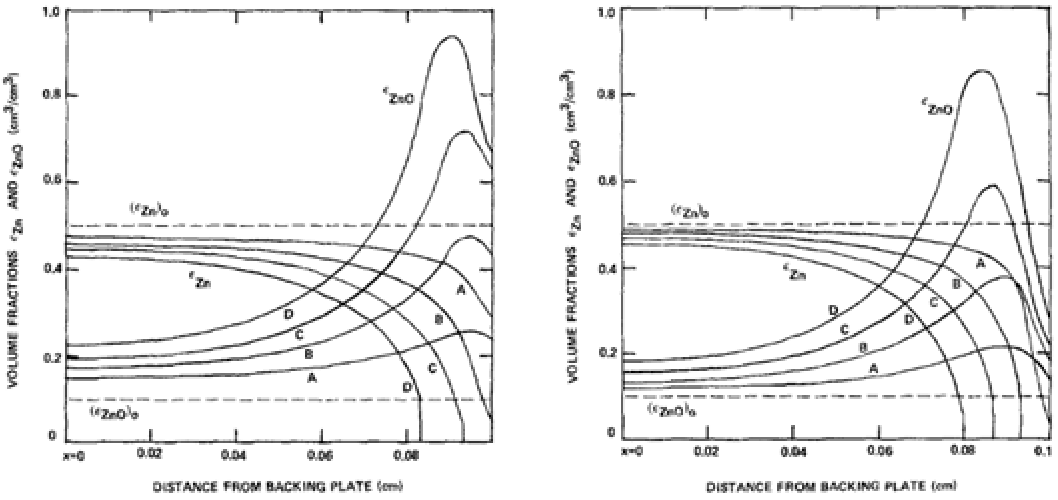

Figure 2.13: Distribution of Zn and ZnO as volume fraction (left) for type I membrane and (right) for solution boundary (I = 50mA/cm^2, and A, B, C and D represent 0%, 10%, 20%, and 40% depth of discharge, respectively) [56].

For cycling cells of a given design, Sunu and al. showed that current distribution becomes more uniform on charging than on discharging, in particular, near the beginning of charge. When charge starts, the solid-solution interfacial area near the electrode face contains mainly the area of ZnO precipitates and a very small active zinc area. This reduced zinc area at the electrode face prohibits the transfer reaction on charge and shifts the reaction toward the backing plate, resulting in curve A. If sufficient amount of zinc forms and serves as nucleation sites for further zinc deposition reaction, current distribution which is similar in shape to that of discharge will result (curves B and C). Figure 2.14 shows the volume fractions of zinc and zinc oxide during two cycles as a function of the distance from the backing plate. The model shows that the solid zinc species (Zn and ZnO) do not reform in their original positions after complete cycling due to the difference in the current distribution during discharge and charge. On repeated cycling, this difference of anodic and cathodic current distributions together with differences in the degree of super-saturation or un-saturation causes the redistribution of solid zinc species and thus significant distortion of the electrode structure [56].

2.3.2 Discussion

The inhomogeneous redistribution of zinc mass is seen as one major factor limiting the cycle life and performance of accumulators in alkaline solution. Shape change usually gives rise to densification, hardening and localized dead zones across the electrode surface. Chemical, mechanical and electrical solutions have been explored to control these structural changes.

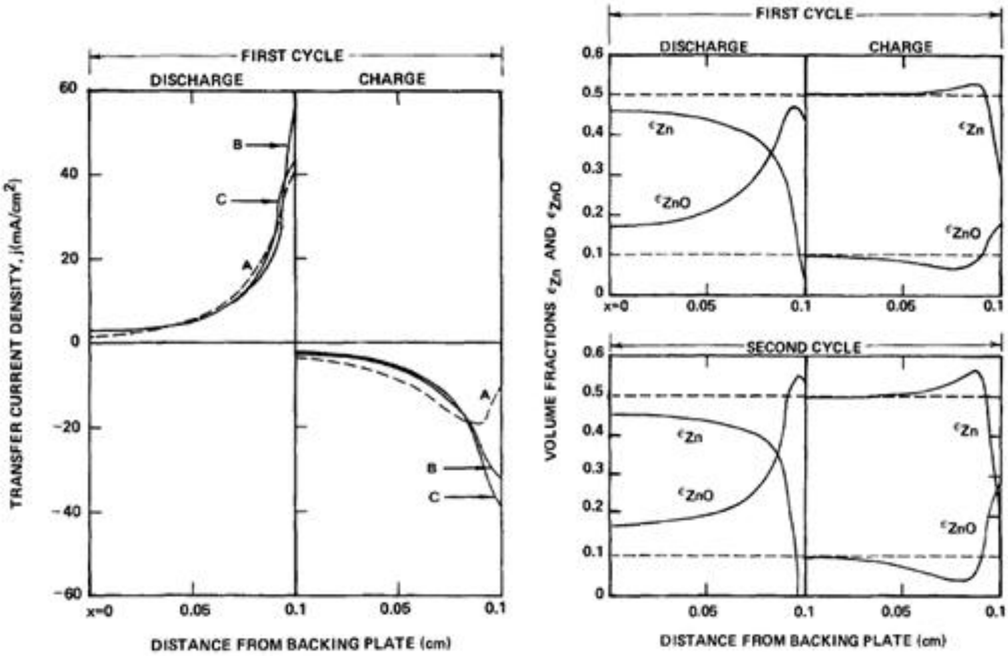

Figure 404: Distribution of Zn and ZnO as volume fractions during two cycles for type I membrane (I = 50mA/cm^2, L = 0.1cm) [56].

a. Chemical solutions

In general, most of the chemical approaches revolve around decreasing the solubility of the zincate ions. This can be achieved by using additives or by merely lowering the electrolyte concentration. The additives can be present in the cell as a solid or dissolved species. Note that all approaches hinder more or less the utilization of zinc.

Additives act either by reducing the ionic conductivity of the solution, or by complexion of the zincate to form larger ions that move more slowly or by forming insoluble composites with zincates ions.

Few examples of soluble additives are KF, H_3BO_3, K_2CO_3, LiOH that have been investigated to limit the solubility of zincate products [57-59]. It was especially found that the ternary KOH-KF-K_2CO_3 electrolyte decreases the rate of zinc electrode shape change with only very limited capacity loss. Other additives such as calcium citrate [60] and calcium gluconate [61] have also been found to improve the capacity retention and the cycle life of cells when added to the solution.

Insoluble additive compounds have also shown promising potential. For an instance, usage of carbon additives to electrode that accelerate the precipitation of the reaction products and improve the electrical conductivity has been investigated [62, 63]. Some studies claim the benefit of using calcium oxide (CaO) or calcium hydroxide $Ca(OH)_2$ to reduce the shape change effect by trapping the soluble zincate in the electrode structure [64, 65, 66]. The same effect is attributed to the usage of SnO_2, Bi_2O_3, Ga_2O_3 [67, 68, 69]. In practice, one shortcoming is associated with the use of insoluble additives due to large volume amount generally needed to neutralize zincates. This results in a significant decrease in the cell energy density.

b. Mechanical solutions

The mechanical approaches involve mainly the design of the zinc electrode and the surrounding components in the cell pack. It was found that shape change can be minimized by preventing the convection by a tight packing design of cells [54]. Other factors that promote shape change are the non-alignment of positive and negative electrodes as well as the type and quality of the separator membranes (resistivity, flatness, imperfections, etc…). The increase of the stoichiometric ratio of the negative to positive active material in the cell proved to reduce the rate at which shape change occurs with cycling.

c. Electrical solution

Reducing the depth of discharge or the current density can significantly improve the cycle life of batteries. Figure 2.15 illustrates the cycling performance of two identical Zn-air cells tested at 100 and 25% DoD in ambient conditions. The throughput capacity yields indicate that the cell cycled at 25% DoD performed better than that cycled at 100% DoD.

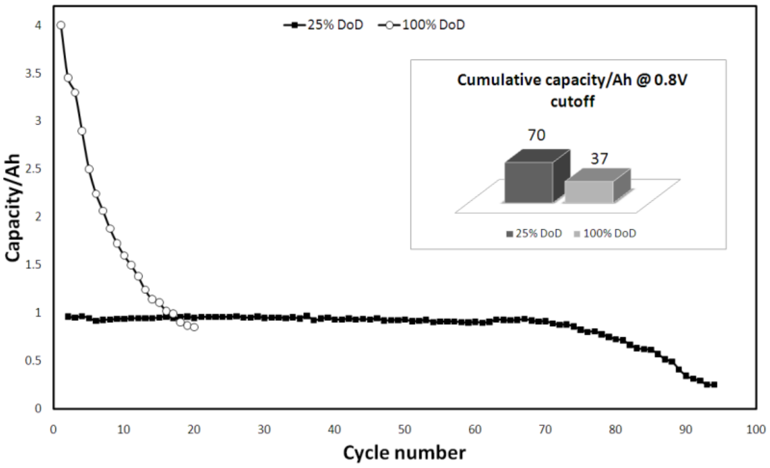

Figure 2.15: Variation of the capacity of a zinc-air cell with cycle number and depth of discharge at 0.8V cutoff voltage. Source: Revolt Technology LLC.

2.4 Dendrite formation

2.4.1 Theory

During the charge process, the deposited zinc crystals may grow in a shape of a tree-like structure at the interface near the separator membrane. Such a type of structure is named ’dendrite’ and it takes place at points of high current density. Dendrites can pierce the separator and reach the cathode, causing an internal short circuit and resulting in a premature failure of cells. Numerous studies have been carried out to prevent the short circuit by developing separator membranes with superior performances. Another approach has been to prevent the dendritic growth by controlling the electrodeposition process using complex charge current profile or additives to the electrode or electrolyte.

a. Electrodeposition

The electrodeposition of metallic layers from aqueous solution consists with the reduction of the metal ions present in the electrolyte on a conductive substrate surface. The electrons consumed in the reaction are provided by either an external potential source or by a reducing agent present in solution (electroless plating). The quality of the substrate surface, the nature of the metal being deposited and the rate of the deposition reaction are the major factors influencing the process.

The electrodeposition process involves several intermediate stages. The most important of these are [70]:

- Transport of the hydrated metal ion or complex from the bulk solution to the cathode.
- Stripping the hydration sheath from the metal ion at the metal-solution interface.
- Charge transfer with formation of adsorbed atom (ad-atom) at the substrate surface.
- Formation of crystal nuclei by the surface diffusion of the ad-atoms.
- Fusion of thermodynamically stable crystal nuclei to form a metallic layer

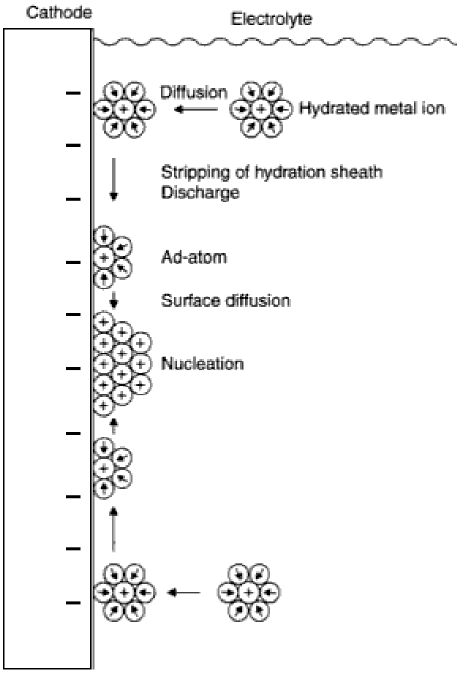

Figure 2.16: Migration of hydrated metal ions to a cathode, surrender of the hydration sheath, formation of ad-atoms, formation of crystal nuclei at the cathode surface [70].

Figure 2.16 gives a very simplified description of the different stages and their sequence of the actual process. The formation of nuclei results from lateral diffusion of ad-atoms. The growth process starts only if the radius of the crystal nucleus is larger than the critical size r* which relates to the change in free energy for a given volume of a solidified material ΔG_V as follows:

$$r^* = \frac{2\gamma}{\Delta G_V} \tag{2.13}$$

b. Electrodeposition overvoltage

As shown above, several steps are involved in the process of electrocrystallization. Therefore, the expression of the electrodeposition overvoltage is the sum of the overvoltage characterizing the individual steps:

$$\eta_{tot} = \eta_C + \eta_D + \eta_K + \eta_R \tag{2.14}$$

η_C : Concentration overvoltage

η_D : Charge transfer overvoltage

η_K : Crystallization overvoltage

η_R : Resistance overvoltage

Any of the steps can be the rate-determining step of the electrode reaction. However, the charge transfer and the concentration overvoltage are the dominant terms [70].

$\eta_R = Ri$	$\eta_D = -a + b\log i$
$\eta_C = \frac{RT}{nF} ln \frac{1 + ({}^{i}/_{i_{l,red}})}{1 + ({}^{i}/_{i_{l,ox}})}$	$\eta_K = \frac{RT}{nF} ln \frac{C_{ad}}{C_{ad}^{o}} = \frac{2\gamma V}{nFr^{*}}$

Table 2.2: Overvoltage during the electrodeposition reaction.

Table 2.2 shows the respective equations characterizing the different overvoltages. Here, R is the resistance of the system, i is the current of the deposition reaction. $i_{l,ox}$ represents the diffusion limiting current of the oxidation reaction whereas $i_{l,red}$ represent that of the reduction reaction. V is the molar volume of a crystal nucleus of critical size and the concentrations of ad-atoms at the growth site and in the equilibrium state are C_{ad} and C_{ad}^{o} , respectively.

c. Mass transport effect

The growing of electrodeposits is influenced by the availability of the necessary ions to build up the crystal at the surface vicinity of the substrate.

Assuming a process controlled by diffusion, for a linear concentration gradient, the diffusion current is given by

$$i = -DnF\frac{c^{0} - c_{x=0}}{\delta} \tag{2.15}$$

If the electro crystallization reaction takes place on a non-uniform surface such as that of porous electrodes, the greater amount of deposition will occur on spots that stick out because of their smaller diffusion layer thickness. This will cause the surface unevenness to increase, resulting in the formation of rough deposit.

Several types of unevenness due to electrodeposition exist from the surface atomistic to the macroscopic scale. Dendrites are a good illustration and they seem to originate from the tips of pyramid as a result of rotation of screw dislocations. The tip of the pyramid may be subject to a spherical diffusion if the radius of the pyramid grows too small [71], explaining the appearance resembling a leafy plant.

2.4.2 Discussion

a. Charge profiles

One way of influencing the dendritic growth is the use of sophisticated charge profiles. These include alternating superimposed currents, pulse currents, periodic reversals and half-wave rectified a.c. [72, 73, 74]. Naybour [75] has investigated such methods and concluded that they all lead to limitations on the charge rate and appear not to be a very promising route for solving the problems of the zinc electrode in free electrolyte systems.

b. Additives

Several additives have been tested to limit the dendritic growth. Inorganic additives such as lead, tin or bismuth seem to induce very small crystallites, and are recommended to improve the compactness, as they yield smooth deposits [76, 77].

It has been reported in several studies that organic compounds based on phosphate, sulfonate, ammonium and fluorinate can be effective in promoting very adherent and finely crystallized deposits [78]. Chang Woo Lee and al. have reported that additives such as phosphoric acid, tartaric acid, succinic acid and citric acid reduce the dendrite formation to some extent [79]. The benefit effects of different types of perfluorosurfactants on the zinc electrodeposition have also been investigated [80].

Organic additives also called ‘surfactants’ act by adsorbing onto the electrode surface where their molecules compete against water. It is believed that the organic molecules adsorb at some preferential crystal faces or sites (the most active ones). In this case the ratio of growth velocities of the different faces and sites will be altered from that obtained in absence of organic additives. This may cause the growth rates to even out, resulting in smooth and even deposits [81].

Unfortunately organic additives are rapidly oxidized in the battery environment. This can give rise to operational problems.

c. Separator

Separators have a direct influence on the key parameters of the battery such as charge efficiency and discharge capacity….the wrong separator leads to premature failure. Some of the basic requirements for separator are contradictory [82]. For instance, from the charge acceptance point of view, the separator must be as open in structure as possible, but safety and long-term reliability require a structure resistant to perforation of dendrites, and thus, a separator as hermetic as possible. A non exhaustive list of requirements is presented in Table 2.3.

Separators for batteries can be categorized into different types, depending on their physical and chemical characteristics. They can be molded, woven, non-woven, microporous, bonded, papers, or laminates. Arora and Zhang [83] divided the separators into six types. But only four of them which are generally used in alkaline-based cells are described below.

- *Microporous Separators*.

They contain pores which are greater than 50-100 Å in diameter. They can be made of polyolefins (PE, PP), nylon, cotton, glass, polyester, etc….

- *Nonwovens*.

They are manufactured directly from fibers bonded by friction, and/or cohesion, and/or adhesion. The materials used in nonwoven fabrics include a single or a combination of polyolefin such as Polyethylene (PE), polyproprylene (PP), polyamide (PA), Poly-tetrafluroehtylene (PTFE), polyvinylidine fluoride (PVdF), Poly-vinyl chloride (PVC).

- *Ion Exchange Membranes*

They are polymeric materials containing pores with diameters smaller than 20Å. The transport properties of ions are characterized by strong interactions between the permeating species and the molecular structure of the polymer due to the presence of ionic exchange group in the membrane. The ionic exchange group allows the membrane to discriminate between permeating or migrating ions by virtue of their specific charge. They are made from PE, PP, or Teflon-based films. These membranes generally undergo additional treatment to increase their hydrophilicity because they are impervious to electrolyte flow.

- Supported Liquid Membrane

They comprise a solid porous membrane and a liquid phase filling up the pores. The liquid phase is generally of an insoluble organic phase that provides adequate ionic conductivity. The porous membranes can be made of polyolefin of several kinds.

Requirement	Solution
• Chemical resistance against electrolyte and oxidation	Use of the 'right 'polymers
• Low ionic resistance	High porosity, structure as open as possible
• High electrical resistance	Non conductive material
• Good barrier against particles released/grown from/at the electrode	Small pores. Structure as closed as possible
• Mechanical support of electrodes during cycling; no mechanical release of active material particle	Compressive material
• High absorption rates of the electrolyte (initial wettability)	Use the 'right' polymer wetting agents and/or post-treatment
• Permanent wettability for the electrolyte	Use the 'right' polymer post-treatment
• High absorption capacity of the electrolyte (reservoir effect)	'Right' structure
• Good mechanical strength	Strong fibers, good bonding

Table 2.3: Basic requirements for battery separators, from Cook et al.

For alkaline batteries, polyolefin materials are the most used for separator manufacture. But they are not inherently wetable by aqueous electrolytes. Therefore their surface is generally modified with surfactants or graft-copolymerized with monomeric substances which allow the alkaline solution to wet the membrane. However, these substances or surfactants can be very sensitive to the environment. As an example, they can be removed when the separator is exposed to dryness for long after it has been wet. This can actually occur in battery when the electrolyte is consumed or gas is trapped at the interface, or the distribution of the electrolyte is not homogenous across the membrane surface, etc…. Once the wetting agents are removed the separators do not wet again, resulting in an increase of the cell impedance and/or an enhancement of the shape change and dendrite formation due to the disturbance of the current density distribution.

Another challenge faced with separator is that several membrane layers are necessary to efficiently prevent a premature failure due to dendrite perforation. This gives rise to significant increase in the internal resistance.

Chapter 3

Experimental

3.1 Chemicals and apparatus

3.1.1 Button cell construction

The zinc button cell mainly consists of an anode cup, a cathode lid and a multi-layer separator stack placed at the interface to isolate the anode from the cathode.

The anode cup is of a tri-clad metal sheet consisting of a stainless steel sheet laminated between a nickel and a copper sheet. The copper faces the interior of the cup. The anode cup hosts the gelled zinc paste which is composed of a granulated zinc powder mixed with electrolyte and some gelling agent. The gelling agent ensures a homogenous distribution of electrolyte throughout the paste mass while maintaining good particle to particle contact between the zinc grains.

The cathode lid hosts the air electrode and the air diffuser. The air electrode comprises a catalyst layer, a metal mesh, a hydrophobic gas diffusion layer. The active layer is a blend of carbon, Teflon and catalyst to support the oxygen reduction and evolution reaction. The gas diffusion allows an even supply of the air across the active layer surface while serving as a barrier to H_2O and CO_2 exchange between the cell and its environment. The lid has two holes for the air access.

The multi-layer separator stack consisting of polyolefin microporous and non-woven membranes prevents any dendrite penetration while ensuring good ionic transport. The separators are laminated onto the active layer of the air electrode.

The lid and cup are assembled by crimping. A plastic gasket is used as an insulator between the two parts. A schematic description is given in Figure 3.1.

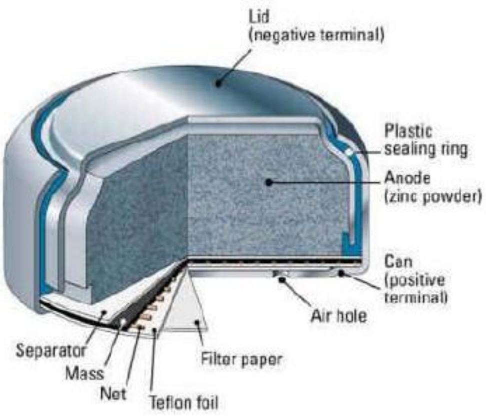

Figure 3.1: Cutaway view of a zinc-air button cell.

3.1.2 Electrochemical cell setup (plate electrode)

A conventional three-electrode cell made of PMMA block was used, as illustrated in Figure 3.2. Both the working and the counter electrodes were made of the same zinc plate. The working electrode was mounted and seal-pressed against one of the cell walls with an open window for the reaction of 1cm^2 area. A silver tab was attached to it and served as the terminal connector. The counter electrode was mounted on the cell wall opposite and parallel to the working electrode, with an open window of 15cm^2 for the reaction. Silicon rubber and screw bolts were used to tightly seal the cell. A zinc wire (Grillo, 99.99%) housed in a heat-shrinking-tube was used as the reference electrode. The Reference electrode was placed in a side room separated from the main chamber by a fine porosity glass frit.

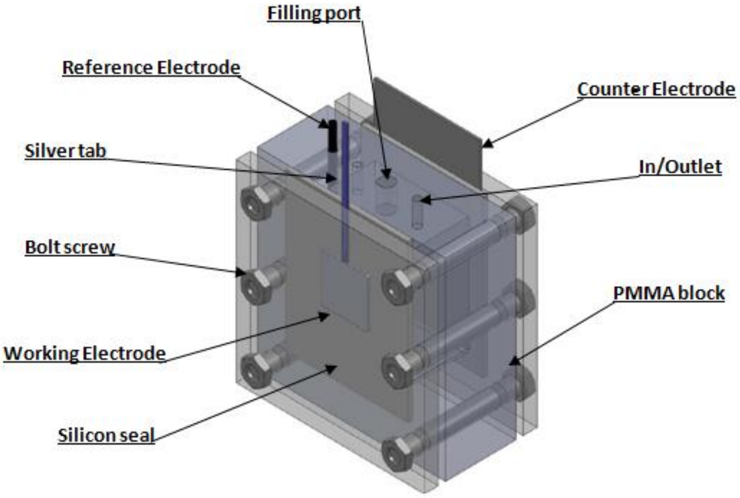

Figure 41: Three-electrode electrochemical cell.

3.1.3 Zinc Half cell setup (porous electrode)

The test vehicle mainly comprised a zinc container consisting of a PVC back chamber plate (2.5 cm X 4.0 cm) hosting the zinc electrode and a PVC front window plate. A copper strip serving as a current collector, on which a zinc paste was coated, constituted the electrode. A microporous PE/PP separator (3.0cm X 5.0cm) was placed on the zinc electrode in such a way to cover up the entire chamber area of 10cm^2 while poking out at the edges. A perforated sheet of the same dimension as the separator (60% opening and 0.2mm thick) was intimately positioned on the top of the separator in order to maintain a steady pressure on the electrode while allowing for the electrolyte permeation. A silicon rubber and a PVC front-window plate were used with plastic bolt screws to seal the whole unit, as illustrated in Fig 3.3-a. The cell as built was then placed inside a PP container with a zinc reference electrode placed near it and facing an air-electrode of higher 'geometric' surface area (1.5 times as large as zinc). The chamber had a venting/filling port and was filled out with 20ml of electrolyte. Fig 3.3-b gives a schematic representation on the complete setup. The open window for reaction was designed to be 10cm^2.

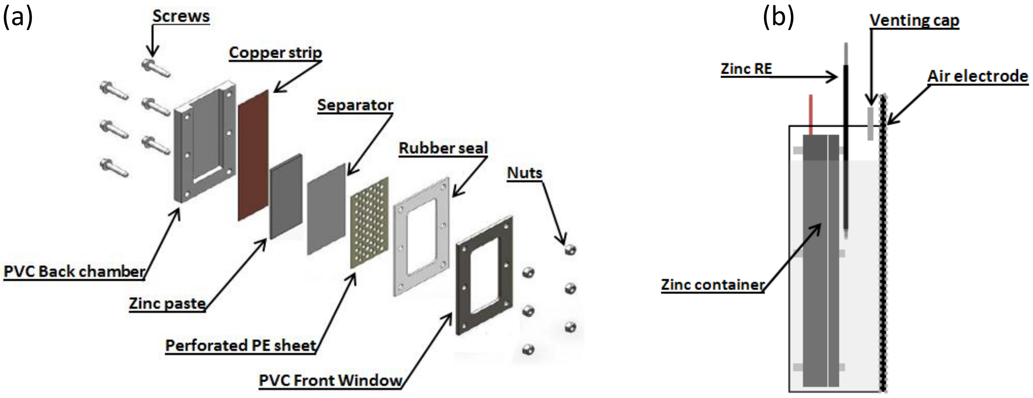

Figure 3.3: Half-cell setup for the porous zinc electrode: (a) PVC zinc container; (b) complete test setup.

3.2 Electrochemical measurement

3.2.1 Steady state polarization

The steady state behavior is obtained by polarizing the electrode under equilibrium conditions. The measurement can be performed either by controlling the current (galvanostatic control) or the potential (potentiostatic control) while recording the response in potential or current. The variation of the potential or current is done in small increments and the response is measured after several minutes when all transitory processes associated with changes in current or potential have ended. Relatively slow changes in a system's condition such as gradual decreases in reactant concentration are not taken into account. The currents measured in steady state are purely faradaic.

Steady state polarization measurement includes the following polarization effects:

- Thermodynamic potential (Reversible potential)
- Overpotential due to the surface reaction on electrodes (activation potential)
- Concentration overpotential
- Ohmic losses

So, the potential applied E_{cell} at a given rate is given by the equation:

$$E_{cell} = E_o + \eta + i.R_{\Omega} \tag{3.1}$$

where R_{Ω} is the Ohmic loss resistance in the electrodes, electrolyte, cable connections and wires and E_o is the cell potential at rest. The electrode overpotential η can be divided into the anodic part η_a and the cathodic part η_c (see Tafel equations):

$$\eta = \eta_c - \eta_a \tag{3.2}$$

By polarizing an electrode, e.g. in the anodic direction and measuring the potential versus a reference electrode, the cathodic contribution can be neglected and Equation 3.1 can be written:

$$E_{cell} = E_o + b_a \log\frac{i}{i_o} + i.R_{\Omega} \tag{3.3}$$

$$= E_o' + b_a \log i + i.R_{\Omega}$$

Where,

$$E_o' = E_o + b_a \log i_o \tag{3.4}$$

At low current densities where R_{Ω} can be neglected, b_a and E_o' can be found from the slope of the curve 'E vs logi'. However, the measurement is generally difficult in these conditions of low current densities because of longer transitory processes. For high current densities the data must be corrected from the ohmic drop. In this latter case the measuring time should be longer than the time needed to set up steady concentration gradients if the high current causes surface concentration changes.

3.2.2 Cyclic voltammetry

Cyclic voltammetry is a surface sensitive technique where each material gives rise to a unique spectrum in a given medium. The method is often applied to determine the physio-chemical state of an electrode surface. CV is useful to study the behavior of adsorbed species, participating as reaction intermediates in a given reaction or as impurities, as well as redox couples in the solution and at the electrode surface.

Cycling the potential at different scan rate can be performed to find the diffusion coefficients of the electroactive species and the capacitance of an electrode (active surface area). Additionally, CV can give information about the reversibility of the charge/discharge process [84].

In CV the potential is swept at a certain rate, ν, within the potential range of interest and the current response is measured. The results are usually reported as the potential dependence of current, or plots of i vs. E. The potential at a given time can be written:

$$E_t = E_{t=0} \pm \nu . t \tag{3.5}$$

Where t is the time, E_t is the controlled potential, $E_{t=0}$ is the starting potential and plus and minus indicates the anodic and cathodic direction of the sweep, respectively.

Unless the potential scan rate is very low, the system has generally no time to reach the steady state. The reactant surface concentration is higher than that of the steady state, resulting in higher current [85]. The current begins to decrease when the reactant surface concentrations drop down, forming waves with maxima appearing in the i vs. E curve. The corresponding current and voltage at the maxima are defined as current peak i_p and voltage peak, respectively.

The value of the current peak for a reversible process at a planar electrode is found to be:

$$i_p = (2.69 \times 10^5) n^{3/2} A D_o^{1/2} C_o \nu^{1/2} \tag{3.6}$$

The potential peak value is independent of the concentration of the electroactive species and scan rate. It is shifted relative to half wave potential $E_{1/2}$ as given in Equation (3.7).

$$E = E_{1/2} \pm \frac{0.028}{n} \qquad (3.7)$$

Table 3.1 shows some diagnostic criteria to determine the reversibility of a charge transfer reaction without diffusion or activation limitations.

1.	$\boldsymbol{i_p \propto \nu}$
2.	$i_p^a / i_p^c = 1$
3.	$\Delta E_p = E_p^a - E_p^c < 59/n\ mV$
4.	E_p independent of ν

Table 3.1: Criteria for reversible reactions without diffusion limitations.

3.2.3 AC impedance

In AC impedance measurement a small sinusoidal voltage perturbation is superimposed on a fixed potential or current, and the response in current is measured [86]. The voltage perturbation is typically applied over a wide frequency range, e.g. 1MHz to 1mHz, where different surface phenomena may give rise to response in different region of the frequency window. The technique relies on the supposition that electrochemical systems behave linearly under sufficiently small potential perturbations, usually about ±10mV.

The voltage perturbation E_t with an amplitude of E_m and angular frequency ω ($\omega = 2\pi f$, where f is the ac frequency) is given in Equation 3.8.

$$E_t = E_m \sin(\omega t) \qquad (3.8)$$

The current response, I_t , will be a sinusoidal function of the voltage perturbation with a phase shift (θ) and a different amplitude (I_m), as given in Equation 3.9.

$$I_t = I_m \sin(\omega t + \theta) \qquad (3.9)$$

The relation between current and voltage can be visualized in Figure 3.5 where the current is shifted by θ. The magnitude of the impedance is given as the ratio between E_t and I_t:

$$|Z_\omega| = \frac{E}{I}(\omega) \tag{3.10}$$

The impedance can be expressed as a vector on complex form by Equation 3.11 and plotted as rectangular coordinates as shown in Figure 3.4.

$$Z_\omega = Z' + jZ'' \tag{3.11}$$

It can be seen from Figure 3.4 that the rectangular coordinate values are:

$$Re(Z) = Z' = |Z| \cos\theta \tag{3.12}$$

$$Im(Z) = Z'' = |Z| \sin\theta \tag{3.13}$$

With the phase angle:

$$\theta = \tan^{-1}\frac{Z''}{Z'} \tag{3.14}$$

And the impedance modulus:

$$|Z| = [(Z')^2 + (Z'')^2]^{1/2} \tag{3.15}$$

Equation 3.15 can be used for the representation in a complex plane, which results in a semicircle curve. Such a representation is called Nyquist diagram.

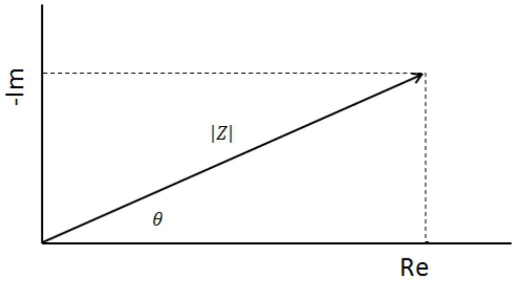

Figure 3.4: Complex plan plot.

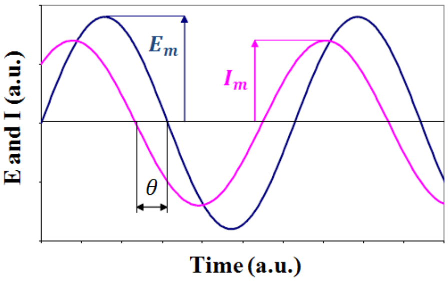

Figure 425: Sinus variation of E and I as a function of time.

The AC impedance behavior can be modeled to conventional electrical circuits consisting of passive components, e.g. ohmic resistor (R), capacitance (C) and inductance (L). The impedance of the real and imaginary parts of the different circuit elements are summarized in Table 3.2.

	$\boldsymbol{Z}$	$\boldsymbol{Z'}$	$\boldsymbol{Z''}$
R	Z_R	R	-
C	Z_C	-	$1/_{jC\omega}$
L	Z_L	-	$jL\omega$

Table 3.2: Equivalent circuit elements.

The simplest circuit proposed for a planar electrode supporting a simple one-step redox reaction of the type Ox + ne- = Red is the so called Randles circuit and it is shown in Figure 3.6 where R_Ω is the ohmic resistance (solution and cable connections, etc…), R_{ct} is the charge transfer resistance and C_{dl} is the double layer capacitance. The impedance of the circuit can be written as:

$$Z = Z_{R_\Omega} + (Z_{R_{ct}}^{-1} + Z_{C_{dl}}^{-1})^{-1} \qquad (3.16)$$
$$= R_\Omega + [R_{ct}^{-1} + \left(\frac{1}{jC\omega}\right)]^{-1}$$

By manipulation of Equation 3.16, the impedance can be written as:

$$Z = R_\Omega + \frac{R_{ct}}{1+(C\omega R_{ct})^2} - j.\frac{C\omega R_{ct}^2}{1+(C\omega R_{ct})^2} \qquad (3.17)$$

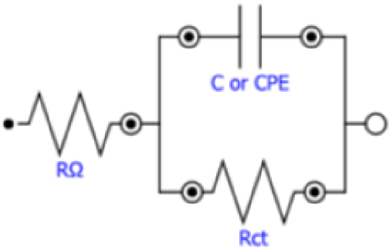

Figure 436: Randles equivalent circuit model.

It can be seen from Equation 3.17 that when $\omega \rightarrow \infty$, $Z \rightarrow R_{\Omega}$. When $\omega \rightarrow 0$, $Z \rightarrow R_{\Omega} + R_{ct}$. The electrode reactions generally have several mechanistic steps, and are rate limited by mass transfer or include insoluble species. In such cases the equivalent circuits can be complex and will in general require more passive components. Equivalent circuit models can be developed for a given reaction, and the model can be evaluated by fitting the model to the measured data. Physical quantities of the electrode process can therefore be determined. Fitting procedure of impedance data are implemented in most impedance software program.

a. Graphical representation

The impedance results can be graphically represented in the Nyquist complex plan or using the Bode plot, as shown in Figure 3.7-8. The Bode plot represents the variation of the impedance magnitude and phase as a function of frequency. Nyquist plots are the most often used in the electrochemical literature because they allow for an easy prediction of the circuit elements. The angular frequency at the maximum of the curve $\omega_0$is given by Equation 3.18.

$$\omega_0 = \frac{1}{R_{ct}C_{dl}} \tag{3.18}$$

R_{ct} corresponds to the diameter of the semi-circle and C_{dl} can be found from $\omega_0$and $R_{ct}$by using EqXXX. The total polarization resistance is given by the intercept between the curve and the real axis as $\omega \rightarrow 0$.

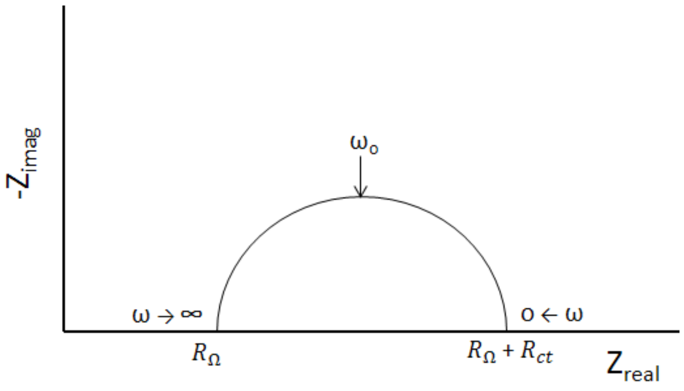

Figure 3.7: Nyquist plot.

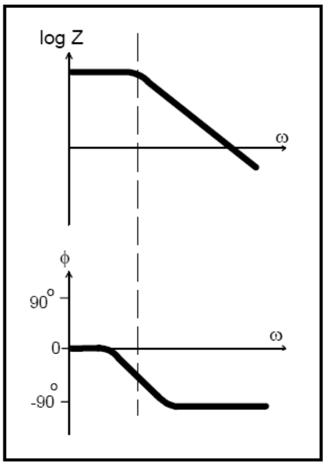

Figure 44: Bode plot.

b. Warburg Impedance

Diffusion can create impedance called the Warburg-impedance. The impedance depends on the frequency of the potential perturbation. At high frequencies the Warburg impedance is small since diffusing reactants don't have to move very far. At low frequencies the reactants have to diffuse farther, increasing the Warburg-impedance. The equation for the "infinite" Warburg impedance is:

$$Z_W = \sigma(\omega)^{1/2}(1-j) \qquad (3.19)$$

where σ is the Warburg coefficient.

On a Nyquist plot the Warburg impedance appears as a diagonal line with a slope of 45°. On a Bode plot, the Warburg impedance exhibits a phase shift of 45°.

c. Constant phase element (CPE)

Rough and porous electrode surface may give rise to a depressed semicircle in the Nyquist diagram, caused by the surface inhomogeneity [86].

The impedance of a CPE element can be expressed as:

$$Z_{CPE} = \frac{1}{B(j\omega)^{\alpha}} \qquad (3.20)$$

Where B is a frequency-independent term and α is a value between 0 and 1. For α = 0, Z_{CPE} is a pure resistor, for α = 0.5 a Warburg element and for α = 1 a pure capacitor. In the latter case B represents the capacitance. The Warburg element characterizes the diffusion of the electroactive species from and to the electrode.

3.2.4 Quartz Crystal Microbalance

The Quartz crystal microbalance measurement technique relates to the sensitivity of piezoelectric devices towards mass changes at the surface of the QCM electrodes. Sauerbrey [87] was the first to recognize the potential usefulness of QCM.

The relation between the mass change per unit area at the QCM electrode surface and the observed change in oscillation frequency of the piezo crystal is given by the Sauerbrey equation:

$$\Delta f = -C_f.\Delta m \qquad (3.21)$$

where Δf is the frequency change in Hz, Δm is the change in mass per unit area in g/cm^2 and C_f is the sensitivity factor for the crystal (56.6 Hz µg^{-1}cm^2 for a 5 MHz AT-cut quartz crystal at room temperature).

The Sauerbrey equation is only strictly applicable to uniform, rigid, thin-film deposits [88]. Calibration is generally required for systems that fail to fulfill any of these conditions in order to obtain accurate frequency-mass correlation results. The system is also highly sensitive to vibration and temperature.

The sensitivity factor is a fundamental characterisitc of the quartz crystal as it is only dependent on the quartz acousto-elastic properties. Its value is given by:

$$C_f = \frac{2nf_o^2}{(\rho_q \mu_q)^{1/2}} \qquad (3.22)$$

Where

n: Number of the harmonic at which the crystal is driven

f_o: Resonant frequency of the fundamental mode of the crystal in Hz

ρ_q: Density of the quartz

μ_q: Shear modulus of quartz

QCM can be used in liquid phase. The change in resonance frequency resulting from immersion of the crystal into a viscous medium, Δf, was studied by Kanazawa and Gordon**[89]**.

$$\Delta f = f_U^{3/2} (\frac{\rho_L \eta_L}{\pi \rho_q \mu_q})^{1/2} \qquad (3.23)$$

The apparatus is from Stanford Research System (SRS) and consists of a QCM200 controller, a QCM25 Crystal oscillator and a crystal holder housing the sensor crystal, as illustrated in Figure 3.9.

The sensor crystal used by the QCM200 system consists of a thin disk of 5MHz, AT-cut, α-quartz with circular electrode patterned on both sides. Figure 3.10 shows the different components of the sensor holder. The sensors were provided by SRS.

Figure 3.9: Quartz crystal microbalance apparatus.

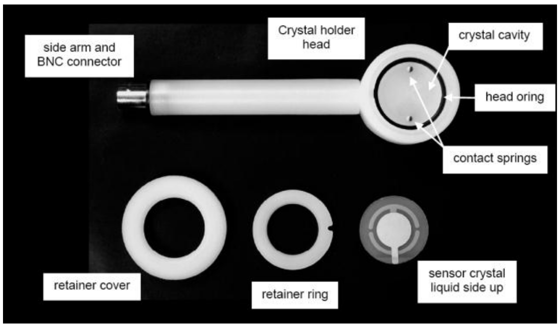

Figure 3.10: Components of the quartz crystal holder.

Chapter 4

Zinc alloys stability in rechargeable electrodes

Abstract

The stability of Pb and In used as alloying elements in Zn was investigated in rechargeable electrode. The impact of the discharge and charge on the alloys was examined using SEM-EDS as well as ICPMS for the quantitative analysis. The data suggest that Pb dissolves during the discharge and does not replenish during the charge. It is also demonstrated that In exhibits different characteristic as it seems to resist to the anodic polarization. The inhomogeneity of the alloy surface redistribution upon subsequent cycles seems to be the major challenge.

4.1 Introduction

In alkaline zinc cells, the inhibition of zinc corrosion has always been of primary importance. Amalgamation of zinc with mercury has been quite effective with this respect, but it has been banned due to its environmental toxicity. Other less or non-toxic alloying elements such as In, Pb, Bi, Ga, Al [25] have been used in zinc alloys. One shortcoming associated with the use of alloys in rechargeable zinc cells is the stability of the alloys upon subsequent cycles. Some alloys may dissolve or oxidize during the discharge and may not reform during the charge. Moreover, the bulk surface of electrodes can increase up to ten folds or more with cycling, altering the alloy distribution at the surface of zinc particles as a result.

In this section, we have investigated the behavior of the indium and lead alloys in zinc when the electrode is discharged and charged. In addition, we examine the gassing performance of the electrodeposited zinc mass.

4.2 Experimental

<u>Preparation of the zinc electrode</u>

Zinc powder (alloyed with 500ppm lead and 300ppm indium, Grillo) of size ranging from 30 to 200µm was mixed with 1wt% Teflon PTFE (6C-N, DuPont) and1wt% Carbopol C940. A porous paste was obtained by adding 7M KOH solution to the mix. 5g of the paste was then pressed onto a copper sheet serving as the current collector. The electrode as built was assembled in a zinc half-cell setup according to the description in section 3.1.3.

<u>Measurement of the electrochemical performances</u>

The cell was discharged and fully charged at constant current density of 20mA/cm^{-2}. The discharge capacity was about 75% of the theoretical input. The discharge and charge cutoff voltages were set at 0.3V and-0.15V vs. Zn reference electrode, respectively.

<u>SEM-EDX analyses</u>

The study of the surface morphology and composition of the fresh, discharged and deposited zinc crystals was carried out in a Zeiss Ultra scanning electron microscope (SEM). The chemical analyses were performed with a Pegasus energy dispersive X-ray spectrometer (EDX) built in the SEM.

ICPMS analysis

The Inducted coupled plasma mass spectroscopy was used to quantitatively analyze the electrolyte composition of the cell at different stages of the cell life. To this respect the electrolyte was sampled out fresh, after discharge and after charge. The analyses were conducted with a HPLC-ICPMS Agilent 7500ce apparatus.

4.3 Result and discussion

4.3.1 Surface analysis

Figure 4.1 shows the surface morphology of the fresh zinc powder. Initially, the particles exhibit an elongated shape of various forms. The presence of shiny precipitates localized at the grain boundaries is illustrated in Figure 4.2. The chemical analysis by EDX is shown in Figure 4.3 (a) and (b) and it reveals that the shiny precipitates are Pb and In, whereas the center of the grains consists mainly of zinc.

Powdery zinc is generally produced by striking an atomizing medium emitted from a nozzle against a molten zinc alloy stream. Initially the alloys are evenly distributed in the zinc melt. The result indicates a case of segregation of alloys in grain boundaries. Such segregation is not completely undesired since grain boundaries are generally the most active sites for hydrogen reaction and are the preferred location where impurities are hosted.

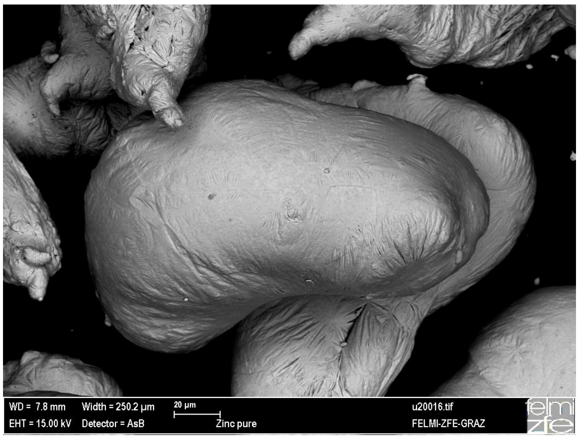

Figure 4.1: Zinc particle morphology.

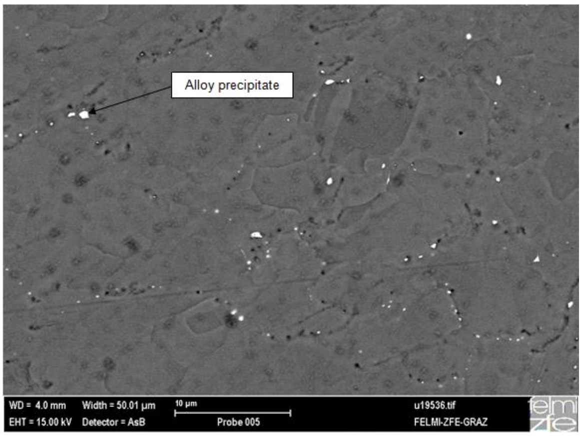

Figure 4.2: Incrusted In and Pb precipitates in the grain boundaries of zinc particle.

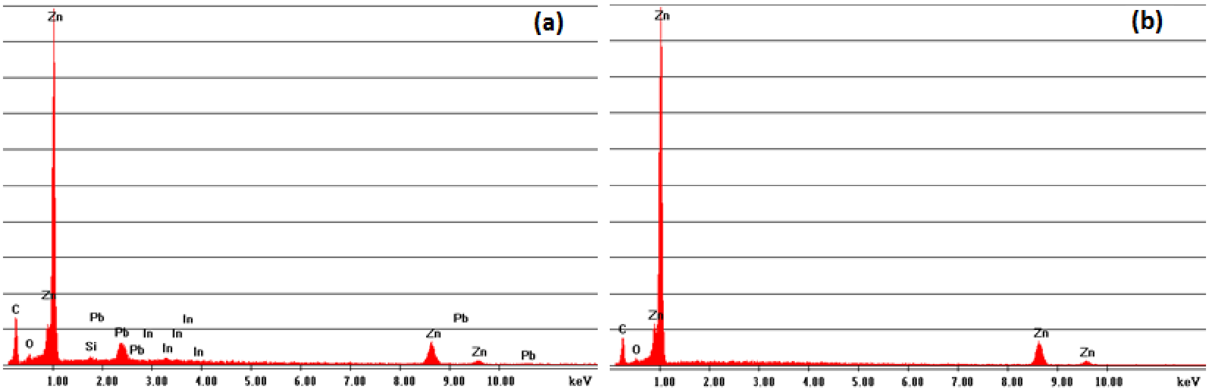

Figure 453: EDX spectrum for specimen consisting of zinc powder alloyed with In and Pb. Index: (a) precipitate at the grain boundary (b) center of grain.

The SEM picture of discharged zinc is shown in Figure 4.4 (a) where a highly porous structure consisting of shells is presented. During discharge, zinc particulates are consumed to form ZnO shells which, in some cases keep the same foot print as the original particles. Highly consumed shells are empty in their core whereas the core of partial consumed shells consists of un-reacted zinc. A close-up SEM image of an un-reacted core is presented in Figure 4.4 (b). It is shown that the core has an etched surface on which the dissolution reaction seems to have preferably started at the alloy location at the grain boundaries.

A higher magnification of the ZnO discharge product is illustrated in Figure 4.4 (c). It is found that the alloy precipitates remain in the porous ZnO skin. This is confirmed by the EDS analysis shown in Figure 4.5. The alloys may be in an oxidized state upon the discharge, accounting for the presence of an oxygen peak in the spectrum. Note that oxygen may as well come from ZnO in the surrounding.

A closer observation shows that the alloy precipitates are distributed across the two distinct ZnO layers constitutive of the shell skin, as illustrated in Figure 4.4 (d). The structure and formation mechanism of the apparent two oxide layers are discussed in section 2.2.

The SEM analysis was also performed on zinc deposits resulting from charge. The deposited zinc exhibits a fine and flaky structure and its surface shows no alloy precipitate, as illustrated in Figure 4.6 and Figure 4.7, respectively.

The absence of the alloy precipitates indicates that lead and indium are not electrodeposited during charge, which results in a non-uniform alloy distribution across the bulk surface. Furthermore, the fine structure of the zinc deposits gives rise to significant increase of the electrode bulk surface area. The uneven distribution of alloys and the increase of the electrode surface area are the major causes of the corrosion enhancement of rechargeable zinc electrodes.

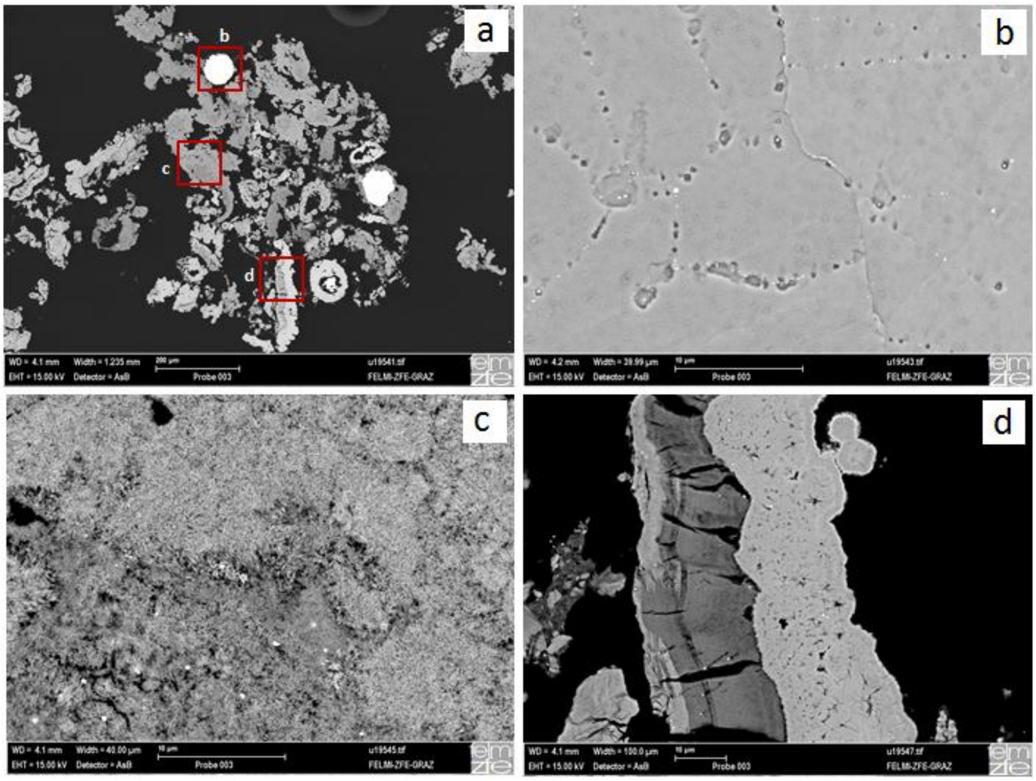

Figure 4.4: SEM picture of zinc after a full discharge of the cell: (a) powder agglomerate, (b) etched surface of un-reacted zinc core, (c) porous and flocculent zinc oxide, (d) layered structure of particle

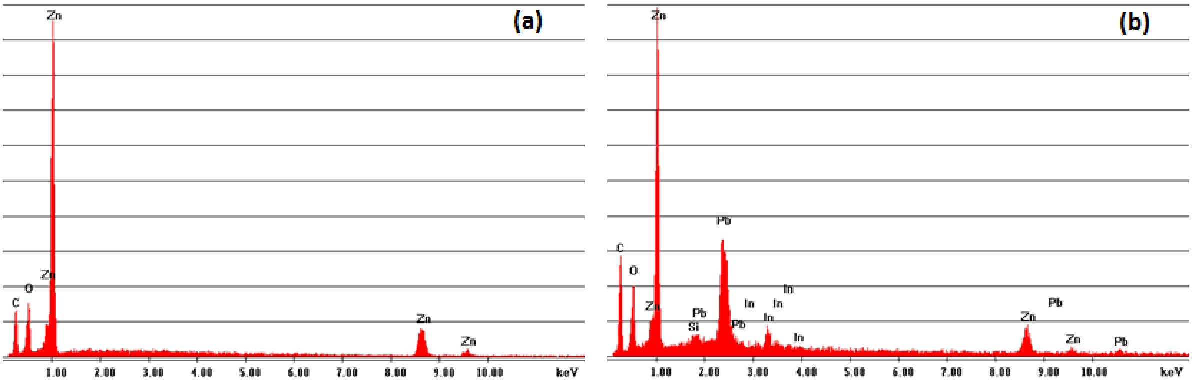

Figure 4.5: EDX analysis of the zinc discharge product: (a) zinc oxide, (b) alloy precipiates

Figure 4.6: Morphology of the zinc deposits in charge.

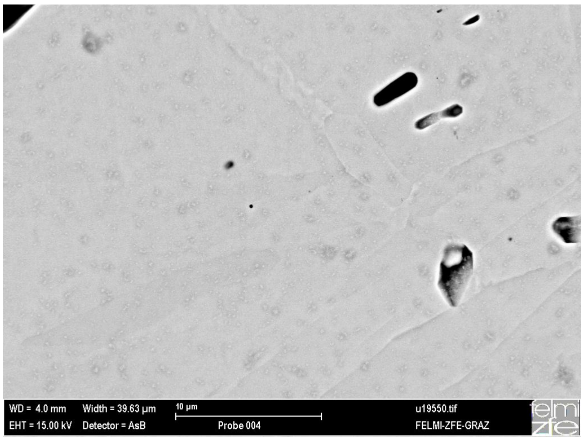

Figure 4.7: SEM picture of the surface of fresly deposited zinc in charge.

4.3.2 Electrolyte analysis (ICPMS)

The ICPMS analysis of the fresh, post-discharge and post-charge electrolytes was performed. The results show a negligible concentration of indium and lead in the fresh electrolyte (smaller than 0.01ppm). After discharge, the indium concentration remained negligible whereas that of lead increased up to 13.7ppm. The cell was filled up with 70g of electrolyte, yielding a total lead mass of 0.001g dissolved in the electrolyte. The electrode comprised 3 g of zinc. Knowing that the lead content in the zinc raw powder was 500ppm, the total amount of lead in the electrode was then calculated to be 0.0015g. Therefore, the data suggest that about 70% of lead dissolved in the electrolyte during the full discharge of the electrode.

The analysis of the post-charge electrolyte reveals that the lead concentration in the solution is not affected by charge as a concentration of 14ppm was recorded. Thus, Pb and In alloys are not replenished in zinc reformed in charge. This is consistent with the observations made with SEM-EDX. The data are summarized in Table 4.1.

	Solution before discharge	*Zn mass before discharge*	*Replenished Zn mass in charge*	*Solution after discharge*	*Solution after charge*
Pb	< 0.01ppm	500 ppm	< 0.10 ppm	13.7 ± 0.2 ppm	14 ± 0.2 ppm
In	< 0.01ppm	300 ppm	0.57 ± 0.01 ppm	< 0.01ppm	< 0.01ppm

Table 4.1: Table summary of the results from the ICPMS analysis of indium and lead alloys in the zinc mass and electrolyte.

4.4 Summary

Alloying Zn as a mean to suppress gassing in rechargeable cells proves to have some limitations. The dissolution of the alloys or their inhomogeneous redistribution on surface upon subsequent cycles points out to the necessity to resort to different inhibitor types. That is reason why it is very common to use alloys in combination with salts or organic substances that inhibit the corrosion of the zinc active mass and reduce the cell gassing rate as a result.

Chapter 5

Hydrogen Overpotential during the zinc electrodeposition on copper

Abstract

Hydrogen evolution during electrodeposition of a thin zinc film on a copper substrate was studied. The effect of the overpotential was investigated by galvanostatic and potentiostatic techniques in association with the electrochemical quartz microbalance. The amount of hydrogen was deducted from the charge columbic efficiency which was obtained by combining cathodic and anodic polarization techniques. The method proved to be an efficient tool to study the electroplating mechanism in which zinc nucleation and growth are addressed. EIS was used to measure the cell impedance.

5.1 Introduction

Hydrogen evolution reaction (HER) during zinc electrodeposition in alkaline zincate solutions has long been studied. Corrosion, electrowinning and battery technology are three examples of field in which many research works have been carried out in order to fundamentally understand the HER mechanism. Electrodeposition is generally a diffusion-controlled process [90]. Thus, current density distribution, composition of the electrolyte and morphology of the substrate play major role.

Various methods have been applied to quantify the amount of hydrogen evolved in a reaction; among them, the volumetric and weight loss measurements are probably the two most commonly used. Numerous studies mostly in zinc corrosion have been reported. Szczesniak et al [91] have investigated the effect of some alloys on the corrosion of zinc based on gas-collection method.

Other method such as manometric technique has been used by L. Binder et al [92] to investigate the zinc corrosion at rest in rechargeable alkaline manganese dioxide batteries. However, such technique can only be applicable for sealed-tight systems.

The rotating ring disk electrode (RRDE) has also been used to quantify the hydrogen evolution of a reaction. The accuracy of RRDE relies on two main factors which are the experimental collection efficiency and H_2 solubility. The collection efficiency varies with electrolyte concentration and disc current density which renders its determination delicate. Moreover, the maximum ring current depends on the rate of the dissolved gas. Therefore, the solubility of H_2 in the electrolyte sets the upper limit for which the RRDE can be applied.

R.E.F Einerhand et al [93] studied the hydrogen production during zinc deposition for various alkaline zincate electrolytes with a rotating ring disk electrode (RRDE). They found that hydrogen production during electrodeposition is very small and increases with decreasing zincates and KOH concentration.

In the study carried out by K.D. Song et al [94] an electrochemical quartz microbalance (EQCM) was used to investigate hydrogen evolution and absorption during zinc metal deposition. The goal was to distinguish between the charge required for Zn deposition and the hydrogen reduction reaction separately. But the high sensitivity of EQCM can easily lead to inaccuracy in the measurement of the resonant frequency and resistance.

T. Trisovic et al [95] found in their work that a combination of classical potentiostatic steady-state voltammetry (PSV) and electrochemical impedance spectroscopy (EIS) can help study the reaction mechanism of HER.

In the present work, potentiostatic and galvanostatic techniques were used to quantify the hydrogen evolution rate. The techniques proved to be satisfactory enough to allow us to study the growth mechanism of zinc crystal on a copper substrate.

5.2 Experimental

5.2.1 Electrode and cell preparation

An in-house-built and sealed cell, similar to that described in section 3.1.2 was used with the exception that the working electrode (WE) was made of copper. The WE pad was cut out of a copper sheet and was thoroughly cleaned with acetone in an ultrasonic bath prior to the cell assembly.

The electrolyte consisted of dissolved potassium hydroxide and zinc oxide in deionised water. All three compounds were Sigma Aldrich grade products. A solution of 7M KOH containing 1.7wt.% of dissolved ZnO was prepared. The cell was deaerated by bubbling oxygen-free nitrogen gas through the electrolyte.

5.2.2 Polarization techniques

The potentiostatic and the galvanostatic measurements were carried out with a battery tester instrument from Arbin at room temperature.

A constant cathodic voltage was applied to the cell, resulting in the deposition of a thin zinc film onto the surface of the working electrode from the zincates solution. The deposition was controlled by a capacity cut-off set at 3mAh. Immediately after deposition, the cell was anodically polarized until the complete dissolution of the deposited zinc layer. The anodic current density was set at 6mA/cm^2. The discharge capacity was recorded and the average current contributing to the hydrogen evolution reaction during the electrodeposition of zinc was deducted from Eq. (5.1), based on the assumption that the zinc corrosion was insignificant.

$$i_{H_2} = {(Q_c - Q_d)}/{t_c} \tag{5.1}$$

t_c is the deposition duration and Q_c and Q_d are the electrodeposition and the discharge capacities, respectively.

In order to investigate the hydrogen production rate as a function of the overpotential, the experiment was applied for various cathodic voltages ranging from 50 to 500 mV.

5.2.3 Electrochemical quartz microbalance (EQCM)

An EQCM was used to investigate the efficiency of the zinc electrodeposition by weight measurement, from the same solution as above using the same cell setup, RE and CE. The temperature was controlled and fixed at 24°C ±0.1 and the electrolyte was purged with nitrogen. The WE was 2.54 cm in diameter and consisted of a copper coated AT-cut quartz crystal with a nominal resonance frequency of 5 MHz from the Stanford Research System (SRS). The crystals back side was coated with gold and Chromium.

The instrument used was a QCM200 model from SRS that was interfaced with a potentiostat, as described in section 3.2.4. The weight measurement was related to the change in the resonance frequency by applying the Sauerbrey equation [96].

5.2.4 Electrochemical Impedance Spectroscopy (EIS)

Impedance measurements were carried out using a Solartron analytical 1400 cell test system. The cell assembly used was similar to that of the polarization measurement. The frequency range applied varied from 100 mHz to 1MHz at constant open circuit voltage with an amplitude of the A.C. signal of 10mV. The Nyquist plots were used to measure the internal resistance of the cell.

5.3 Result and Discussion

As on many metal electrode surfaces, the hydrogen evolves under cathodic polarization in alkaline solution according to Equation 2.7 and 2.8 which relate the overpotential η to the exchange current density i and the Tafel slope b.

According to Lee [31] the HER Tafel plots measured on a zinc electrode in 6 M and 9 M KOH solutions are linear and exhibit a slope of 124mV/dec, like most cases of metal electrodes in aqueous solutions [32].

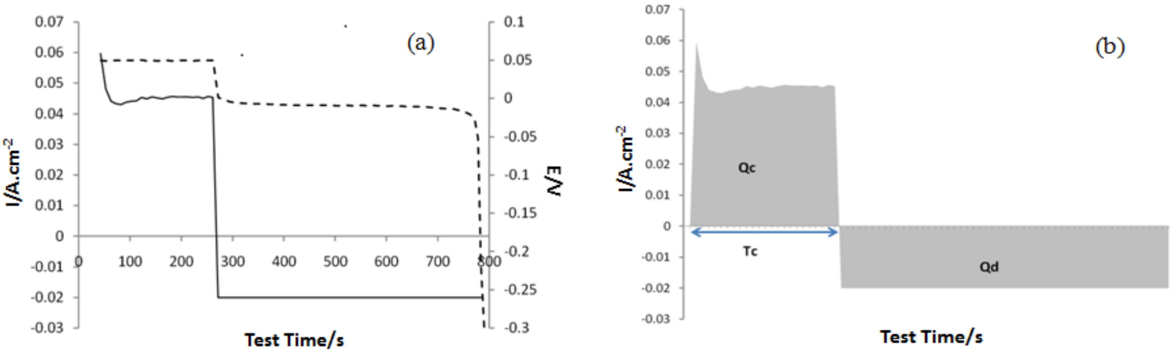

Figure 5.1: Electrochemical performance at 50mV overpotential: (a) Voltage (-----) and current (——) curve variation, (b) capacity variation as a function of the test time.

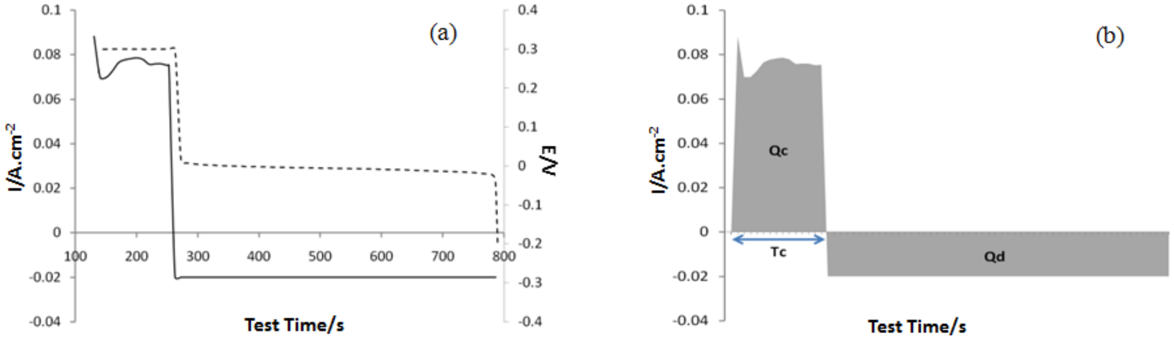

Figure 5.2: Electrochemical performance at 300mV overpotential: (a) Voltage (-----) and current (——) curve variation, (b) capacity variation as a function of the test time.

In order to investigate the hydrogen evolution rate, a zinc layer was deposited onto the WE at constant cathodic voltage with a capacity cut-off set at 3mAh. The WE was immediately fully discharged after the deposition completion. The discharge was performed at a constant anodic current of 20mA and controlled by a cut-off overvoltage set at -0.3V vs. Zn RE. The electrodeposition was performed at an overvoltage ranging from 50 up to 500mV vs Zn RE. Figure 5.1 (a) and Figure 5.2 (b) are two examples of the current and voltage curve variation during the potentio-galvanostatic experiment at 50 and 300mV overpotential, respectively. As predicted by the Tafel equation, the electrodeposition current at 300mV (7.5mA) is higher than at 50mV (4.5mA). The respective discharge (Q_d) and capacities (Q_c) are presented in

Figure 5.1 (b) and Figure 5.2 (b). The deposition capacity being fixed at 3mAh, the hydrogen evolution rate was calculated according to Equation 5.1.

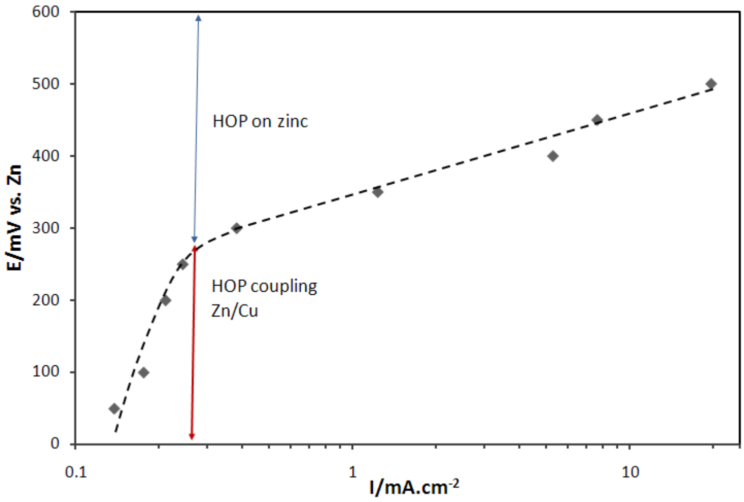

Figure 5.3: Tafel polarization curve for the HER during the Zn electrodepositon on copper in 7MKOH solution containing 1.7wt.% of dissolved ZnO at 24°C.

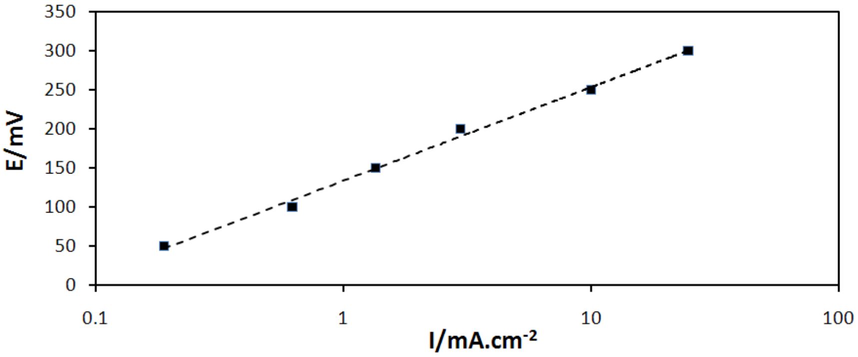

Figure 46: Tafel polarization curve for HER on copper substrate in 7M KOH solution at 24°C.

Figure 5.3 relates the variation of the hydrogen evolution current density to the overpotential. The resulted curve is characterized by two distinct Tafel slopes, indicating that the rate of the hydrogen evolution reaction varies from one region of overpotential to another. Therefore, the curve was split into two regions called ‘low’ and ‘high’ overpotentials. The ‘low’ overpotential that ranges from 0 to 250mV is characterized by a slope of about 860mV/dec, while the ‘high’ overpotential that starts from 250mV upward exhibits a slope of 120mV/dec.

In order to explain the origin of the two slopes exhibited in Figure 5.3, the hydrogen overpotential of the copper electrode was investigated by means of potentiostatic technique. The electrode was cathodically polarized at a constant overvoltage ranging from 50 to 300 mV vs a Zn reference electrode. The resulted steady state current at each voltage corresponded to the hydrogen evolution current. The experiments were performed in the electrochemical cell housing as described above and in 7M KOH solution free of zincates. During the experiment, nitrogen gas was purged through the solution to minimize the effect of oxygen evolving from the Nickel mesh used as the counter electrode.

As shown in Figure 5.4, the relation between the exchange current density and the hydrogen overpotential on the copper electrode is linear with a Tafel slope of 120mV/dec.

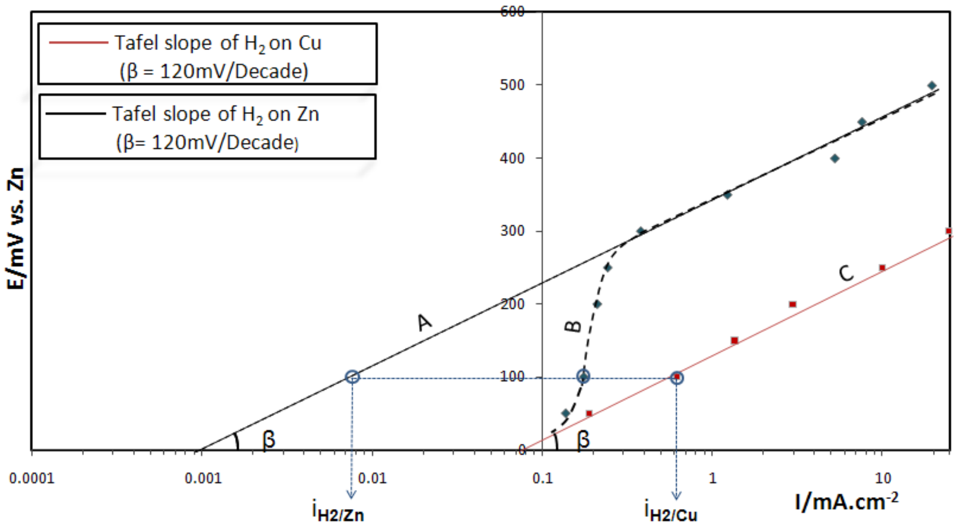

Figure 47: Tafel polarization curve comparison between the hydrogen overpotential on Cu surface in 7M KOH solution and that during the Zn electrodepositon on copper in 7MKOH solution containing 1.7wt.% of dissolved ZnO at 24°C.

By plotting the curves in Figure 5.3 and Figure 5.4 on a same graph, we were able to graphically represent the change happening in the system as a result of the zinc deposition across the wide range of overpotential, as illustrated in Figure 5.5.

It was found that the curve relating the hydrogen current density to the overpotential during the zinc deposition onto the copper substrate is split into two lines, namely A and B. Line A and B represent the Tafel slopes in the high and low overpotential regions, respectively. In the same Figure, the Tafel line of the hydrogen overpotential on the copper substrate is represented by line C.

Line A and C are parallel and exhibit an identical slope of 120mV/dec. This is concordant with Lee's findings [31]. Therefore, given that line C represents the hydrogen overpotential on copper surface, the results suggest that line A is representative of the hydrogen overpotential on zinc. The fact that line A is shifted up with respect to Line C indicates that zinc has higher hydrogen overpotential than copper.

Figure 5.5 also shows that lines C and B intersect; pointing out that the hydrogen production in the low overpotential region is influenced by the copper surface. Near the open circuit voltage, the copper substrate seems to have the strongest influence but as the overpotential increases the predominant contribution is progressively shifted to the deposited zinc layer. Therefore, the line B can be seen as a transition path from the pure copper surface (line C) to the fully zinc plated surface (line A). Note that the contribution of cell internal resistance to the polarization voltage was measured using an EIS and was found to be negligible since its value averaged 40mΩ at the open circuit potential.

If copper can influence the hydrogen evolution rate in the low region of overpotential, it indicates that a fraction of the substrate surface may not plate during the deposition process. In other words, the deposition is non-uniform and its efficiency is low.

In order to strengthen the interpretation and to validate the results yielded by means of potentio-galvanostatic experiments, a different technique was used to assess the electrodeposition efficiency. The variation of the deposition efficiency as a function of the charge current density was investigated by measuring the weight of the zinc deposits onto an EQCM working electrode. The current density window ranged from 0 to 15mA/cm^2. An example of the graphical representations of the variation of the resonance frequency and deposited mass, for the deposition rate of 0.2 and 6mA/cm^2, is given in Figure 5.6 (a) and (b), respectively. The technique operates with measuring the variation of the resonance frequency of the working electrode which is converted into the mass change. At the beginning, the steady state resonance frequency of the WE is recorded for a short period of time and paused at 'start'. Then, the deposition process is launched while the frequency measurement is paused. Once the deposition is over, the frequency measurement is resumed at 'end', giving rise to a different steady state resonance frequency.

Figure 5.6 also shows the mass change (Δm) recorded through the deposition process. Δm is calculated using the Sauerbrey model. The deposition efficiency was obtained by dividing the experimental deposited mass by the theoretical mass corresponding to the quantity of electricity of the electrodeposition, as illustrated in Figure 5.7.

The Sauerbrey equation relates the variation of the resonance frequency and the mass change as follows:

$$\Delta f = -\frac{2f_0^2}{A\sqrt{\rho_q \mu_q}}\Delta m \tag{5.2}$$

f_0 is the resonance frequency, Δf and Δm the frequency and mass change, respectively. The active area of the piezoelectric crystal is represented by A, while ρ_q and μ_q are the density and the shear modulus of the quartz for AT-cut crystal, respectively.

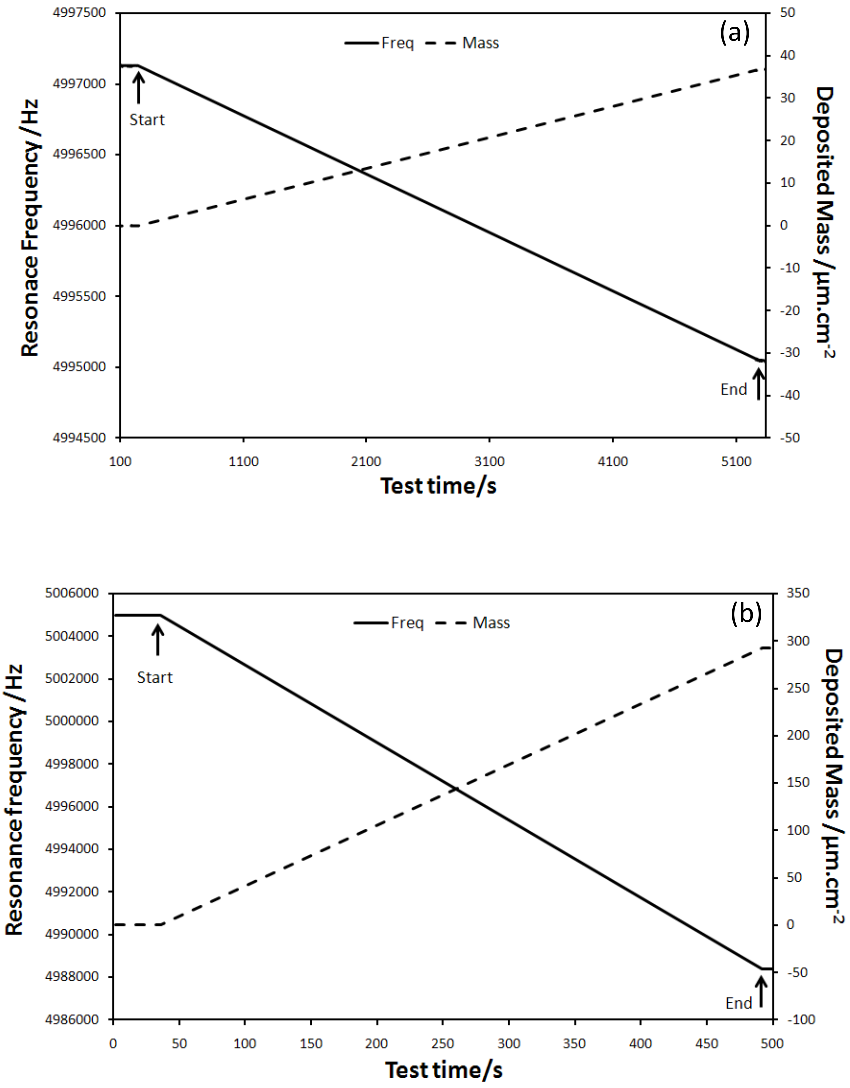

Figure 5.6: Variation of the resonance frequency and deposited mass on the EQCM quartz crystal at 0.2mA/cm2 (a) and 6mA/cm2 (b) deposition rate.

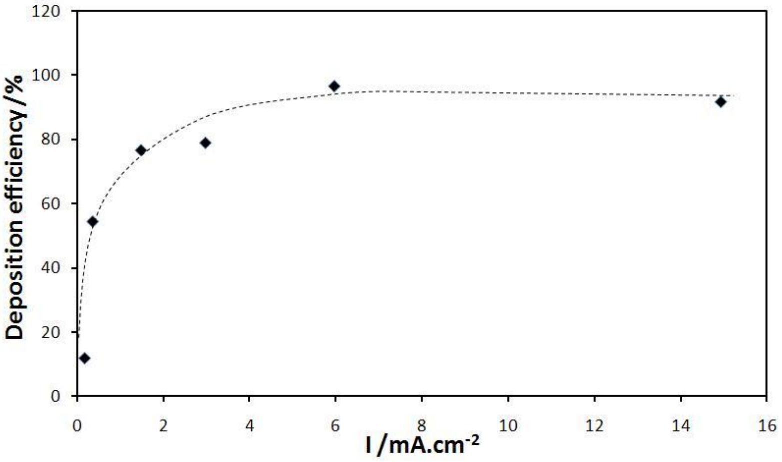

Figure 48: Efficiency curve of the Zn electrodeposition on a 5MHz-QCM crystal in 7MKOH containing 1.7wt.% of dissolved ZnO at 24°C.

At very low current density, only a small fraction of the current seems to contribute to the effective deposition of zinc; we believe the remaining large fraction to be consumed in the HER. The efficiency increases with current density. This result corroborates the observed trend obtained by combining the potentiostatic and galvanostatic measurements.

One probable explanation of the non-uniform and low deposition efficiency lies in the surface morphology of the copper substrate.

Generally, metal electrodeposition reaction takes place in two consecutive and coupled stages. It first starts with the formation of thermodynamically stable crystal nuclei at some active sites of the cathode, followed by their growth. Both processes can be expressed in terms of characteristic overvoltage, generally known as crystallization overvoltage, η_k. Note that the nucleation usually contributes more to the crystallization overvoltage than the growth. And the relation between the growth current *I* and the overpotential η is expressed by the Butler- Volmer formula [97];

$$I_{(t)} = AS_{(t)}Jo\{ \exp[\alpha zF\eta/RT] - \exp[-(1-\alpha)zF\eta/RT] \} \qquad (5.3)$$

Jo is the exchange current density, the cathodic and anodic charge transfer coefficients are α and 1-α, respectively. R is the molar gas constant and T is the temperature. F is the Faraday constant, z is the number of electrons transferred and $S_{(t)}$ characterizes the type of reaction control taking place during the process.

During cathodic polarization, the contribution in current of the anodic term is negligible.

Equation 5.3 suggests that both the anodic and cathodic reactions are to be considered during the electrodeposition, unless the cathodic overvoltage is significantly high. In other words, the increase of the electrodeposition overvoltage should yield higher efficiency.

The understanding of the plating mechanism requires us to discuss about two important notions which define the electrocrystallization: the nucleation and the growth of crystals.
For a solid nucleus to form, it must reach a critical size that allows it to be thermodynamically stable. Otherwise, the nucleus is likely to contract in size and dissolve as a result. The growth is the result of the fusion of the crystal nuclei which have formed at the substrate surface.
The maximum energy for the formation of a nucleus is generally not constant all over the substrate surface. It varies as a function of sites or crystallographic defects. The different site types on metal surfaces are the point sites, the one-, two-, and three-dimensional sites. It is generally accepted that the activation energy to form a nucleus of critical size increases strongly as the dimension of the site increases [98].
Under comparable conditions, the rate of nucleation that is the number N_k of nuclei forming in unit time decreases when ΔG^* increases as described by Equation 5.4. The critical nucleus size r* can be related to the crystallization overvoltage η_k, as given by Equation 5.5 [97].

$$dN_k/dt = a_k exp(-\Delta G^*/RT) \qquad (5.4)$$

Here, a_k is a constant of the system.

$$\eta_k = 2\gamma V/zFr^* \qquad (5.5)$$

V is the molar volume of a crystal nucleus and γ is the surface energy between the crystal surface and the solution.
Eq.(5.4) and Eq.(5.5) suggest that high overpotential favors the nucleation by either reducing the critical size of crystal nucleus or by giving to the system sufficient energy to overcome the activation barrier set by the minimum energy of formation of nucleus. This might explain why at high overvoltages, the favored zinc nuclei quickly grow to form a layer that completely shields the underlying copper substrate, causing the hydrogen overpotential current to be dictated only by zinc, characterized by line A in Figure 5.5.

At low overpotential, the crystal growth may not occur at the sites with high activation energy for nucleation. Only those with a low activation barrier such as the zero or one-dimensional site types may allow thermodynamically stable nucleus to form. As a result, the surface of the copper substrate is only partially plated with the growing zinc crystallites. Consequently, during the cathodic polarization, a competition between the zinc deposition and the hydrogen evolution reaction on copper may occur. The competition is favored by the low hydrogen overpotential of copper. Therefore, the cathodic current is split out, causing the zinc deposition efficiency to decrease and the contribution of copper in the hydrogen overpotential current to be significant.

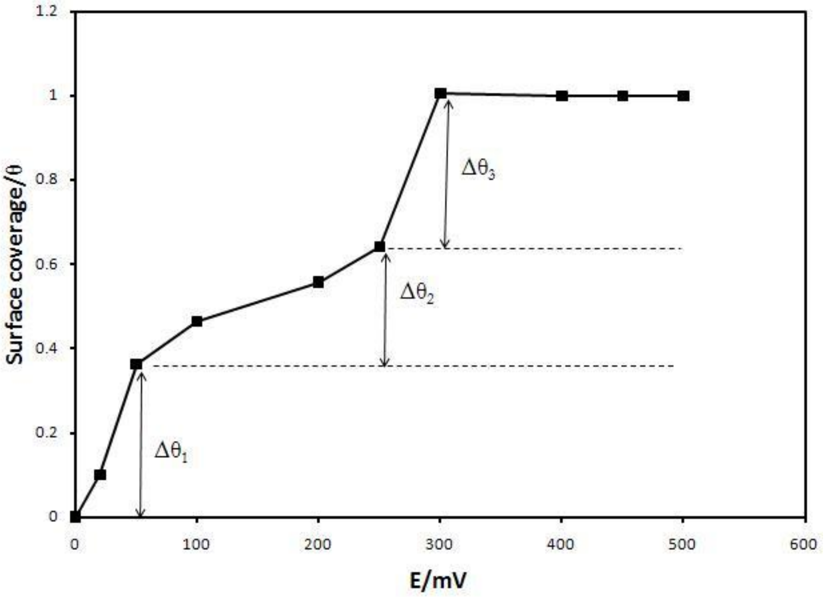

Figure 5.8: Zinc crystal surface coverage variation on a copper substrate as a function of the overpotential in 7M KOH solution containing 1.7wt.% of dissolved ZnO at 24°C.

Let us now assume that θ to be the surface coverage of the deposited zinc crystals. Then the surface coverage of the copper substrate is equal to 1-θ. The surface coverage is defined by the following equation:

$$\theta = \frac{A_z}{A} \tag{5.6}$$

Where A_z and A are the surface areas of the electroplated zinc and the substrate, respectively.

Considering the contribution of $i_{H2/Zn}$ and $i_{H2/Cu}$ (see Figure 5.5) and their respective surface coverage, the total hydrogen overpotential current and the zinc crystal surface coverage can be related as follows:

$$i = \theta i_{Zn} + (1-\theta) i_{Cu} \tag{5.7}$$

Or

$$\theta = (i - i_{Cu})/(i_{Zn} - i_{Cu})$$

Considering Equation 5.7, an experimental relation between the crystal surface coverage and the overpotential was established, as shown in Figure 5.8.

Up to 3 levels of surface coverage can be identified on the curve. The first level $\Delta\theta_1$ is characterized by a sharp increase from zero to about 27% of the surface coverage, as the cathodic polarization rises from the OCV up to 20mV.

$\Delta\theta_1$ probably represents the fraction of the substrate surface where the growth occurs on the active sites of lowest nucleation energy (zero dimensional type sites).

The second level $\Delta\theta_2$ represents 40% of the total surface and it exhibits a less steep slope that could indicate that the crystal growth is favored at sites of small numbers and different activation energies. $\Delta\theta_2$ may represent the surface fraction of the zinc crystals that nucleate and grow at one- and two-dimensional type sites. Its voltage window ranges from 20 to 250mV.

Beyond 250mV overpotential a complete surface coverage of copper is favored. We believe $\Delta\theta_3$ to characterize of the remaining active sites possessing the highest activation energy for nucleation. These sites could be mostly of three-dimensional types and they seem to represent about 35% of the surface.

5.4 Summary

The hydrogen evolution reaction during the eletrodeposition of zinc onto a copper substrate from alkaline zincate solution has been investigated using potentio-galvanostatic technique combined with EQCM. The results show that the hydrogen overpotential of copper is lower than that of zinc. We also observe that the electrodeposition efficiency is low at low overpotential due to the reaction competion between the hydrogen evolution and the zincates reduction on the copper substrate. Since the HER is mainly a surface reaction, it was possible to relate the hydrogen reduction rate to the surface coverage of the substrate. We were then able to study the deposition mechanism and explain the low electrodeposition efficiency measured by EQCM at low current densities. However, no direct correlation was established between the results yielded by both techniques; only their trends were analyzed. In general, electrodeposition is rather complex. Yet, it seems that mere technique such as potentio-galvanostatic could be used as a qualitative and quantitative surface characterization tool that helps investigate the isotherm of the crystal deposition onto a substrate.

Chapter6

Study of the stability and effect of indium coat on the zinc reaction

Abstract

In this chapter, the influence of the indium plating of the copper current collector on hydrogen gassing as well as cell performances was examined. The coating of the copper substrate with indium was found to significantly reduce the hydrogen gas evolution without causing appreciable increase in the cell internal impedance. The cycling tests indicated that the indium film is very stable within the potential window of operation of the zinc electrode. SEM analysis was carried out on the current collector cross section and the results are presented.

6.1 Introduction

Copper is the preferred current collector metal for zinc electrodes in alkaline solutions, mainly because it is rather cheap and it is a good electric conductor. On the other hand, copper has a relatively low hydrogen overpotential compared to zinc and its exhibits an open crystal structure that is susceptible to host incrusts or favor solid phase diffusion of foreign atoms. In batteries, when the copper collector is put in contact with zinc paste in presence of KOH solution containing zincates, hydrogen gas evolves as a result of the galvanic coupling formed by the two dissimilar metals. However, the gassing rate readily decreases upon the spontaneous deposition of a zinc film that generally takes place on the surface of the copper substrate and serves as a protective layer. However, the layer stability is rather poor and seems to depend on the system hydrodynamic conditions, KOH concentration and state of discharge. For instance, in rechargeable cells using copper as the current collector for the zinc anode, subsequent discharges may cause the protective zinc film to deplete locally, resulting in an enhancement of gas evolution reaction. It is therefore recommended to protect the copper with more stable coatings. Some studies [99] have shown that the plating of copper with metal such as indium or tin is efficient to reduce gassing. Especially that, some works [100, 101] claimed that indium metal oxidizes in alkaline solution to produce a film of In_2O_3 or $In(OH)_3$. The studies carried out by Campbell showed that the overvoltage to hydrogen evolution of indium is fairly high [102].

In this work, the stability and beneficial impact of indium plating on the HER in rechargeable zinc-air cell were explored.

6.2 Experimental

6.2.1 Preparation of the porous zinc paste and electrode

Zinc powder (alloyed with 300ppm bismuth and 300ppm indium, Grillo) of size ranging from 30 to 200µm was mixed with 1wt% Teflon PTFE (6C-N, DuPont) and1wt% Carbopol C940. A porous paste was obtained by adding 7M KOH solution to the mix. 1g of the paste was then pressed onto a copper woven mesh and rolled to form the porous zinc electrode. The mesh had a surface area of 3cm^2 and was cleaned in low concentrated acidic solution and thoroughly rinsed with triple deionized water prior to its use. The KOH solution was prepared by dissolving reagent-grade KOH pellets in deionized water.

6.2.2 Gas volumetric measurement in vessel

The corrosion test was carried out by measuring the volume of the evolved hydrogen gas of zinc paste and zinc electrode submerged in a measuring Pyrex vessel containing 50ml of 7M KOH solution. The vessels were aged in an oven at 70°C for several days and the amount of hydrogen was recorded on a daily basis. The measurement was performed at room temperature after the cells were cooled down.

6.2.3 Investigation of gassing in rechargeable zinc-air cell

The investigation was carried out by performing a storage test on 675 button cells at elevated temperature. To this respect, two lots of 3 cells each were prepared. The cells were assembled like described in section (3.1.1). In one of the lots, the inner surface of the anode cup was plated with indium. The plating was made in an electrolytic sulfamate bath in which a shiny and smooth coat was obtained, as illustrated in Figure 6.1. The storage test was performed on fresh and cycled cells. The cells were tab-sealed and stored in an oven at 70°C and 50% relative humidity. The life time of each cell was recorded. The end of life was reached when the cells wept.

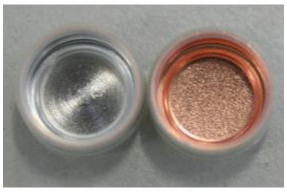

Figure 6.1: Bare anode cup (right) and indium-plated anode cup (left).

6.2.4 Qualitative and semi-qualitative analysis

The cross section of fresh and cycled anode cups was examined using a Vega Tescan SEM-EDS. A light microscope from Leica DM6000 Series was used to analyze the state of the cup surface.

6.2.5 Measurement of the electrochemical performances

a. Cyclic voltammetry

The three-electrode electrochemical cell described in section 3.1.2 was used to perform cyclic voltammetry experiments on Indium and zinc. For CV on indium, the WE and CE both consisted of indium plate (99.99% pure, Indium Corporation of America). Copper and zinc were used as the WE and CE, respectively, for the CV on Zn. The experiments were performed at room temperature using a Solartron 1470E cell test system.

b. Cycling test

Cycling tests were carried out in 675 button cells at constant discharge and charge current of 10mA. The cells had a nominal capacity of 300mAh and were cycled at 50% depth of discharge. The discharge and charge cutoff voltages were set at 0.9V and 1.95V, respectively. For some specific experiments, the charge cut-off voltage was increased up to 2.25V because the cells used different separator package. The cells were initially subject to a cycle formation performed at low rate. The cells were cycled using a computer–controlled tester from Arbin.

6.3 Result and Discussion

6.3.1 Corrosion test

As illustrated in Figure 6.2, the electrode made with the mesh coated with indium exhibits lower gassing rate than the zinc electrode made with a bare copper mesh. The former shows a cumulative gravimetric gassing of 9ml after 800 hrs storage at 70°C whereas the latter exhibits the same cumulative gas volume at a much earlier stage (after 120hrs). The results indicate that indium plating tremendously reduces the corrosion rate.

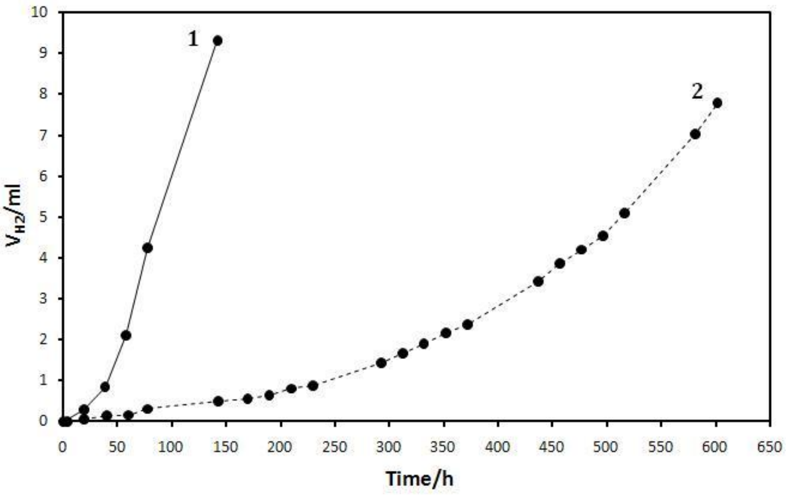

Figure 6.2: Corrosion of zinc paste rolled within a copper mesh without (1) and with (2) an indium coat in 7M KOH solution.

The accelerated life test was performed with fresh and cycled button cells (10 cycles) assembled in bare and indium-plated anode cup. The results are presented in Table 6.1. Generally gassing gives rise to a pressure buildup inside the cells, causing them to bulge and eventually to leak either through the air electrode and its surrounding or around the crimped seal. This experiment shows that the rate of HER is lower with the indium-plated anode cup as a life extension of 6 to 10 days is obtained in comparison to the cell build with the bare cup. The data also indicate that cycling significantly enhances gassing. However, the rate seems to be tremendously lowered with indium.

Cells	***Aging @ 70°C, 50%RH (days)***	
	Bare cup	Indium plated cup
Fresh cell-1	21	31
Fresh cell-2	23	29
Cycled cell-1	3	17
Cycled cell-2	7	14

Table 6.1: Life time of the fresh and cycled button cells under the conditions of 70°C and 50%RH.

6.3.2 Cyclic voltammetry

Figure 6.3 shows the cyclic voltammetric polarization curve of indium in 7M KOH solution saturated with indates, between 0 to 0.95V vs. Zn reference electrode and at a scan rate of 100mVs^{-1}. Four peaks are exhibited: the first anodic peak A1 at 0.325V, the second anodic peak A2 at 0.35V and the third anodic peak A3 at 0.325V followed by the cathodic peak C at 0.275V. Saidman and El Sayed [103, 104] studied the dissolution and deposition of indium in alkaline solution. They attributed the first anodic peak A_1 to the dissolution of indium with the formation of indate (InO_2^-) ions whose saturation at the electrode surface gives rise to a porous layer of $In(OH)_3$. They confirmed the presence of In_2O_3 at the second anodic peak A_2. The formation of $In(OH)_3$ proceed through consecutive one-charge processes [105, 106]:

$$\mathrm{In} + \mathrm{OH}^- = \mathrm{In(OH)_{ads}} + \mathrm{e}^- \tag{6.1}$$

$$\mathrm{In(OH)_{ads}} + \mathrm{OH}^- = \mathrm{In(OH)_{2ads}} + \mathrm{e}^- \tag{6.2}$$

$$\mathrm{In(OH)_{2ads}} + \mathrm{OH}^- = \mathrm{In(OH)_3} + \mathrm{e}^- \tag{6.3}$$

The formation of the In_2O_3 layer may result from the direct oxidation of the metal at higher potential according to the reaction:

$$2\mathrm{In} + 6\mathrm{OH}^- = \mathrm{In_2O_3} + 3\mathrm{H_2O} + 6\mathrm{e}^- \tag{6.4}$$

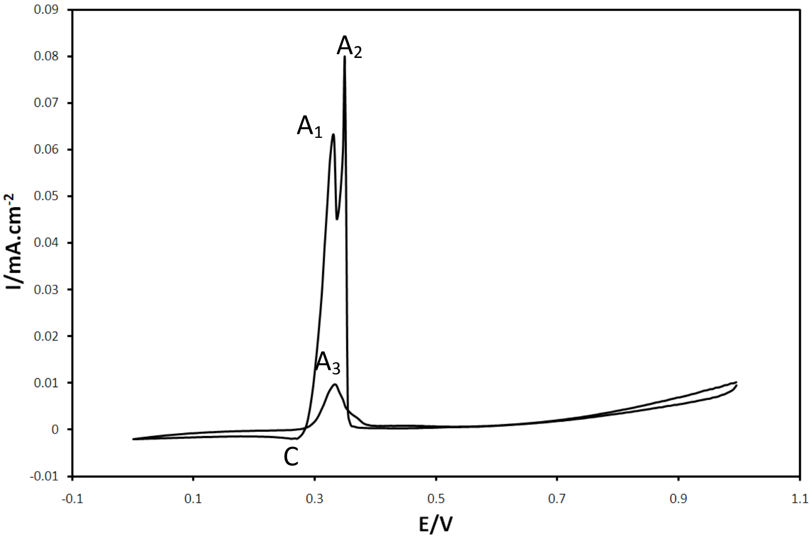

Figure 6.3: Cyclic voltammogram of indium in 7M KOH; scan rate = 100mVs^{-1}; between 0 and 950mV vs. Zn RE.

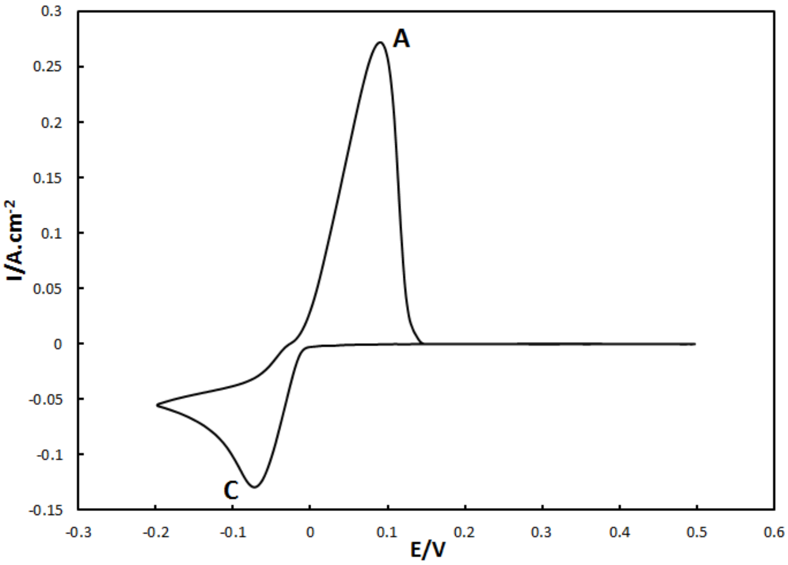

Figure 6.4: Cyclic voltammogram of ZnO in 7M KOH; scan rate = 100mVs^{-1}; between -200 and 500mV vs. Zn RE.

The reverse scan in the anodic region exhibits a peak A_3 near the potential of the peak A_1 and A_2, suggesting that the adhered $In(OH)_3$ and In_2O_3 film formed during the anodic scan are not stable. As the potential shifts more negatively in the cathodic region a small cathodic peak C is revealed. The charge under the cathodic peak C is insignificant compared to that under the anodic peaks A_1 and A_2. This indicates that indates are barely reduced under these conditions.

For comparison, the cyclic voltammogram of zinc oxide is shown in Figure 6.4 where two peaks are revealed. The CV was performed between -0.2V to 0.5V vs. Zn reference electrode at a scan rate of 100mVs^{-1} in 7M KOH solution containing 1.7wt.% of dissolved ZnO. The occurrence of the anodic peak A at 0.085V is ascribed to the dissolution of zinc whereas that of the cathodic peak C characterizing the reduction of zincates ions to metallic zinc is attributed to either the diffusion limitation of $Zn(OH)_4^-$ ions towards the surface or that of OH^- ions away from the reaction sites. The cathodic peak appears at a potential of -0.075V during the reversal scan in the cathodic region. The difference in charge between the dissolution and reduction reactions indicates that, quantitatively, not all the discharge products of zinc are reduced.

The CVs suggest that zinc is more active in 7M KOH solution than indium with regard to their respective peak currents. It is also shown that the dissolution potential of zinc is lower than the deposition potential of indium, suggesting that an indium film must remain stable within the potential window of operation of rechargeable zinc electrode in 7M KOH solutions. This is another reason why indium is a preferred material for coating the collector besides its high hydrogen overpotential.

6.3.3 Electrochemical performance

Button cells from each lot were discharged and charged at a constant drain rate of 10 mA (15mA.cm^{-2}) for 15 hrs. The typical charge voltage profile as a function of time is shown in Figure 6.5. The analysis of the charge curves during the first cycle Figure 6.5 (a) shows that the behavior of the cells consisting of the indium-plated and bare anode cups is comparable. The two voltages exhibit a slight decay varying from 10 to 15 mV at the beginning of the charge to reach a constant value after 6hrs at about 1.93V. Such decay may be explained by the increase of the electronic conductivity and porosity of the paste as ZnO which is not very conductive transforms into zinc, a material of higher density.

At the 3rd cycle Figure 6.5 (b), the voltage of the bare cell increases right from the start of the charge, reaching the cutoff voltage of 1.96V after 10.5 hrs. The indium-plated cell shows an initial behavior that is similar to that observed during the 1st cycle, followed by a sloppy rise toward the end of charge.

The trends of the charge voltage curves at the 5thcycle Figure 6.5 (c) are comparable to those at the 3rd cycle. However, the cell with the bare anode cup reaches the cutoff voltage in a shorter period of time (9hrs) while the rising end of the In-plated cell voltage curve slightly flattens out.

The shift in the charge voltage between the 1st and 5th cycle exhibited by the cell with the bare anode cup may be attributed to the hydrogen gas formed inside the cell. If not vented out, the hydrogen gas may accumulate at the interface to form a resistance pouch that causes the cell internal impedance to increase.

The charge and discharge voltage variations as function of time of the cell with the bare cup and the indium-plated cup are illustrated in Figure 6.6 and Figure 6.7, respectively. The In-plated cell exhibits 22 cycles whereas the bare cell reaches only 11 cycles before hitting the charge cut-off voltage of 2.25V. The data indicate that the life time of cells improves when the anode cup is indium plated.

The effect of the indium film on the power performance of the cells was examined as well, by steady state discharge polarization. The cells were discharged at various potentials ranging from 1.4 to 1.1V until attainment of a steady current. The steady state polarization curves of the fresh cells made with a bare and In-plated anode cup are compared in Figure 6.8. The indium film does not seem to influence the cell internal impedance since the two curves are comparable.

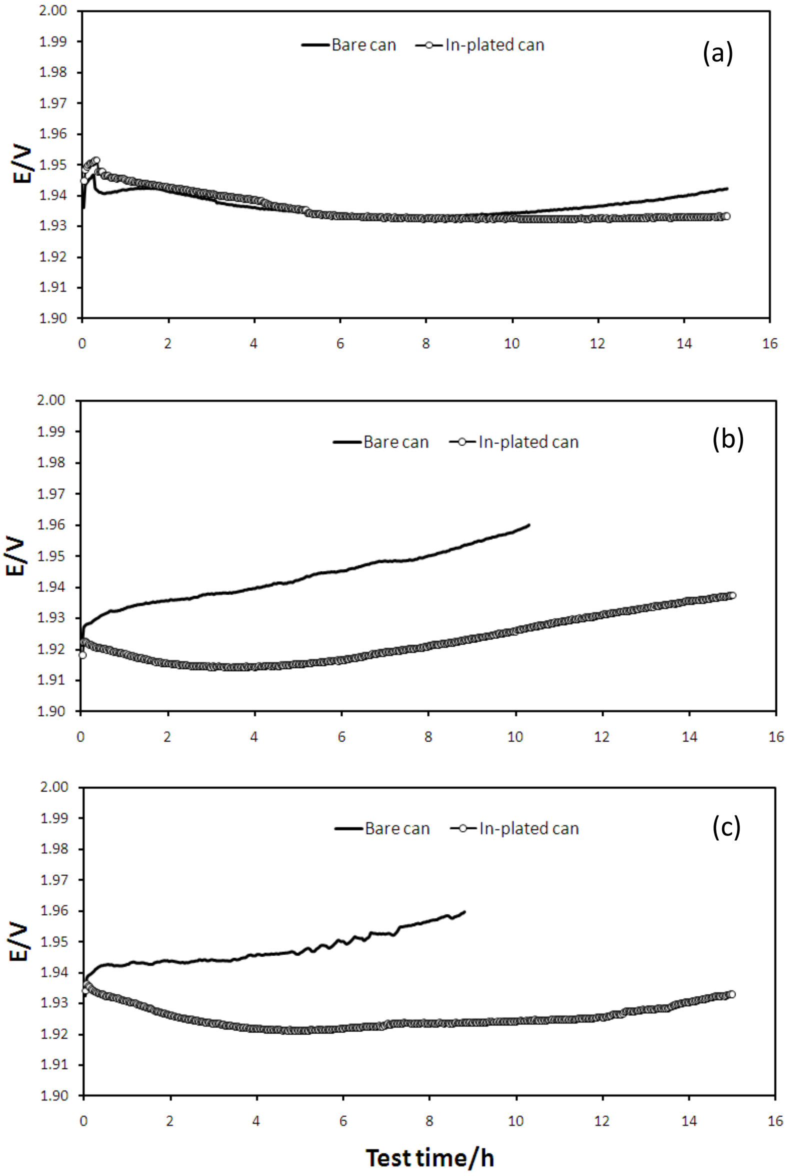

Figure 6.5: Charge voltage variation with time and cycle number of rechargeable button cell comprising a bare copper cup and indium plated cup for the anode: (a) after 1 cycle, (b) after 3 cycles and (c) after 5 cycles.

Note that beyond the current density of 10mA.cm^{-2}, the cells may be subject to the diffusion limiting current on the air electrode, accounting for non-linearity of the curve in that region.

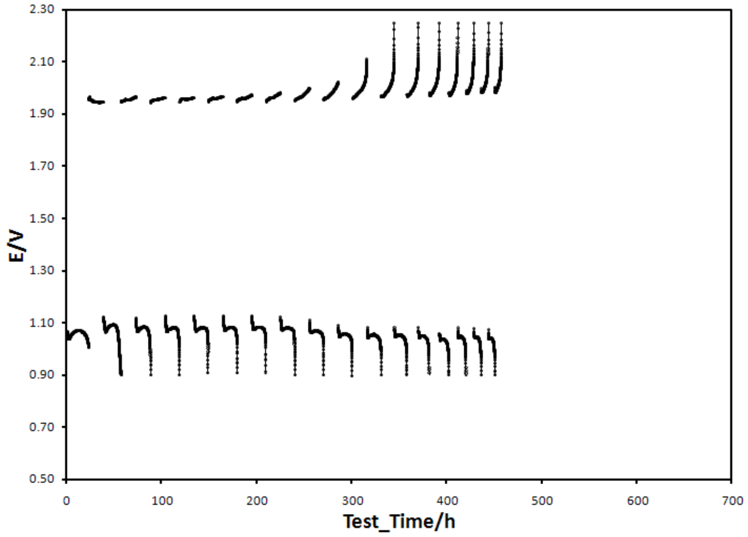

Figure 496: Discharge and charge voltage variation as a function of time at 15mA/cm^2 of button cell with the bare anode cup.

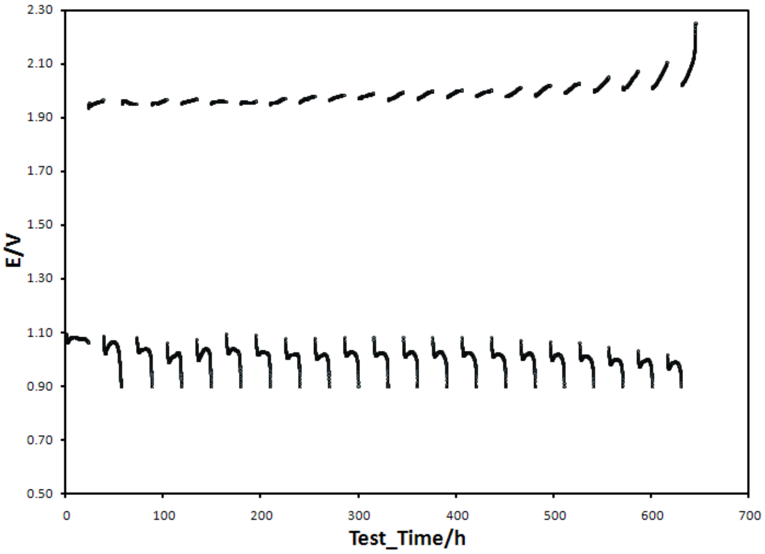

Figure 6.7: Discharge and charge voltage variation as a function of time at 15mA/cm^2 of button cell with indium-plated anode cup.

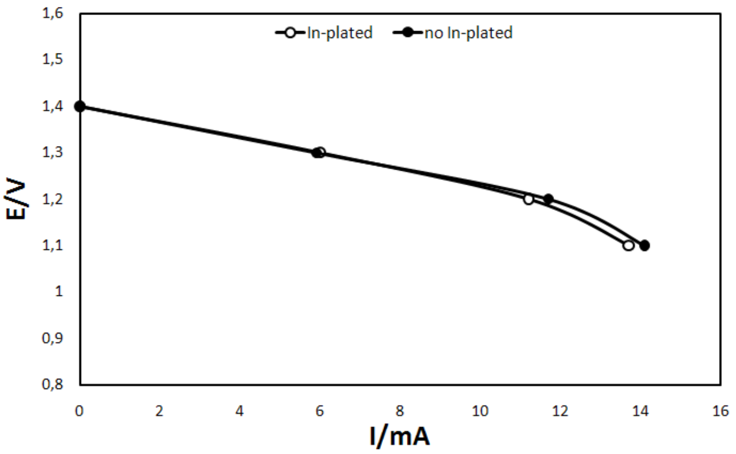

Figure 50.8: Steady state polarization curve of zinc-air 675 button cell: (o) with indium plated anode cup; (●) with bare anode cup**.**

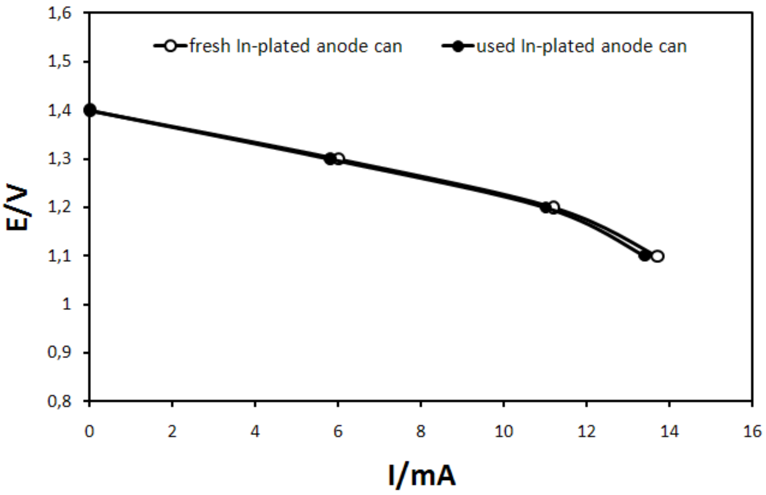

Figure 6.9: Steady state polarization curve of zinc-air 675 button cell with indium plated anode cup: (o) fresh anode cup; (●) cycled anode cup.

In order to investigate the impact of cycling on the electrical resistance of the indium film, an In-plated anode cup retrieved from an old cell that cycled 15 times was cleaned up and used to assemble a fresh cell. The cleaning was performed by rinsing the can several times with deionized water after scooping out the old zinc paste. Steady state polarization test similar to the one described above was performed on the cell and the result was compared with that of a cell made with a fresh In-plated anode can. As illustrated in Figure 6.9, the two cells show similar polarization performances. This suggests that cycling may not alter the indium the indium coat.

6.3.4 Surface analysis

The analysis of the anode cup surface was performed using a light microscope. The cells were cycled 10 times prior to the analysis. As illustrated in Figure 6.10 (A) and (B) the surface of the bare anode cup exhibits several depletion zones where copper is exposed. Initially, the copper surface is spontaneously plated with zinc, when the zinc paste is loaded in the cup, as explained in section 2.1.3. The protecting zinc film is very instable as it can easily oxidize or dissolve. This leads to the exposure of copper and the enhancement of gassing as a result. No copper exposure was observed in the cup plated with indium, indicating that In-plated cells are less prone to gas (see Figure 6.10 (C) and (D)). This is consistent with the result of the charge voltage analysis.

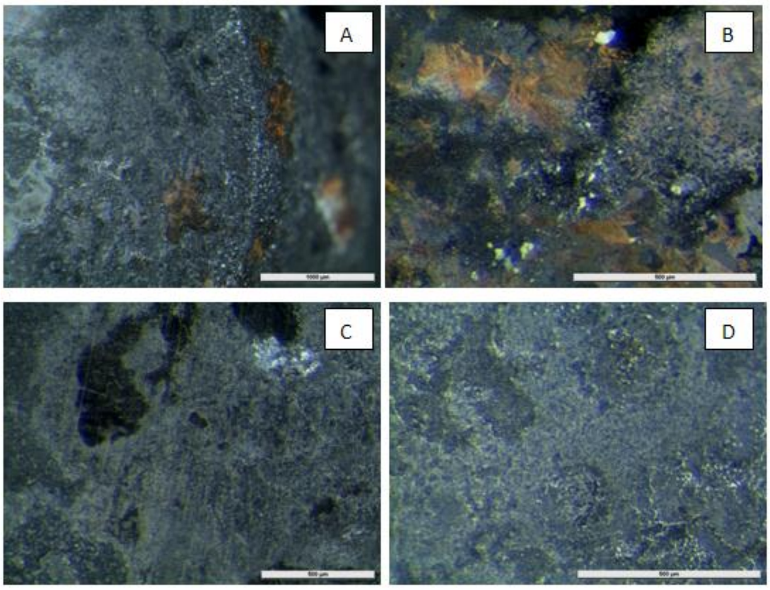

Figure 6.10: Surface morphology of anode cup of zinc-air 675 button cell cycled 10 times: (A-B) with bare anode cup; (B) with indium-plated anode cup.

The SEM images of the cross section of fresh and cycled In-plated anode cup are shown in Figure 6.11 and Figure 6.12, respectively. The indium plating provided a complete coverage and a thin film deposition of about 0.8µm. The analysis of the cell that cycled 20 times revealed the presence of deposited zinc onto and in the structure of the indium film, causing its thickness to drop by 75% to 80%.

The presence of zinc in the indium protective film structure, as evidence by the EDS analysis (Figure 6.12), probably results from a gradual oxidation of indium due to repeated cycles.

Indium may oxidize to form a porous layer, allowing zincates to diffuse in and the zinc crystals to grow during the charge, as a result.

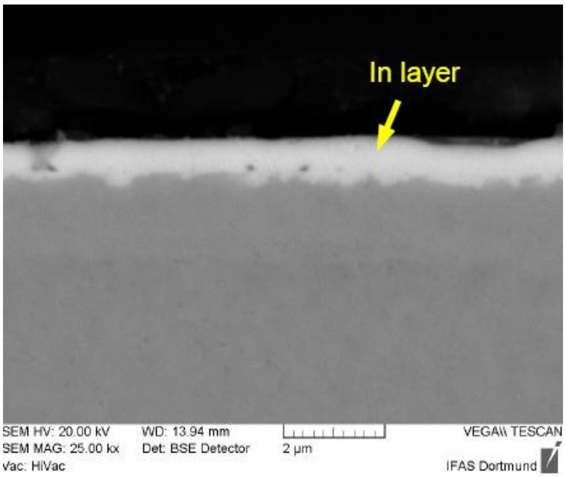

Figure 6.11: SEM image of the cross-section of freshly indium-plated anode cup of zinc-air 675 button cell.

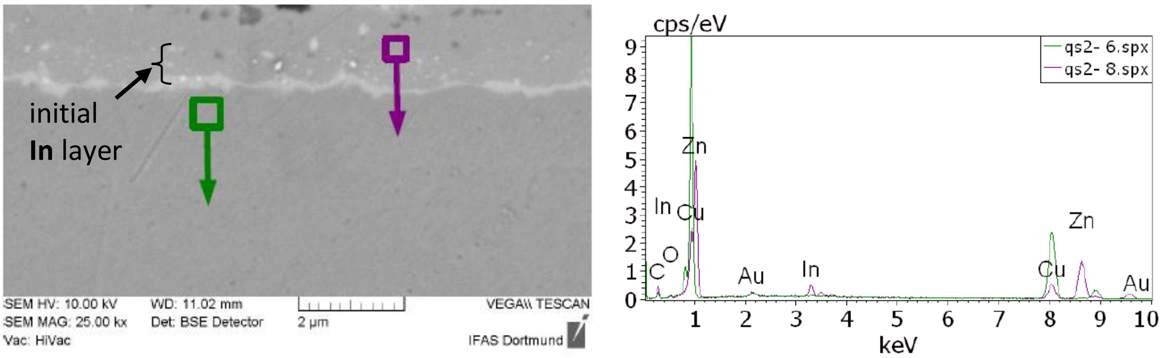

Figure 6.12: SEM image (left) and EDS analysis (right) of the cross-section of cycled zinc air 675 button cell with indium-plated anode cup.

6.4 Summary

Due to the high hydrogen overpotential of indium, the plating of a copper substrate with indium significantly reduces the gassing resulting from the galvanic coupling effect between zinc and copper. The results showed that the zinc layer that spontaneously forms onto the copper surface when zinc paste is loaded into the anode cup can be depleted upon subsequent cycles. An indium film offers a more resistant coat. However, SEM-EDS analysis suggests that prolonged cycles eventually alter the film structure, causing its thickness to decrease. This points out to the necessity to optimize the thickness of the deposited indium film. Note that because indium is a rather expensive material, the thinner the film, the better from a production cost point of view. It was also found that the deposited indium film does not influence the reaction kinetics of zinc and tremendously improves the cycle life of rechargeable button cells.

Chapter 7

$In(OH)_3$ effect on zinc reaction in concentrated KOH solution

Abstract

In the present work, the effect of $In(OH)_3$ inhibitor on the reaction kinetics of zinc oxidation and reduction was investigated. Cyclic voltammograms and electrochemical impedance spectra of zinc electrodes in deaerated zincate-containing KOH solutions with or without $In(OH)_3$ were studied. The electrolyte viscosity change was measured using a quartz crystal microbalance. The data indicate that the presence of $In(OH)_3$ salt in KOH solution improves the kinetics of the anodic as well as the cathodic reaction of zinc. These effects are concentration-dependent and are attributed to the surface modification of the current collector due to the deposition of indium crystallites.

7.1 Introduction

Multiple approaches have been studied to suppress gassing in batteries and still the problem remains elusive. Upon the ban of Mercury due to its toxicity, many studies have reported the use of various organic and inorganic additives to the electrolyte to suppress gassing [26-30]. Although the inhibiting properties of these compounds have been heavily studied, their impact on the overall reaction kinetics is sometimes elusive, especially in rechargeable systems. An illustrative case is $In(OH)_3$ which has long been known and used in alkaline batteries for its inhibiting properties with respect to hydrogen evolution on zinc [107].

The objective of the present work was to study the effects of $In(OH)_3$ salt on the dissolution and deposition reaction kinetics of zinc, within the framework of potential use in secondary cells.

7.2 Experimental

7.2.1 Corrosion test

a. Preparation of the porous zinc paste and electrode

Zinc powder (alloyed with 300ppm Bismuth and 300ppm indium, Grillo) of size ranging from 30 to 100µm was mixed with 1wt% Teflon PTFE (6C-N, DuPont) and1wt% Carbopol C940. A porous paste was obtained by adding 7M KOH solution to the mix. 1g of the paste was then pressed onto a pure copper woven mesh with a surface area of $3cm^2$ to form the porous zinc electrode. The mesh was cleaned in low concentrated acidic solution and thoroughly rinsed with triple deionized water prior to its use. The KOH solution was prepared by dissolving reagent-grade KOH pellets in deionized water.

b. Gas volumetric measurement

The corrosion testing was carried out by measuring the volume of the evolved hydrogen gas that generally accompanies the dissolution of zinc in alkaline solution. In that regard, the porous zinc paste solely and the zinc electrode described above were each submerged in a measuring Pyrex vessel containing 50ml of 7M KOH solution. The measurements were carried out using plain 7M KOH solution and using the same solution containing $In(OH)_3$

additive in various concentrations ranging from 0.6x10^{-3}M to 3x10^{-3}M. The vessels were aged in an oven at 70°C for several days and the amount of hydrogen was measured on a daily basis by recording the volume of the accumulated gas in the vessel.

7.2.2 Cyclic voltammetry

The experiment consisted with depositing a film of zinc onto a copper substrate by reducing the zincates in solution during the cathodic sweep. The anodic sweep was characterized by the dissolution of the formed zinc film. A three-electrode electrochemical cell similar to that described in section 3.1.2 was used to perform the experiment. Copper was used as the working electrode in 7M KOH solution containing 1.7wt.% of dissolved ZnO. The solution inside the cell was de-aerated by passing oxygen-free nitrogen through it. The experiments were performed at room temperature with various concentrations of $In(OH)_3$ additives in solution using a Solartron 1470E cell test system. $In(OH)_3$ was added to the experimental solution in concentrations varying from 0.6x10^{-3}M to 3x10^{-3}M.

7.2.3 AC. Impedance technique

The impedance measurements were performed using a Solartron analytical 1400 analyzer over a frequency range from 0.1Hz to 1MHz. The cell assembly used was the same as in the cyclic voltammetry experiments. The AC signal amplitude was 10mA and the impedances were measured at a constant cathodic current of 20mA. The Nyquist plots were interpreted by applying the Randles equivalent circuit.

7.3 Result and Discussion

7.3.1 Zinc corrosion

The Indium effect was investigated by dissolving $In(OH)_3$ in the 7M KOH solution in concentrations varying from 0.6x10^{-3}M to 3.0x10^{-3}M. It was found that the hydrogen gassing rate of the zinc electrode can be substantially reduced in presence of indates, as illustrated in Figure 7.1. The data show that the gas inhibiting effect increases with the indate concentration up to an optimal value between 2.4x10^{-3}M and 3.0x10^{-3}M. This behavior is depicted in Fig 3 where the hydrogen gas volume variation is plotted as a function of the $In(OH)_3$ concentration after 148hrs of storage at 70°C.

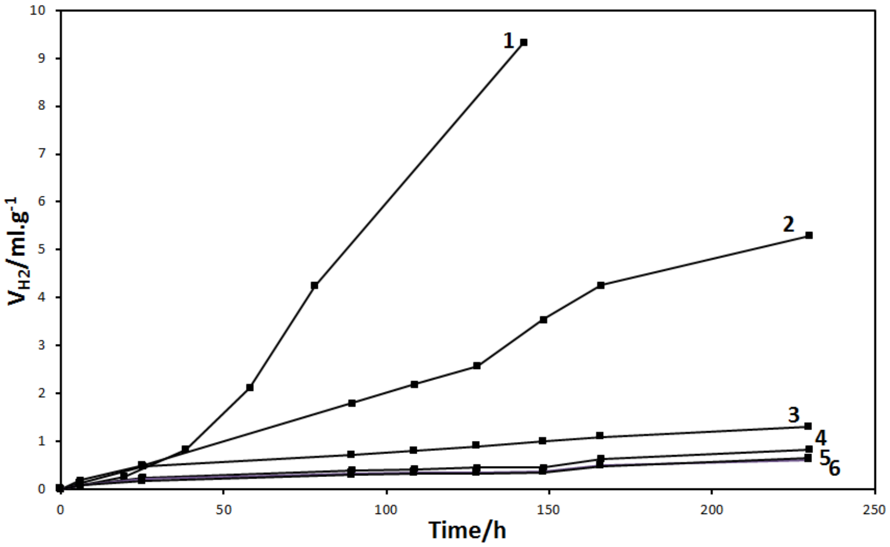

Figure 51: Dependence of zinc electrode hydrogen evolution rate with time in 7M KOH with and without indate additives. Index: Plain 7M KOH (1), plain + 0.6x10^{-3} M (2), plain + 1.2x10^{-3} M (3), plain + 1.8x10^{-3} M (4), plain + 2.4x10^{-3} M (5), plain + 3.0x10^{-3} M (6); at 70°C and 50%RH.

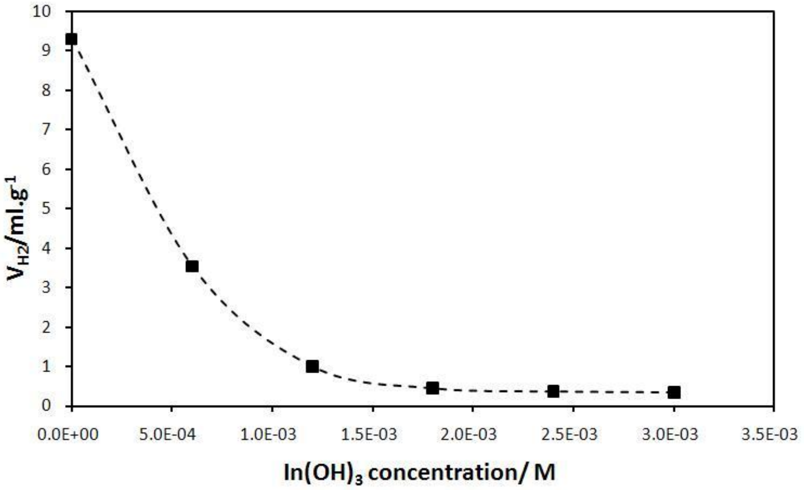

Figure 52: Variation of the zinc electrode hydrogen evolution rate with indate concentration after 180 hours of storage at 70°C and 50%RH.

The trend observed in Figure 7.2 may be dictated by the solubility of $In(OH)_3$ in the solution where the optimal concentration would correspond to the solubility limit. Such an interpretation is in agreement with the study carried out by Deichman et al. who found that the solubility of $In(OH)_3$ in concentrated NaOH solutions does not exceed $2.0x10^{-3}$M [108].

7.3.3. Cyclic voltammetry

The effect of indates on the redox reaction of zinc in 7M KOH containing 1.7wt% ZnO was investigated. The cyclic voltammograms in the presence of $In(OH)_3$ additives are shown in Figure 7.3. Compared with the plain electrolyte, the presence of $In(OH)_3$ in the solution shifts the anodic peak toward the cathodic direction and the cathodic peak toward the anodic direction. In other words, the peak potential difference ΔEp decreases, indicating that indates increases the kinetic activity of the dissolution and the deposition reaction of zinc. However, this effect seems to reach a limit where further increase in indate concentrations leaves the system invariant, as shown in Figure 7.4. The optimal indate concentration seems to vary between $1.8x10^{-3}$ and $2.5x10^{-3}$M. The observed trend could be dictated by the solubility of $In(OH)_3$ in the solution where the optimal concentration would correspond to the solubility limit. The results are concordant with the gassing test experiment.

The dependency of the anodic and cathodic peak currents on the indate concentration was also analyzed and is represented in Figure 7.5 and Figure 7.6, respectively. It can be seen that the current density of the anodic peak increases from 141 to $148mA/cm^{-2}$, whereas that of the cathodic peak varies from 47 to $57mA/cm^{-2}$. The trend exhibited by the curves of the current peak variation as a function of the indate concentration is similar to that of the voltage peaks which is characterized by an increase up to an optimal concentration limit.

The contribution of the indates to the cathodic current was examined and was found to be negligible as no indate reduction peak was observed in CV performed in zincate-free 7M KOH solution containing $3.0x10^{-3}$M $In(OH)_3$, as illustrated by Figure 7.7. The CV test procedure and the cell used were identical to those described in the experimental section, except the zinc counter electrode that was replaced with indium. In Figure 7.7, the exhibited peak currents result from the hydrogen overpotential reaction. The data suggest that the hydrogen overpotential of copper increase in presence of indates.

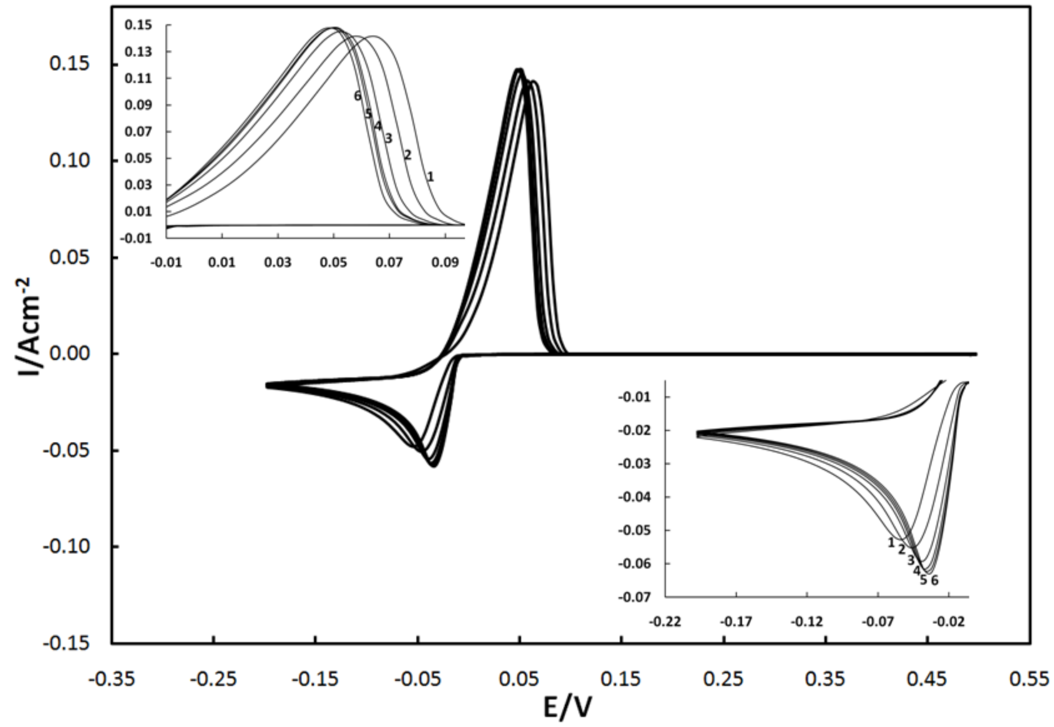

Figure 53: Cyclic voltammogram of ZnO in 7M KOH with and without indate additives. Index: Plain 7M KOH (1), plain + 0.6x10^{-3} M (2), plain + 1.2x10^{-3} M (3), plain + 1.8x10^{-3} M (4), plain + 2.4x10^{-3} M (5), plain + 3.0x10^{-3} M (6); scan rate = 10mVs^{-1}; between -200 and 500mV vs. Zn RE at 25°C.

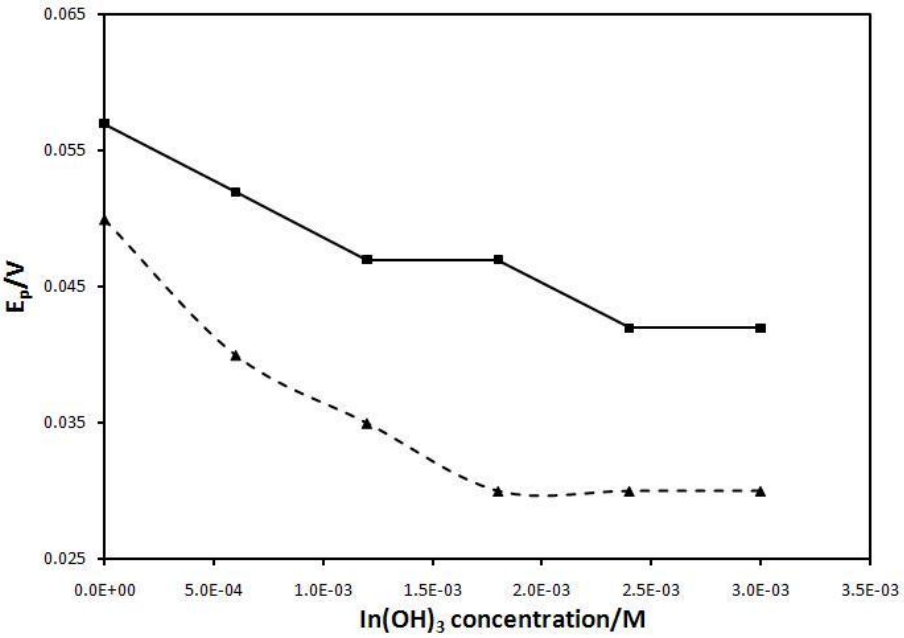

Figure 54: Effect of the indate concentration on the anodic (——) and cathodic (-----) potential peaks of the cyclic voltammogram for ZnO in 7M KOH at 25°C.

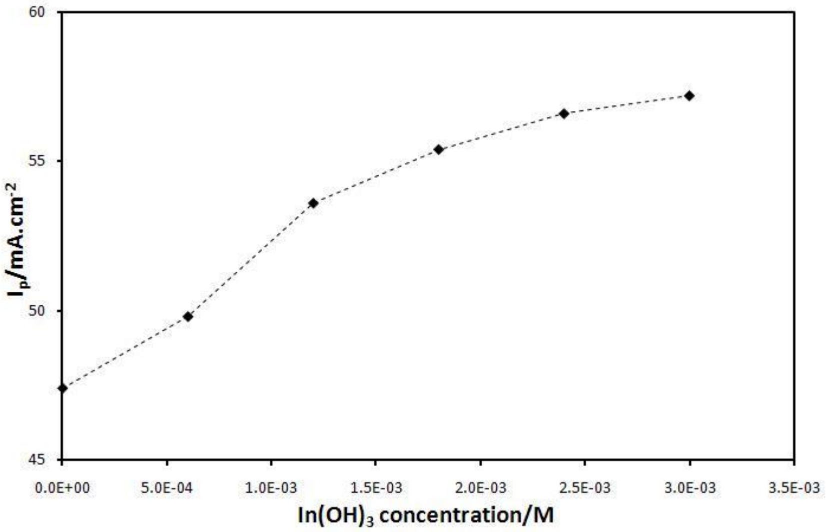

Figure 55: Effect of the indate concentration on the anodic peak current of the cyclic voltammogram of ZnO in 7M KOH at 25°C.

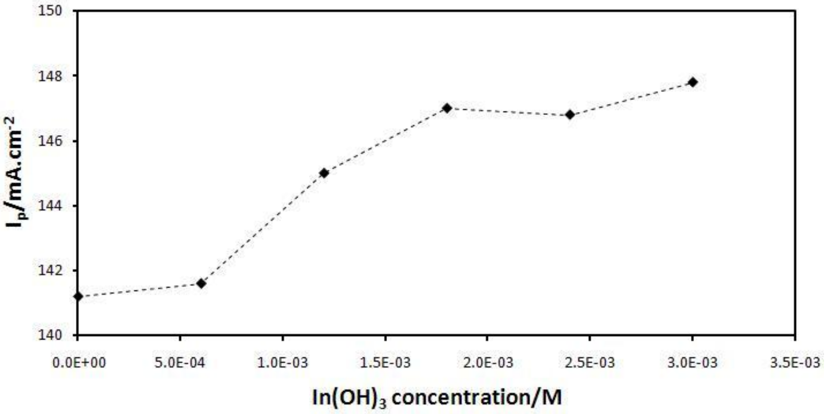

Figure 56: Effect of the indate concentration on the cathodic peak current of the cyclic voltammogram of ZnO in 7M KOH at 25°C.

Experiments were carried out to investigate the influence of the scan rate on zinc dissolution and deposition in presence and absence of $In(OH)_3$. The variation of the anodic and cathodic peak currents with the square root of the sweep rate was studied.

Figure 7.8 (a) and (b) shows typical voltammogram for various scan rates (from 10 to 100mV/sec) of ZnO in 7M KOH electrolyte and in the same electrolyte containing 3.10^{-3} M $In(OH)_3$, respectively.

The total peak current can be represented as the sum of the charge-transfer and diffusion controlled currents [109]:

$$i_p = k_{ct}\nu + k_{diff}\nu^{1/2} \quad (7.1)$$

where k_{ct} and k_{diff} are the constants corresponding to the charge-transfer and diffusion-controlled currents, respectively. As shown in Figure 7.9, the two systems show a linear relation between the peak current and the square root of the sweep rate for the dissolution and deposition reactions, suggesting that the zinc oxidation and reduction reactions are mainly diffusion-controlled processes. Table 7.1 summarizes the values of k_{ct} and k_{diff} in the respective electrolytes. It was found that indates influence the charge transfer mechanism of the zinc redox reaction and more particularly that of the electrodeposition where k_{ct} exhibits an increase from 0.28 to 0.58. Such a variation of the charge transfer rate of the zinc deposition reaction is probably due to the surface modification of the copper collector resulting from the deposition of some indium crystallites. Indates may be reduced upon the cathodic polarization according to the reactions [110]:

$$In(OH)_3(s) + OH^- \rightarrow H_2InO_3^- + H_2O \quad (7.2)$$

$$H_2InO_3^- + H_2O + 3e- \rightarrow In + 4OH^- \quad (7.3)$$

The surface modification of the copper collector by indium seems not to influence the zinc dissolution reaction as only an insignificant change of the charge transfer constant from 2.81 to 2.86 was recorded. The data also reveal that the diffusion constant k_{diff} of the cathodic sweep increases from 0.51 to 0.64 whereas that of the anodic sweep varies from 1.65 to 1.74 in presence of $3.0\text{x}10^{-3}$M $In(OH)_3$.

The significant rise of the electrodeposition charge transfer rate could be attributed to the increase of the effective current for the zincate reduction since the undesired hydrogen overpotential current is reduced in presence of indates, as illustrated in Figure 7.7. The curves show that at a cathodic potential of 200mV, the current density of the hydrogen overpotential is reduced from 0.07 to 0.04 A/cm^2 in presence of $3.0\text{x}10^{-3}$M $In(OH)_3$.

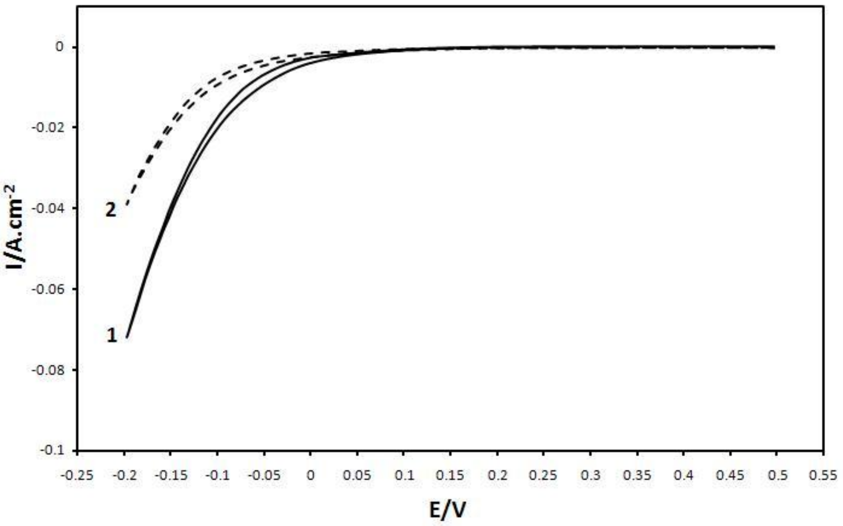

Figure 57: Cyclic voltammogram in 7M KOH with and without indate additives. Index: Plain 7M KOH (1), plain + $3.0\text{x}10^{-3}$ M (2); scan rate = 10mVs^{-1}; between -200 and 500mV vs. Zn RE

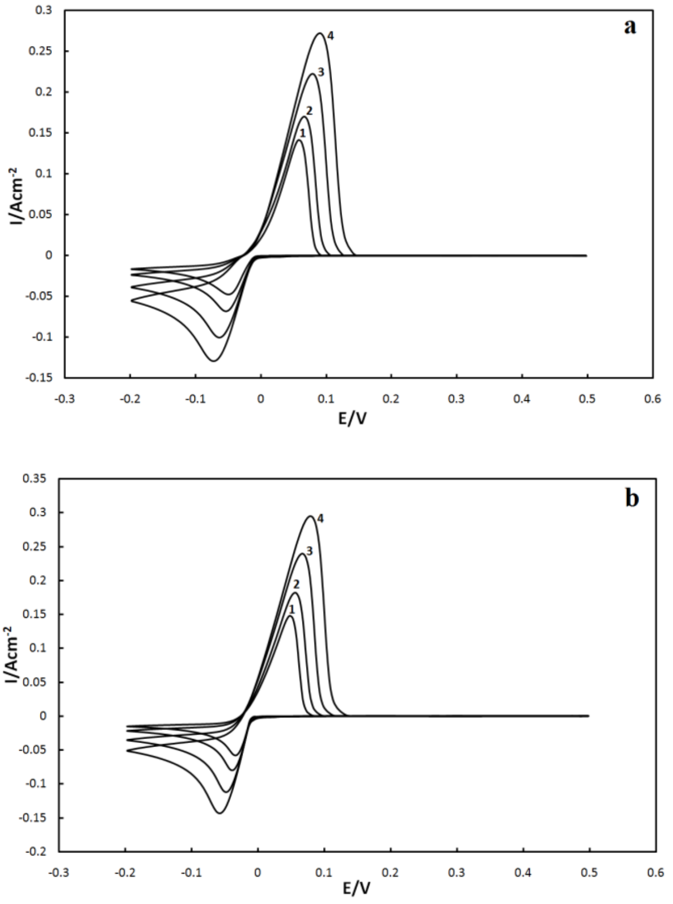

Figure 58: Cyclic voltammogram of ZnO at various scan rates; between -200 and 500mV Vs Zn RE at 25°C. Index: (1)10mVs^{-1}, (2) 20mVs^{-1}, (3) 50mVs^{-1}, (4) 100mVs^{-1}; (a) in 7M KOH and (b) in 7M KOH + 3.10^{-3} M $In(OH)_3$.

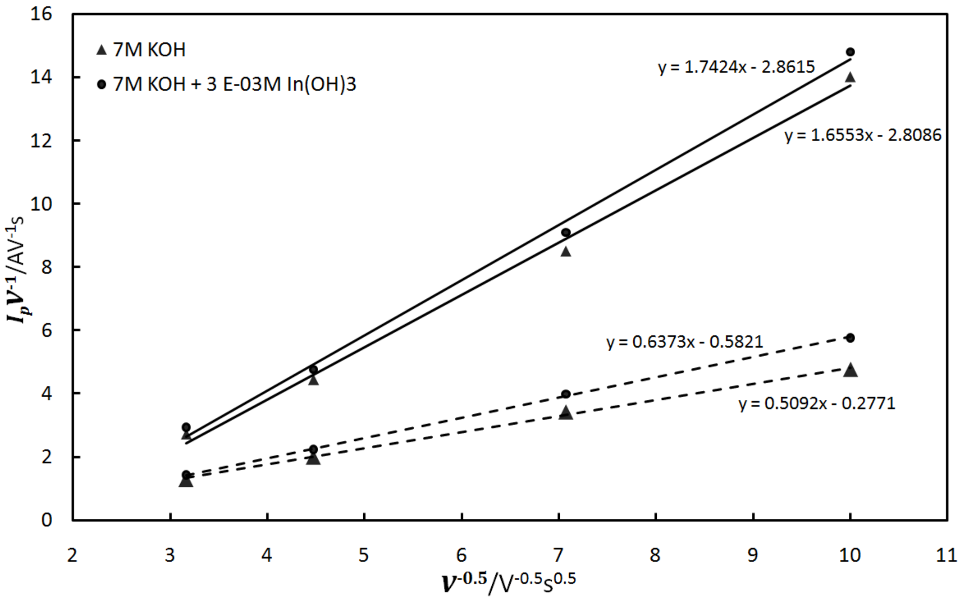

Figure 59: Plot of anodic and cathodic peak currents i_p vs. $v^{1/2}$ for ZnO in 7M KOH and in 7MKOH + $3.0x10^{-3}$ M In(OH)$_3$ at 25°C; anodic (——) and cathodic sweep (----).

Zincates solution	Anodic		Cathodic	
	k_{ct}	k_{diff}	k_{ct}	k_{diff}
7M KOH	2.81	1.65	0.28	0.51
7M KOH +$0.6x10^{-3}$M In(OH)$_3$	2.86	1.74	0.58	0.64

Table 7.1: Anodic and cathodic characteristics of charge-transfer constant (k_{ct}) and the diffusion controlled constant (k_{diff}) of the cyclic voltammogram for ZnO in 7M KOH and in 7M KOH + 3.10-3 M In(OH)$_3$.

7.3.4 Electrochemical Impedance Analysis

The impedance analysis of zincate reduction on a copper substrate in 7M KOH + 1.7wt% ZnO solution with or without In(OH)$_3$ was carried out. The EIS was performed at a steady cathodic current of 20mA and AC amplitude of 10mA. Figure 7.10 represents the complex plane diagrams for the blank, $1.2x10^{-3}$M, $1.8x10^{-3}$M, $2.4x10^{-3}$M, and $3.0x10^{-3}$M In(OH)$_3$ additives. The spectra show depressed semi circles with a rising portion of the impedance plot indicating a diffusion-controlled reaction. The impedance spectra were fitted using a Randles circuit where R_s is the solution resistance, CPE is the double layer capacitance and where the polarization resistance is represented by a combination of charge-transfer kinetic (R_{ct}) and solution diffusion (W_o) processes. The values of the electrical circuit components are listed in Table 7.2. The parameter α characterizes the nonideal capacitative behavior of the system due probably to the surface roughness. The values of α vary from 0.71 to 0.79 and the data show that the capacity value rises with increasing the indate concentration. Such a rise could be related to the increase of the charge at the interface of the electrode. R, P and T are parameters defining the open Warburg impedance W_o.

Electrolyte composition	R_S (mΩ)	CPE		R_{ct} (mΩ)	W_o		
		C (F)	α		R	P	T
7M KOH + 1.7wt% ZnO (A)	42	0.058	0.79	59	0.061	0.74	0.39
A + 1.2E-03M $In(OH)_3$	42	0.11	0.72	43	0.026	0.32	0.41
A+ 1.8E-03M $In(OH)_3$	43	0.21	0.71	28	0.035	0.53	0.41
A + 2.4E-03M $In(OH)_3$	41	0.28	0.74	18	0.043	0.73	0.38
A + 3.0E-03M $In(OH)_3$	41	0.55	0.71	17	0.039	0.52	0.38

Table 7.2: Values of the electrical circuit components to fit the impedance spectra of the zinc deposition in 7M KOH.

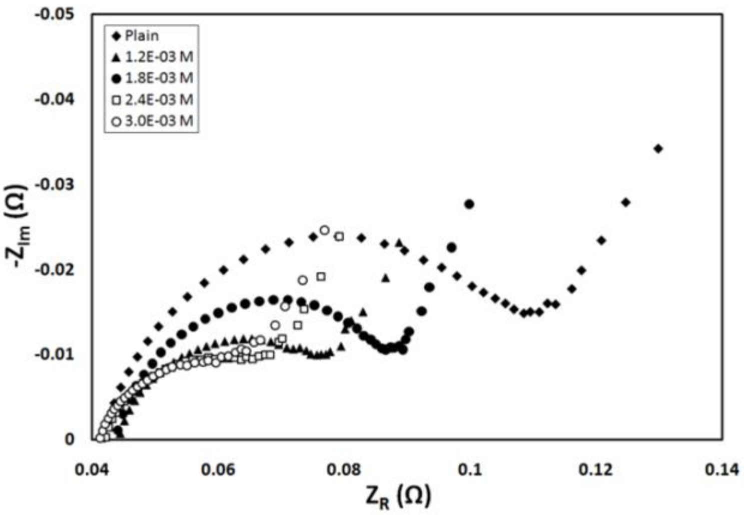

Figure 60: Complex impedance spectra (Nyquist plot) of the zincate reduction in 7M KOH with and without indate additives; between 0.1 and 1MHz at 20mA cathodic current and 10mA AC amplitude at 25°C.

The variation of the charge transfer resistance R_{ct} as a function of the indate concentration is illustrated in Figure 7.11. The results show that $In(OH)_3$ does not noticeably influence the solution resistance R_s that averages 42 mΩ whereas the charge transfer resistance R_{ct} varies significantly. As shown, R_{ct} gradually decreases from 59 to 17 mΩ with increasing the concentration of indates and tends to reach a plateau at concentrations higher than 2.10^{-3}M $In(OH)_3$. These results are in agreement with the findings from the cyclic voltammetry experiment since they reveal the positive impact of indates on the zinc electrodeposition reaction.

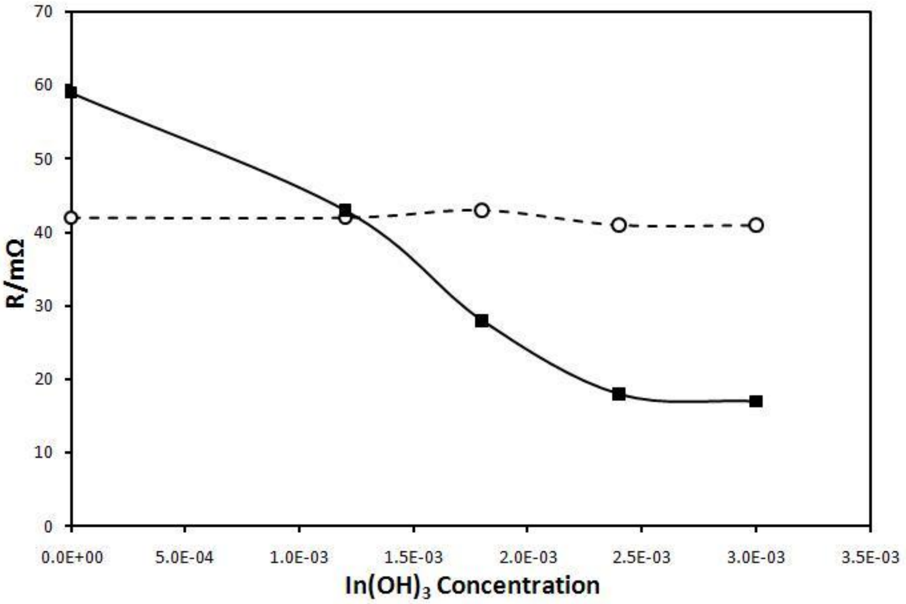

Figure 61: Effect of the indate concentration on solution resistance Rs (----) and the charge transfer resistance R_{ct} (——) of the impedance spectroscopy of zincate reduction in 7M KOH at 25°C.

7.4 Summary

Cyclic voltammetry and impedance spectroscopy revealed that Indium hydroxide has a positive impact on the zinc dissolution and deposition reaction in 7M KOH solution as both the charge transfer and diffusion rate showed an increase. The improvement of the charge transfer rate was attributed to the surface modification of the current collector caused by the reduction of indates. An optimum indates concentration ranging from 2.0 to $3.0x10^{-3}$M was suggested for a maximum effect in 7M KOH and it is argued that the optimum concentration corresponds to the solubility limit of indates.

Chapter 8

Characterization of zinc passive film by sonication in 7M KOH solution

Abstract

The influence of 40 KHz ultrasound radiation on the passivation behavior of zinc in 7M KOH is presented. The results of potentiodynamic and potentiostatic measurements combined with the current oscillation caused by the irradiation were examined to explain the mechanism and the sequence of formation of the oxide films during passivation. In this study, sonication was also used to investigate both effects of the passivation duration and passivation potential on the structure of the oxide layers; the adherence of the layers was found to depend strongly on both parameters. SEM-EDX analysis of the zinc surface provided complementary information on the oxide layer composition and structure.

8.1 Introduction

Understanding the anodic dissolution and passivation of zinc in alkaline solutions has always been of prime importance for alkaline batteries employing zinc electrodes. The passivation limits the utilization of a zinc electrode by forming an oxide layer that significantly reduces the rate of diffusion of electroactive ions towards and away from the unreacted zinc surface. The mechanism of passivation and the relationship between current density and passivation time for zinc anode have been intensively studied and it is generally agreed that zinc oxide film is responsible for the passivation [111]. Although various theories related to the passivation of zinc in strong alkaline solutions have been emitted [112,113], the 'dissolution-precipitation' model has given some satisfaction. During the anodic dissolution, the concentration of dissolved species (zincate ions) near the electrode surface increases up to the critical value of supersaturation, causing the precipitation of insoluble solid phase of ZnO or $Zn(OH)_2$. The mechanism can be represented as follows:

$$Zn + OH^- \leftrightarrow Zn(OH)^- \tag{8.1}$$

$$Zn(OH)^- \leftrightarrow Zn(OH) + e^- \ (rds) \tag{8.2}$$

$$Zn(OH) + OH^- \leftrightarrow Zn(OH)_2 + e^- \tag{8.3}$$

$$Zn(OH)_2 + 2OH^- \leftrightarrow Zn(OH)_4^{2-} \tag{8.4}$$

Upon saturation by zincates, the following chemical reaction takes place:

$$Zn(OH)_4^{2-} \leftrightarrow ZnO + H_2O + 2OH^- \tag{8.5}$$

It is generally accepted that the passivation is characterized by the formation of a dual oxide layer, as described in Section 2.2.Diverse experimental techniques have been employed to characterize the passivation. Potentiodynamic sweep and potentiostatic discharge have been used solely or in combination with rotating ring disk electrode (RRDE) or electrochemical impedance spectroscopy (EIS). The study of the passive film stability has been reported by many workers [114, 44]. Mc Kubre et al. studied the reversibility of the passive film formation using a RRDE under controlled hydrodynamic conditions in order to show the oscillatory activation/passivation process on the electrode [45].

In the present study, the passivation behavior of zinc in sonicated 7M KOH media is studied and characterized in situ. The effects of the potential and the duration of passivation on the thickness of the passive film are investigated. The structural composition and formation sequence of the oxide layers are analyzed using the profile of the oscillatory (activation/passivation) behavior induced by the ultrasound. Sonication is a well-established characterization technique in the corrosion field where the media are generally of low alkalinity [115, 116]. The study of the ultrasound effect on the zinc corrosion resistance and passivation in lowly concentrated NaOH solutions has been reported in previous works [117, 118].

8.2 Experimental

8.2.1. Material preparation

The working electrode used in this study consisted of a 1 mm thick plate made of zinc (99, 99% pure) and purchased from Sigma-Aldrich. Before each experiment, the electrode surface was mechanically polished with a silicon carbide paper (400 grits) followed by a slight etching in concentrated nitric acid and a thorough rinsing with deionized water.

The work was carried out in 7M KOH solution prepared from reagent-grade chemicals and deionized water. The solution was saturated with zincates by dissolving in ZnO (Aldrich 99.99%) and was purged with nitrogen prior to use. A nitrogen blanket was maintained throughout the experiment.

8.2.2. Apparatus

The three-electrode electrochemical cell made of PMMA block and described in section 3.1.2 was used. An UP100H ultrasonic probe from Hielscher was inserted in the cell through the filling port hole. The probe was immersed half way of the electrolyte high. All experiments were performed at a constant ultrasonic frequency of 40 KHz and under room temperature conditions. The duration of the exposure to sonication varied according to the requirement of the study.

8.2.3 Electrochemical measurement

A battery tester from Arbin Instruments was used to perform the potentiodynamic sweep and the steady state polarization experiments. The polarization sweeps were all carried out at a scan rate of 5mV.s^{-1}. The shape of the polarization curve and the magnitude of the resulting current were analyzed.

8.2.4 Surface characterization

The surface structure and morphology was investigated using a scanning electron microscope (SEM). The elemental analysis was performed using an energy dispersive X-ray scanner (EDS) built in the SEM.

8.3 Result and discussion

8.3.1 Effect of sonication on the surface passivity

The polarization curve of zinc in 7M KOH was first investigated in absence of sonication by performing a potentiodynamic sweep followed by a potentiostatic period at 400mV. A typical current-potential curve of zinc was obtained as shown in Figure 8.1. Two anodic peak currents attributed to the oxidation of zinc are observed. The first peak (less anodic) is representative of the zincate ions dissolution, $Zn(OH)_4^{2-}$, and the second peak (more anodic) is indicative of the precipitation of ZnO upon supersaturation of the solution with zincates at the vicinity of the electrode surface. The first peak current reaches a current density of 290mA.cm^{-2}. As the oxide precipitates, the current density decays down to 200mA.cm^{-2}. The precipitated ZnO is rather flaky in absence of stirring and corresponds to the typeI [44]. As the potential sweep continues the TypeI ZnO layer accumulates. The surface coverage by TypeI ZnO causes the depletion of OH^{-} ions near the electrode surface, resulting in the formation of typeII ZnO film[44]. The formation of typeII film is believed to be responsible for the transition from the active to the passive state of zinc characterized by the sharp decrease of the anodic current. In our case the sudden drop of the anodic current is seen at overpotential of 250mV. Such a behavior is in good agreement with those reported in the literature [44, 45]. The passivating current density reaches 10mA.cm^{-2} and slightly increases up to 30mA.cm^{-2} as the potential scan goes from 250 to 400mV.

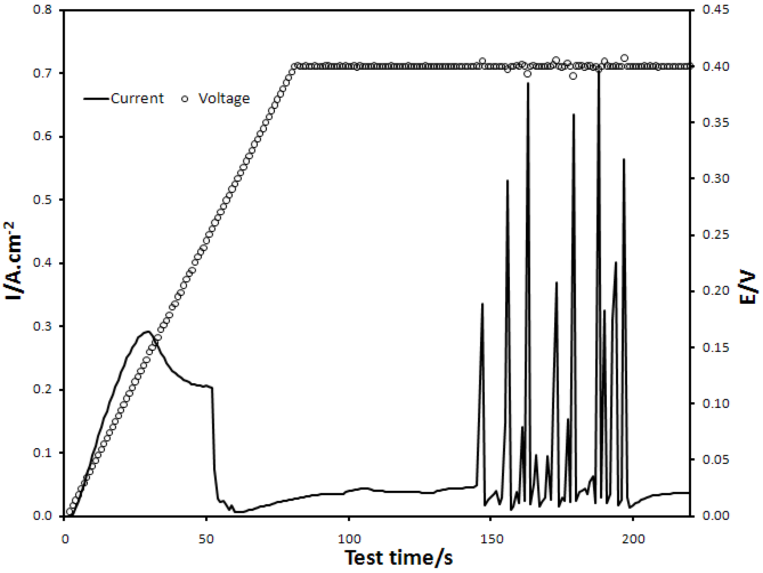

Figure 8.1: Polarization curve of zinc in 7M KOH in silent and irradiated conditions.

At 400mV, the potential is maintained constant and the passivating current density seems to stabilize at 0.036 A.cm^{-2}. After about 143s of test time the ultrasound bath is initiated and the cell is under irradiated condition. Figure 8.1 clearly shows that sonication promotes the passivation break down resulting in the formation of a current spectrum. At 200s of test time the sonication is stopped and the passivation current density drops back to 0.036A.cm^{-2}. The obtained current spectrum may provide structural and diffusional information about the electrode surface.

a. Current spectrum

The current spectrum is the result of the mechanical damage caused by the ultrasound to the oxide layers. The removal of the oxide layers allows for further dissolution as OH^- ions access fresh zinc surface giving rise to sudden current jumps. The presence of peaks suggests that the electrode surface quickly re-passivates after the breakdown of the initial passive layers, resulting in a current oscillation at the steady passive potential (400mV overpotential). The oxide layer breakdown caused by the irradiation was investigated by carrying out a SEM-EDX surface analysis. Two samples were anodically polarized at a constant potential of

350mV for 10min. One of the samples was conditioned by exposure to 40 KHz ultrasound radiation for 1min after the polarization. The electron micrograph in Figure 8.2 shows the presence of a porous ZnO layer on the surface of the non-conditioned sample. A partial removal of the oxide layer is noticed on the surface of the irradiated sample since only few randomly distributed ZnO crystallites are observed, as illustrated in Figure 8.3.

Figure 8.4 (a) and (b) shows a closer morphology examination of the ZnO under layers. It is revealed that the irradiated sample has more reaction pits, suggesting a stronger attack of the surface during the dissolution.

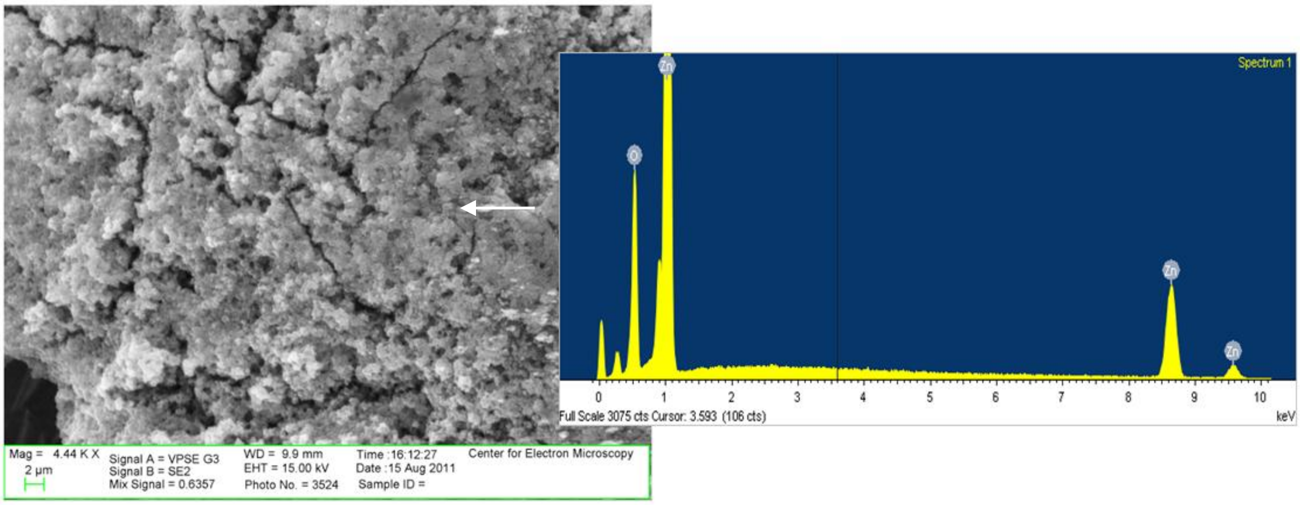

Figure 8.2: SEM micrograph and EDS Spectrum of zinc surface polarized at 350mV constant voltage for 5min under silent conditions.

b. Intensity and position of peaks

The spectrum in Fig2 consists of various peak intensities. The highest peaks approach 0.70 $A.cm^{-2}$ as opposed to $0.29A.cm^{-2}$ obtained in silent conditions (no irradiation). The significant rise in peak current under sonication condition could partially be attributed to the increase in the mass transport. It is well known that ultrasound increases mass transfer in electrochemical process [119]. Another non-negligible factor could be the slight increase of the electrode surface area upon etching due to dissolution.

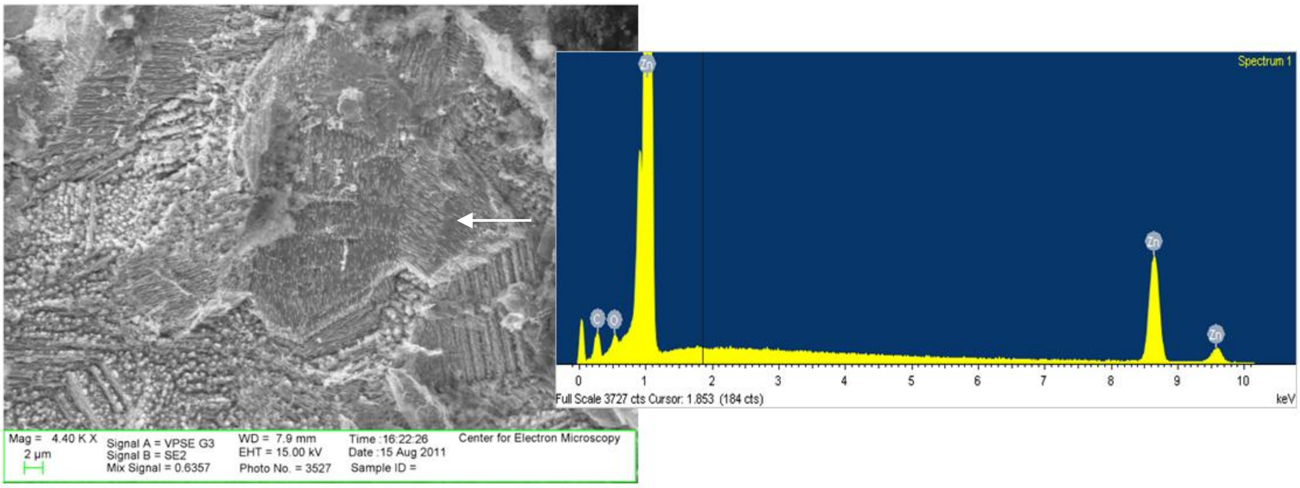

Figure 62: SEM micrograph and EDS Spectrum of zinc surface polarized at 350mV constant voltage for 5min under irradiation conditions.

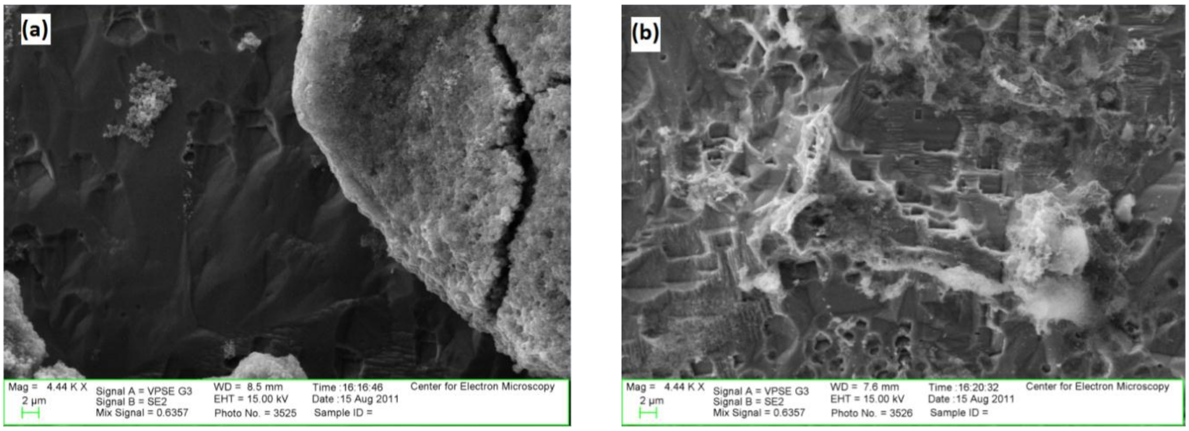

Figure 8.4: SEM micrographs of the cavities on the zinc after an anodic polarization at 350mV constant voltage for 5 min: (a) under silent conditions; (b) under ultrasound irradiation.

The peaks of low intensity probably result from the removal of the less adherent or porous oxide films whereas the high intensity peaks are likely indicative of the breakdown of all oxide layers including the most adherent or compact ones. Such an interpretation leads to think that the oxide layers constitutive of the passive film may be either of different thicknesses or structures as commented above. The thickness of a given oxide layer may vary from one region to another of the electrode surface due to the presence of preferential sites for the dissolution reaction.

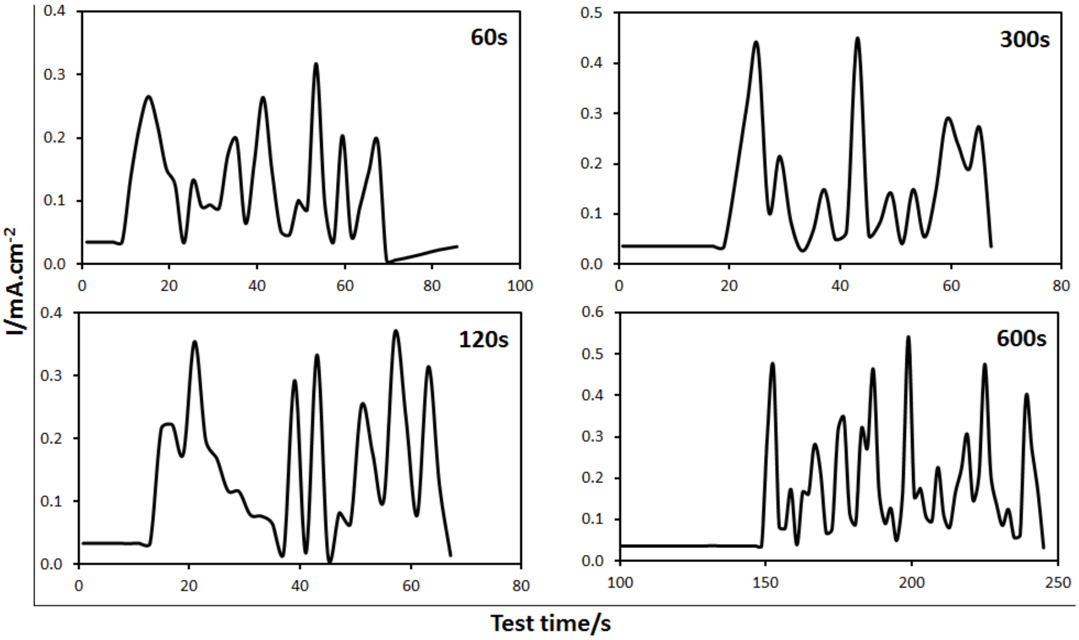

Figure 8.5: Current spectrum of zinc electrodes at a passive potential of 400mV under sonication conditions (40 KHz). Prior to the sonication exposure, the electrode surfaces were passivated for: 60, 120, 300 and 600s.

8.3.2 Characterization of the passive film growth

The growth of the passive film was investigated by initiating the sonication at various time intervals on the electrodes that were anodically polarized at 400mV overpotential (passive state). Figure 8.5 shows the current spectrum of the electrodes irradiated after 60, 120, 300 and 600s of time spent in passive state. The times of appearance of the first peak were recorded. The data show that the longer the time spent in passive state the later the peak appearance. The peak appearance time (t_{ap}) of the electrode irradiated after 60s is 7s whereas that of the electrode irradiated after 600s is 150s. The peak appearance time corresponding to the electrodes irradiated after 120 and 300s are 13s and 20s, respectively. The results suggest either a thickness growth or an increase in adherence of the oxide layers with the passivation time. These effects are not proportional given the variation of t_{ap}. All spectra exhibit peaks of various intensities, indicative of the presence of oxide layers of different structures. It is also found that the intensity of the highest current peak rises as the passivation time is prolonged. Such an effect may be the result of an increase of the active surface area of the electrode with dissolution. The highest peak points at 320mA.cm^{-2} for 60s, 375mA.cm^{-2} for 120s, 450mA.cm^{-2} for 300s and 550mA.cm^{-2} for 600s.

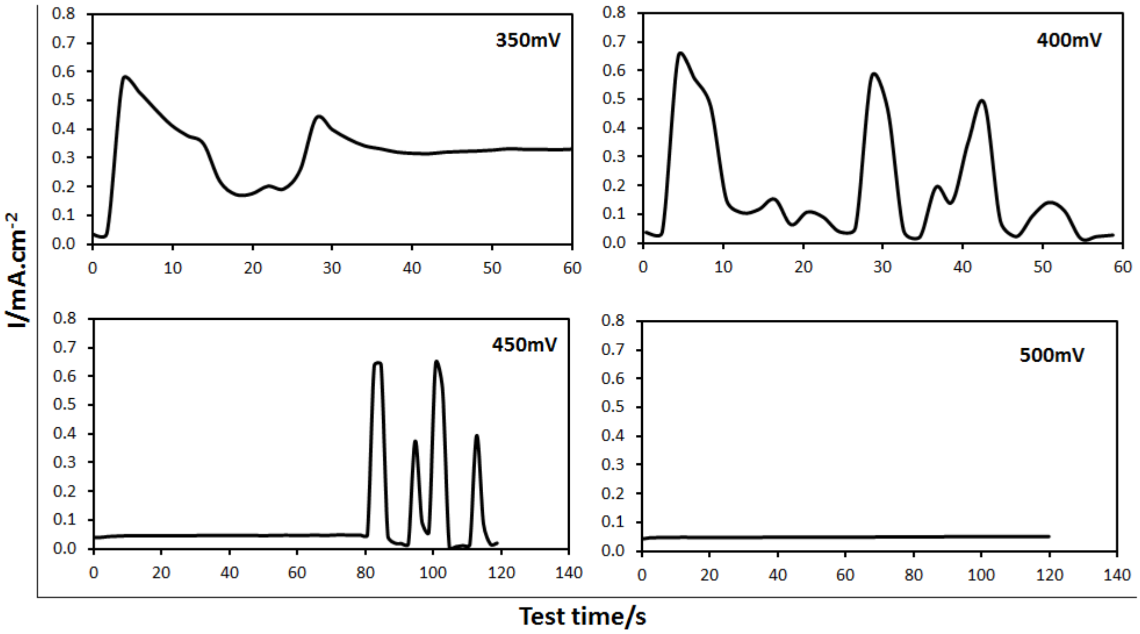

Figure 63.6: Current spectrum of zinc electrodes at various passive potentials (350, 400, 450 and 500mV) under sonication conditions (40 KHz). Prior to the sonication exposure, the electrode surfaces were passivated for 300s.

8.3.3 Investigation of the potential effect on the oxide layer structure

Steady state polarization was carried out on the electrodes at various potentials of passivation for 300s. Then, the electrodes were exposed to the ultrasound radiation while maintaining the potentials constant. Figure 8.6 shows the different spectra obtained at 350, 400, 450 and 500mV overpotential from the irradiation starting time. The data suggest that the higher the passivating potential the later the time of appearance of the first peak. At 350mV overpotential the breakdown of the passive film is readily within the first two seconds. The first peak points at 5s at 400mV whereas that of 450mV shows up at 80s. No peak appearance is observed at 500mV overpotential during 120s of irradiation time. The examination of the peak shape of the electrode polarized at 350mV overpotential shows no surface re-passivation. The current density decays from the first peak undergoing an oscillation to reach a steady state at 350mA.cm^{-2} after 40s of irradiation. In this particular case the decay in current may be ascribed to a porous oxide layer that is not strongly attached to the electrode surface. This oxide layer is probably of a structure similar to that of the ZnO of typeI discussed above. The steady state current is the result of equilibrium between the rate of formation and removal of the oxide. The spectrum at 400mV overpotential exhibits a combination of high and low peaks and a sign of surface re-passivation. It is also noticed that upon the appearance of the first peak, the current density does not immediately drop down to the initial passive current of 35mA.cm^{-2}. It stabilizes at 100mA.cm^{-2} for 5s, which may be indicative of the presence of porous oxide layers. If so, then the data suggest that the porous oxide layer forms before the dense layer. Powers and Breiter [44] have demonstrated identical sequence in the formation of the oxide layers.

The spectrum at 450mV overpotential shows no small peak after re-passivation since all peaks are higher than 400mA.cm^{-2}. At 500mV overpotential the passive film seems stable despite the ultrasound radiation, accounting for the total absence of peak. These results point out to the dependence effect of the structure of the passive film. In fact, high potentials may favor more compact or adherent layers.

8.4 Summary

The objective of the present work was to investigate the effect of sonication on the passivation of zinc in a highly concentrated KOH solution. The experiment showed that a passive surface can become active again when it is exposed to ultrasound radiations (40 KHz). The re-activation of the passive surface was ascribed to the breakdown of the oxide layers which is caused by the ultrasound vibration. It was also found that zinc surface quickly re-passivates when polarized under sonication conditions, giving rise to a current oscillation over time. The understanding of the oscillation response allowed for the study the effect of some influencing parameters such as the duration and the potential of passivation. The data revealed that both parameters affect either the structure or the adherence of the oxide layers. A growth or densification of the passive layers was suggested with increasing the passivation potential or the exposure time in passive state. At overpotential as high as 500mV, the structure of the passive film becomes very resistant to the 40 KHz sonication in 7M KOH.

Chapter 9

Impact of the passivation on the zinc electrode charge performance

Abstract

In this section the effect of the passive film formed during the discharge on the charge behavior of the zinc electrode was investigated. The study was performed using voltage sweep and potentiostatic as well as galvanostatic techniques in zincate-saturated KOH solutions in various concentrations of 2, 6 and 11M. The results lead to a tentative conclusion that the effect of the passive film on the charge voltage is rather minim in highly concentrated KOH solutions. The effect seems to be more significant in solutions of low alkalinity where the kinetics of the reduction reaction of zincates is slowed down.

9.1 Introduction

Passivation takes place at the electrode surface during the cell discharge. Extensive studies by numerous investigators led to the understanding of the passive film formation and the effect of the electrode potential on its stability. In batteries, maintaining the potential of charge low is critical in order to achieve high charge efficiencies on zinc because of the risk of evolving hydrogen due to overpotential. One major factor that has strong impact on the zinc electrode potential during charge relates to the chemical dissolution rate of ZnO. In fact, ZnO dissolves in alkaline solution producing zincates which are reduced in charge, as demonstrated in Equation 1.1. It is therefore important to ensure a quick dissolution of ZnO on the demand, otherwise the solution may lack of zincate ions to sustain the charge reaction, resulting in a sudden rise of the electrode potential. This work intends to investigate the effect of the passive film on the kinetics of the zinc deposition reaction in alkaline solutions.

9.2 Experimental

9.2.1. Material preparation

A zinc plate (99,99% pure, Sigma-Aldrich) was used as the working electrode for the electrochemical cell. The plate was 1mm thick and, before each experiment, its surface was mechanically polished with a silicon carbide paper (400 grits) followed by a slight etching in concentrated nitric acid and a thorough rinsing with deionized water.

The work was carried out in KOH solution prepared from reagent-grade chemicals and deionized water. The solution was saturated with zincates by dissolving in ZnO (Aldrich 99.99%) and was purged with nitrogen prior to use. A nitrogen blanket was maintained throughout the experiment.

9.2.2. Apparatus

a. Electrochemical cell

A conventional three-electrode cell described in section 3.1.2 was used as the setup for the voltammetry experiments.

b. Full cell

The validation in a full system was carried out in zinc-air 675 button cells. The description of the cell is given in section (3.1.1).

9.2.3. Electrical performance measurement

Potentiostatic and galvanostatic technique were both used to partially discharge the cells in different conditions favoring or not the passivation of the electrode surface. The cells were afterward charged and their respective voltages were examined. In order to study the reaction kinetics, potentiodynamic sweep was carried out at a scan rate of $5mV.s^{-1}$. The shape of the polarization curve and the magnitude of the resulting current were analyzed. The measurements were performed using a computer–controlled tester from Arbin.

9.3 Result and Discussion

9.3.1 Discharge voltage sweep analysis

The objective of the experiment was to determine the active and passive potential regions of the different systems. Figure 9.1 shows the polarization curves of the zinc electrode in zincate-saturated KOH solutions of various concentrations (2M, 6M and 11M). The experiments were performed at a scan rate of 5mV/s. The resulting curves show an active, passive-transition and passive regions. The current and potential peaks as well as the passivation potential show an increase with the KOH concentration. The observed trends are consistent with the general knowledge that zinc electrode is more prone to passivate in solutions of low alkalinity.

9.3.2 Effect of the passive film on the electrodeposition kinetics

In this section, freshly etched zinc electrode was discharged at a constant voltage in such a way to promote the formation and growth of both passive and non-passive film. According to Figure 9.2, 100 and 400mV are overpotentials characterizing to the active and passive state of the surface, respectively. Therefore, the two overpotential values were chosen for the respective potentiostatic experiments. These experiments were performed on a zinc plate working electrode until attainment of steady current and a capacity of 15C. An example of the current variation as a function of time in 6M KOH is shown in Figure 9.2.

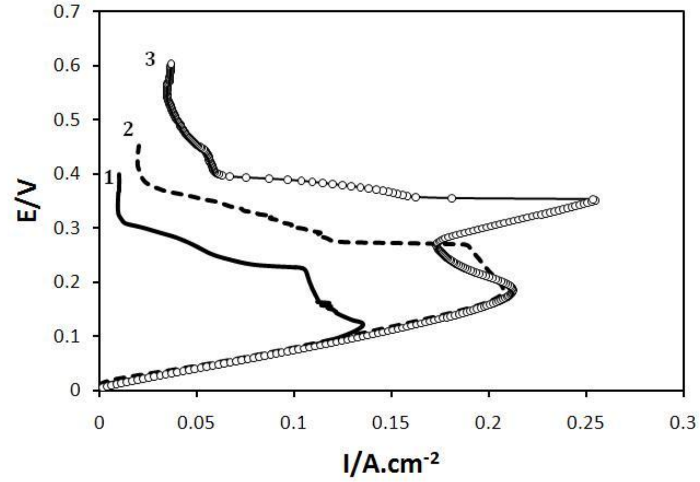

Figure 9.1: I-E curve of zinc electrode in KOH solution in various concentrations, saturated with zincate: (1) 2M, (2) 6M and (3) 11M KOH.

At 100mV overpotential the current of the discharged electrode stabilizes at 0.15A.cm^{-2}, indicating that the electrode surface remains active. The surface morphology of the electrode before and after the polarization at 100mV is presented in Figure 9.3. A current density of 0.5A.cm^{-2} is obtained from the very start when the electrode is polarized at 400mV overpotential followed by a rapid decay down to 0.027A.cm^{-2}. The sudden drop in current is a characteristic of passivation.

Once the potentiostatic discharge completed, the electrode was rested for 60s and a charge voltage sweep was performed then after. The polarization curves obtained from the cathodic polarization sweep in 2, 6 and 11M zincate-saturated KOH are illustrated in Figure 9.4 – 9.6.

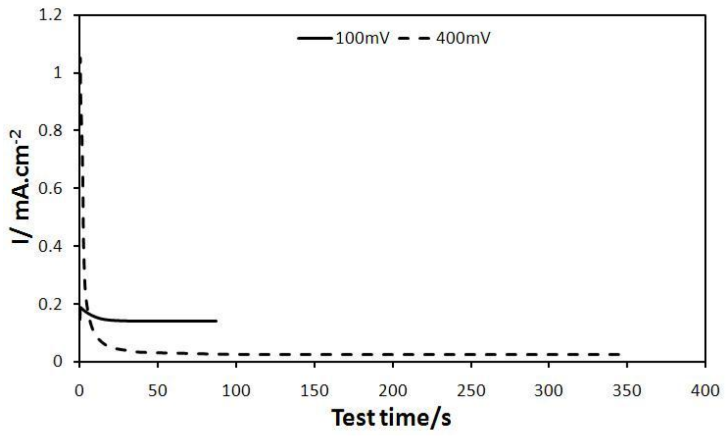

Figure 9.2: Current density variation as a function of time of the zinc plate electrode anodically polarized at 100mV and 400mV overpotential in 6M KOH.

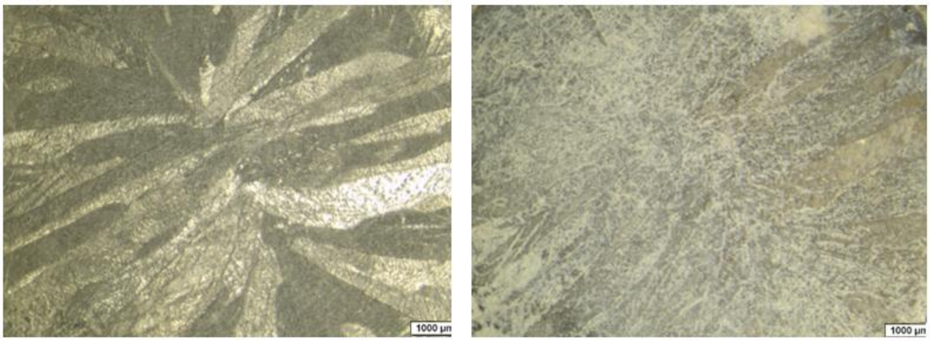

Figure 643: Surface morphology of the zinc plate before (a) and after (b) the anodic polarization at 100mV overpotential in 6M KOH.

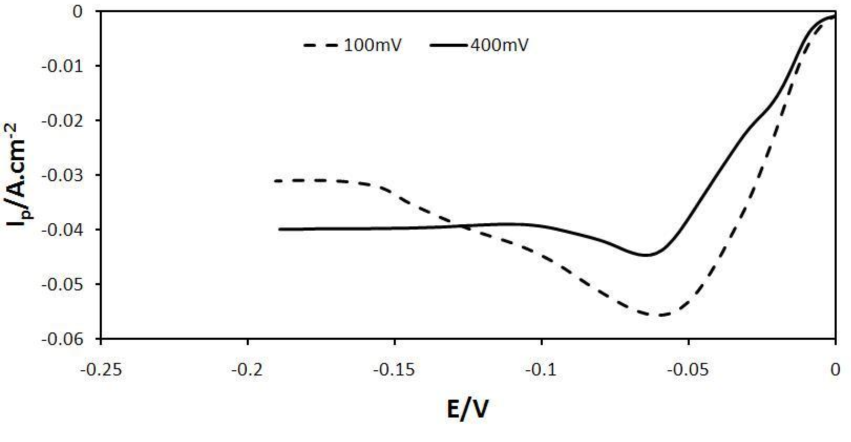

Figure 9.4: I-E curve of cathodic polarization sweep in zincate-saturated 2M KOH at 5mV.s^{-1} scan rate.

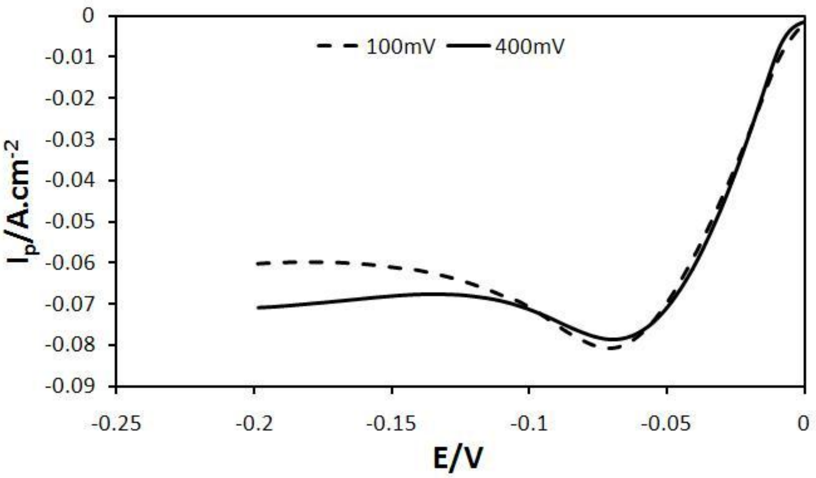

Figure 9.5: I-E curve of cathodic polarization sweep in zincate-saturated 6M KOH at 5mV.s^{-1} scan rate.

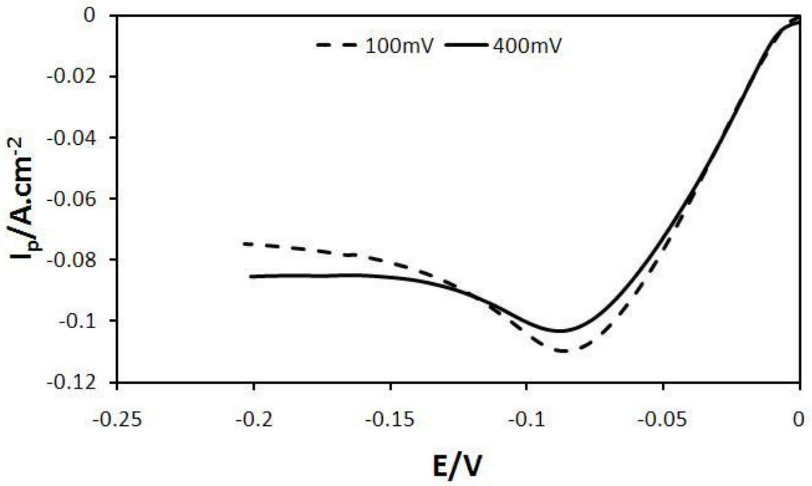

Figure 9.6: I-E curve of cathodic polarization sweep in zincate-saturated 11M KOH at 5mV.s^{-1} scan rate.

Zincate-sat. KOH	Peak current density I_p (mA/cm^2)			Overvoltage η @ 45 mA/cm^2		
	Active	Passive	ΔI_p (%)	Active	Passive	Δ η (%)
2M	55	44	-20	38	65	71
6M	81	79	-2.5	30	30	0
11M	109	103	-5.5	31	31	0

Table 9.1: Current density peak and overvoltage performances summary.

Surprisingly, the state of passivation resulting from the potentiostatic polarization at 400mV does not seem to significantly influence the charge voltage behavior in highly concentrated electrolyte, as summarized in Table 9.1. The peak current density variations (ΔI_p) of only 2% and 6% were recorded in 6M and 11M KOH, respectively. The largest variation of ΔI_p was obtained in 2M KOH solution, where the current peak drops by about 20% and the overvoltage η increases by 71% at a randomly current density of 45mA/cm^2. At that same rate, the 6 and 11M KOH system almost show no variation in overpotential. Note that the peak potentials remained invariant for all three systems. The data may indicate that the passive film formed in 2M KOH is probably more compact and resistant than that formed in 6 and 11M KOH solutions.

9.3.3 Effect of the passive film thickness on the electrodeposition potential

Figure 9.7 shows the polarization curves of a series of cathodic polarization sweeps performed on a zinc electrode following an anodic polarization at a constant potential of 400mV (passive region) in a zincate-saturated 11M KOH solution for various capacities (5, 10, 20, 30 and 40C). Various discharge capacities were investigated in order to study the thickness effect of the passive film which seems to grow upon continued dissolution, as discussed in Chapter 8.

The variation of the cathodic peak current density and the overvoltage at the current density of 45mA/cm^2 are illustrated in Figure 9.8. It is demonstrated that the kinetics of the reduction reaction of zincates slows down with increasing the discharge capacity (thickness of the passive film) up to a maximum value beyond which the reaction kinetics is accelerated again. The increase in the reaction kinetics is characterized by the rise of the current peak and the decrease of the overvoltage. A probable explanation of such a behavior could be the meta-stability of the passive film; as the film becomes thicker it tends to break down and peel off from the electrode surface (3).

Cathodic polarization sweeps were performed at various scan rates ranging from 10 to 80mV/s on a zinc electrode of identical state of discharge of 15C, obtained under different surface conditions. The first discharge (anodic polarization) was carried out at 100mV overpotential (active state), followed by the first series of the cathodic polarization sweep. After completion, the electrode surface was refreshed and underwent a second discharge at a constant overpotential of 400mV (passive state), followed by the second series of the cathodic polarization sweep.

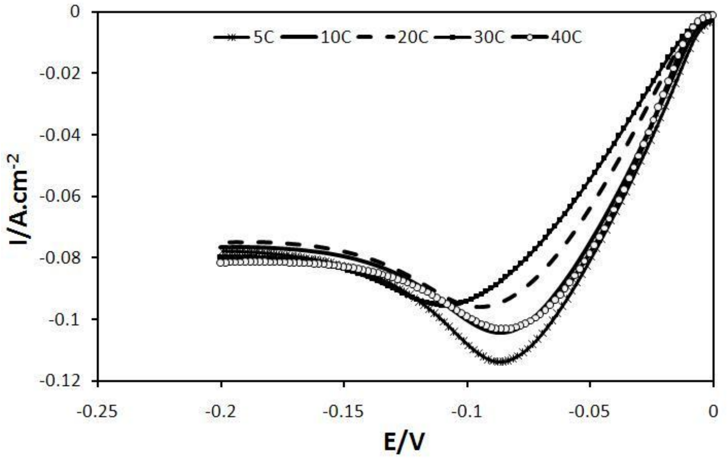

Figure 9.7: I-E curve of the cathodic polarization sweep of the zinc electrodes of various discharge states in zincate-saturated 11M KOH.

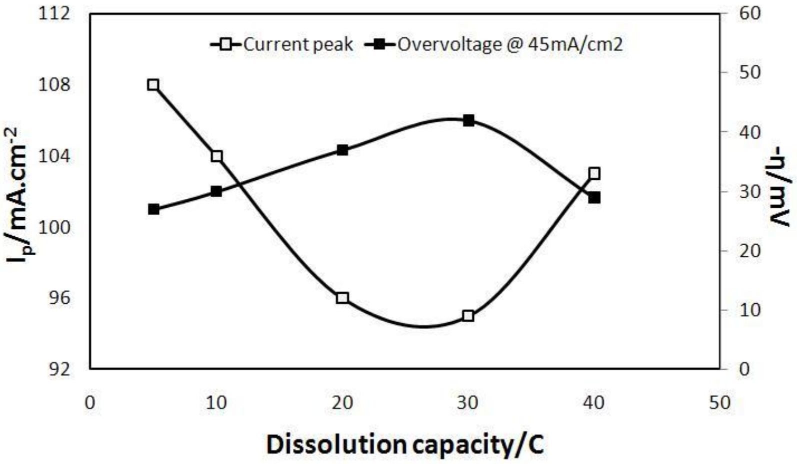

Figure 9.8: Variation of the peak current density I_p and overvoltage η (at 45mA/cm^2) as a function of the discharge capacity of the zinc electrode.

Figure 9.9 shows that the current densities at the peaks of the deposition reaction increase with increasing sweep rate. The lack of a fully linear relationship between the peak current and the square root of the sweep rate suggests that the zinc deposition reaction is not totally controlled by diffusion. It is also shown that the electrode discharged in passive state exhibits smaller charge transfer coefficient than that of the electrode discharged in non-passive state, according to Equation 7.1.

9.3.4 Effect of the passivation on the charge voltage of the 675 button cell

In this section, two 675 button cells were cycled at the same capacity but under different discharge regimes. Both cells had an open circuit voltage around 1.4V. The first cell was subjected to a potentiostatic discharge at 0.5V resulting in an initial current density of 100mA.cm^{-2} that quickly dropped to a steady value of 12mA.cm^{-2}. The second cell was discharged at a constant current density of 15mA.cm^{-2} and an average discharge potential potential of 1.2V was obtained.

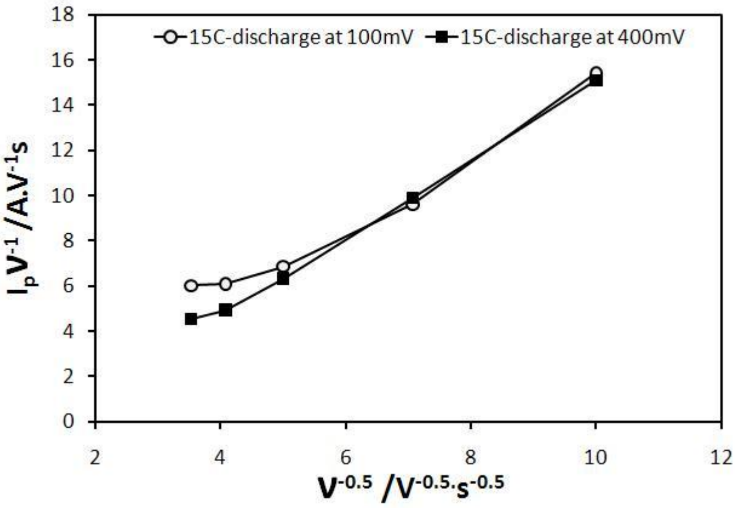

Figure 9.9: Plot of the charge current density peak I_p vs. $v^{-1/2}$ of zinc electrodes with passive and active surface in 11M KOH saturated with zincates.

Upon attainment of the desired capacity of 20mAh, the two cells were put on charge at a constant drain rate of 15mA.cm^{-2}. Figure 9.10 shows the variation of the respective charge voltages as a function of time. A 30mV difference is exhibited between the charge voltage of the first cell and that of the second cell.

The first cell shows higher charge potential because of the high discharge polarization that probably caused the surface of the zinc grains inside the battery to passivate; The zinc mass in the second cell was certainly not as stressed due to the low current drain rate.

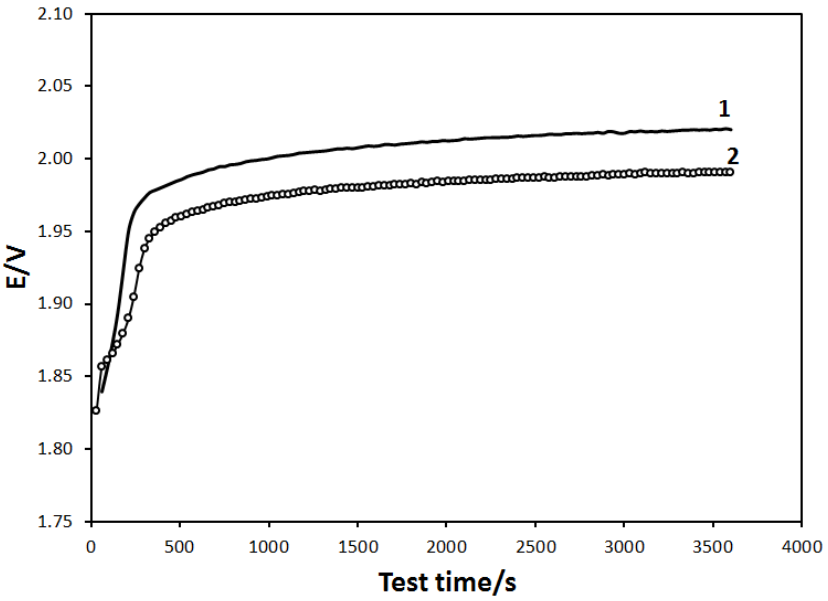

Figure 9.10: Charge potential curve of zinc-air 675 button cells discharged at a constant potential of 0.5V (1) and at a constant drain rate of 15mA.cm^{-2} (2). The charge current density is 15mA.cm^{-2} and the discharge capacity is 20mAh.

9.4 Summary

It was found that the passive film formed in 2M KOH can markedly slow down the kinetic of the zinc deposition reaction whereas the films obtained in highly concentrated solutions do not seem to have significant effect. The investigation carried out in zinc-air batteries (675 button cells) containing 7M KOH suggested a slight effect on the behavior of the system charge voltage. In the light of the present finding we are inclined to believe that the passivation of zinc can impact the reaction kinetics of the electrodeposition. The effect may be more pronounced in battery systems. Therefore, it is judicious to control the discharge potentials in order to achieve high charge efficiency.

Chapter 10

Conclusion

The zinc chemistry in highly concentrated alkaline solutions is used in a variety of battery systems. The reaction mechanism involves both solids phases and ion intermediates. The zinc reaction generally involves an undesirable side reaction which is responsible for the formation of the hydrogen gas. The entrapment of the gas largely contributes to the heterogeneity of the current density distribution across the surface and throughout the bulk of the zinc active mass. Entrapped gas causes the cell internal resistance to increase. Several approaches to address the gassing issues have been studied as discussed in the introduction of this Thesis. These approaches include the usage of alloying element in zinc and additive in electrolyte, as well as the coating of the current collector, as discussed below.

The alloying elements lodge at the grain boundaries of the zinc particle where they segregate by diffusion. We found that lead dissolves as the zinc electrode discharges and does not reform during the reverse process (charge). Indium remains incrusted in the porous ZnO layer resulting from the discharge of the electrode. The indium alloying element may oxidize during the process. The deposited zinc resulting from charge was found to be alloy-free, suggesting an inhomogeneity of the surface redistribution of the alloying elements upon sequent cycles. This observation showed the limit of alloying to effectively inhibit the HER in secondary cells and justifies the necessity to seek other solutions out.

Both zinc corrosion and polarization performance data were collected in presence and absence of $In(OH)_3$. The finding is in agreement with the conclusion of Yoshizawa [107] who asserted that $In(OH)_3$ reduces the rate of corrosion of zinc. $In(OH)_3$ was found to positively impact the zinc reaction mechanism and the optimal effect was observed for concentration ranging from 2.4×10^{-3}M to 3.0×10^{-3}M.

This work can be extended to other indium salts such as $InCl_3$, $In(NO_3)_3$ and $In_2(SO_4)_3$. Tin salts may also be of interest.

Galvanic coupling as a driving force for the corrosion of zinc electrode was ascertained and the effect of coating the copper current collector with indium was investigated. The coating was done electrochemically in an electrolytic sulfamate bath and the study was carried out in 675 button cells. The stability of the indium coat was examined by mean of CV in an electrochemical cell and repeated cycles in the button cells. The results indicate that an indium coat can tremendously cut down the corrosion rate of the electrode without impeding the cell. The only downsides are the cost of indium and its stability upon subsequent cycles in rechargeable cells.

An important factor that has not been examined in the present Thesis is the effect of the cell potential on the degradation of the indium layer. The indium coat lifetime may be significantly prolonged with adjusting the discharge and the charge voltage cut-off.

Another aspect of the zinc-copper coupling is reported through the assessment of the reaction mechanism of the zinc electrodeposition onto a copper substrate by mean of galvanostatic measurement technique. The data show that low current densities may result in low deposition efficiency of zinc. Besides the galvanostatic technique, an independent and different technique (EQCM) was used to validate the results. From the system point of view, the study points out to the necessity of tuning the current density of the charge reaction for an optimal performance. Any current loss due to inefficiency contributes to the formation of the hydrogen gas which generally leads to precocious cell failure. The current of charge should not be too large either otherwise the risk of evolving hydrogen because of the fast depletion of zincates from the solution is high. Note that the rate of the zincate reduction to zinc is much faster than that of the chemical dissolution of ZnO to form zincates.

The passivation of zinc in alkaline solution was studied by mean of sonication. The findings suggest that the passive film can be removed upon irradiation. The growth of the passive layer was found to be potential and time-dependent. The sequence of formation of the different oxide layers was examined. The data indicated a probable formation of a porous and less adherent oxide film followed by the growth of more compact and sticky layer during the polarization sweep. SEM-EDS was used to characterize the state of the electrode surface. This technique may have other potentials if it is fine tuned. Some areas which are worth considering are:

1) Effect of the probe frequency on the passive film stability
2) Analysis of the peak width and its relation to the film thickness
3) Sonication in presence of additives that retard or inhibit passivation

It is also reported in this Thesis that passivation can have significant effect on zinc electrodeposition in KOH solutions with concentration as low as 2M. The effect lessens as the concentration increases.

Bibliography

1. H. Morrows: Encyclopedia of Material Science and Technology, Vol. 7, M. B. Bever (ed), MIT Press, Cambridge, Massachusetts (1986).
2. L. Tongqing: The changing patterns of the global EMD business, IMI EPD Meeting (2006).
3. German patent 38,383 (1887).
4. J. Mc Breen, and E. J. Cairns: Adv Electrochem. and Electrochem. Eng., 11, 273 (1978).
5. A. Volta, Phil. Trans. R. Soc. London 90:403 (1800).
6. S. U. Falk, and A. J. Salkind, Alkaline Storage Batteries, Wisley, New York (1967).
7. H. André, Bull. Soc. Fr. Electrochem. (6th ser.) 1:132 (1941).
8. H. André, US Patent 2,317,711 (1943).
9. D. Linden, T. B. Reddy, Handbook of Batteries 3rd Edition, McGraw-Hill, New York (2001).
10. W. Tahil: Zinc air battery and zinc economy, Meridian International Research (2007).
11. J. D. Ivad, K. Kordesch: The status of rechargeable alkaline manganese dioxide/zinc battery, 190th Meeting of Electrochemical Society, 96-16, 11-22 (1996).
12. J. O'M. Bockris, J. McBreen and L. Nanis: The hydrogen evolution kinetics and hydrogen entry into a-iron, J. Electrochem. Soc., 112, 1025 (1965).
13. E. G. Dafft, K. Bohnenkamp and H. J. Engell: Investigations of the hydrogen evolution kinetics and hydrogen absorption by iron electrodes during cathodic polarization, Corros. Sci., 19, 591-612 (1979).
14. S. Y. Qian, B. E. Conway and G. Jerkiewicz: Kinetic rationalization of catalyst poison effects on cathodic H sorption into metals: relation of enhancement and inhibition to H coverage, J. Chem. Soc., Faraday Trans., 94, 2945-2954 (1998).
15. S. Y. Qian, B. E. Conway and G. Jerkiewicz: Electrochemical sorption of H into Fe and mild-steel: kinetic conditions for enhancement or inhibition by adsorbed HS^-, Phys. Chem., 1, 2805-2813 (1999).

16. S. Trasatti: Physical electrochemistry of ceramic oxides, Electrochim. Acta, 36, 225-241 (1991).

17. D. J. Walton, L. D. Burke and M. M. Murphy: Chlorine, hydrogen and oxygen evolution at platinized platinum, Electrochim. Acta, 41, 2747-2751 (1996).

18. B.E. Conway, J. O'M. Bockris: Electrolytic hydrogen evolution kinetics and its relation to the electronic and adsorptive properties of the metal, J. Chem. Phys., 26, 532 (1957).

19. P. Ruetschi, P. Delahay: Potential at Zero charge for reversible and ideal polarized electrodes, J. Chem. Phys. 23, 697 (1955).

20. R. Parsons: The rate of electrolytic hydrogen evolution and the heat of adsorption of hydrogen, *Trans. Faraday Soc.*, 54, 1053-1063 (1958).

21. Bard, A. J. (ed): Encyclopedia of Electrochemistry of the Elements, Vol. 9, Marcel Dekker, New York (1982).

22. Ruetschi, P.: Solubility and diffusion of hydrogen in strong electrolytes and the generation and consumption of hydrogen in sealed primary batteries, J. Electrochem. Soc. 114, 301-305 (1967).

23. R.J. Brodd, V.E. Leger, Zinc, in: A.J. Bard (Ed), Encyclopedia of Electrochemistry of the Elements, Vol. 5, Marcel Dekker, New York, (1974).

24. F. Manfeld, S. Gilman: The effect of potential and time on deposition characteristics of zinc on a zinc single crystal in KOH, J. Electrochem. Soc. 117, 1521 (1970).

26. H. Yoshizawa, and A. Muria: Mercury free alkaline manganese batteries, Prog. Battery Mater. 12, 132-139 (1993).

27. V. K. Nartey, L. Binder, and K. Kordesh: Identification of organic corrosion inhibitors suitable for use in rechargeable alkaline zinc batteries, J. Power Sources 52, 217-222, (1994).

28. J. Dobryszycki, S. Biallor: On some organic inhibitors of zinc corrosion in alkaline media, Corrosion Science 43, 1309-1319 (2001).

29. N. Shuster: Electrolyte compositions and methods, US patent 5108856.

30. C. Randell, and D. Kilby: Phosphate ester additive to alkaline cells to reduce gassing, US patent 5378559.

31. Lee, T. S.: Hydrogen overpotential on pure metals in alkaline solutions, J. Electrochem. Soc. 118, 1278-1282 (1971).

32. X.G. Zhang: Corrosion and Electrochemistry of Zinc, Plenum Press, New York (1996).

33. Fontana, M. G., and Greene N. D., Corrosion Engineering, 2nd ed., McGraw-Hill, New York (1978).

34. In Tae Bae: Alloy Formation at Electrodeposited Zinc–Copper Electrode Interfaces at Room Temperature, J. Electrochem. Soc., 155, D395-399 (2008).

35. P. Ruetschi: Solubility and diffusion of hydrogen in strong electrolytes and the generation and consumption of hydrogen in sealed primary batteries, J. Electrochem. Soc., 114, 301 (1967).

36. R. N. Snyder, and J. J. Lander: Rate of hydrogen evolution of zinc electrodes in alkaline solutions, Electrochem, Technol. 3 (5-6), 161-166, 1965.

37. T. P. Dirkse, and R. Timmer: The corrosion of zinc in KOH solutions, J. Electrochem. Soc. 116, 162-165, 1969.

38. D. P. Gregory, P. C. Jones, and D. P. Redfearn: The corrosion of zinc anodes in aqueous electrolytes, J. Electrochem. Soc. 118, 1684-1688, (1972).

39. Gilette Company: Hydrogen recombination catalyst, Patent US6333123, (2001).

40. Gilette Company: Hydrogen recombination catalyst, Patent US6500576, (2002).

41. H. Dietz, L. Dittmar, D. Ohms, M. Radwan and K. Wiesener: Noble metal-free catalysts for the hydrogen/oxygen recombination in sealed lead/acid batteries using immobilized electrolytes, J. Power Sources, Vol.40, page 175-186 (1992).

42. K-R. Kim, S-W. Paek, H-J Choi and H. Chung: Catalytic recombination of hydrogen and oxygen in air stream, J. Ind. Eng. Chem., Vol. 7, No. 2, 116-120 (2001).

43. K. Huber: Anodic Formation of Coatings on Magnesium, Zinc, and Cadmium, J. Electrochem. Soc. 100, 376 (1953).

44. R. W. Powers and M. W. Breiter: The anodic dissolution and passivation of zinc in concentrated potassium hydroxide solutions, J. electrochem. Soc. 116, 719 (1969).

45. M. C. H. Mc Kubre and D. D. Macdonald: The dissolution and passivation of zinc in concentrated aqueous hydroxide, J. Electrochem. Soc. 128, 524 (1981).

46. Liu, M., Cook, G. M., and Yao, N. P.: Passivation of zinc anode in KOH electrolyte, J. Electrochem. Soc. 128, 1663-1668, 1981.

47. Dirkse. T. P., and Hampson, N. A.: The Zn(II)/Zn exchange reaction in KOH solution—II. exchange current density measurements using the double-impulse method, Electrochim, Acta 17, 383-386, (1972).

48. V. N. Flerov: The ageing of supersaturated zincates, Zh. Fiz. Khim., 31, 49 (1957).

49. A. J. Appleby, J. Jacquelin, and J. P. Pompon, SAE Trans., Paper No. 770381 (1977).

50. A. Marshall, N. A. Hampson, and J. S. Drury, and J. P. G. farr: The effect of potassium silicate on the dissolution of zinc in alkali, J. Surface Technol. 5, 149 (1977).

51. W. G. Sunu and D. N. Bennion: Transient and failure analyses of the porous zinc electrode*,* J. Electrochem. Soc., Volume 127, Issue 9, pp. 2017-2025 (1980).

52. D. P. Boden, V. J. Spela and R. B. wiley: The electrode potential of zinc amalgam in alkaline zincate solutions, J. Electrochem. Soc., 118, 1298-1301 (1971).

53. J. McBreen: Zinc Electrode Shape Change in Secondary Cells, *J. Electrochem. Soc.,* 119, 1620 (1972).

54. K. W. Choi, D. N. Bennion, and J. Newman: Engineering analysis of shape change in zinc secondary electrodes. I. Theoretical, *J. Electrochem. Soc.,* 123, 1616 (1976).

55. J. Newman and W. Tiedemann, *Am. Inst. Chem.Eng. J.,* 21, 25 (1975).

56. W. G. Sunu and D. N. Bennion: Transient and Failure Analyses of the Porous Zinc Electrode. II. Experimental, J. Electrochem. Soc., 127, 2017 (1980).

57. T. C. Adler, F. R. McLarnon, E. J. Cairns: Low-zinc-solubility electrolytes for use in zinc/nickel oxide cells, J. Electrochem. Soc., 140, 289 (1993).

58. R. F. Plivelich, F. R. McLarnon, E. J. Cairns: Degradation mechanisms of nickel oxide electrodes in zinc/nickel oxide cells with low-zinc-solubility electrolytes, J. Appl. Electrochem. 25, 433-440 (1995).

59. E. G. Gagnon: Effects of KOH concentration on the shape change and cycle life of Zn/NiOOH cells, J. Electrochem. Soc. 133, 1989 (1986).

60. V. Takashi, I. Yoshikazu, jpn. Patent , 63, 26, 957; chemical Abstract: 108: P189965f.

61. V. Takashi, I. Yoshikazu, jpn. Patent , 63, 19, 767; chemical Abstract: 106: 1537118p.

62. A. Duffield, P. J. Mitchell, D. W. Shield, N. Kumar, in: L.P. Pearce(Ed), Power Source11, Int. Power Sources Symp. Committee, Leatherhead, P. 253 (1987).

63. E. Frąckowiak, in: T. Keily, B. W. Baxter (Eds.), Power Sources 13, Int. Power Sources Symp. Committee, Leatherhead, P. 225 (1991).

64. N. A. Zhulidov and F. I. Efremov: An alkaline storage cell, Vest. Elektroprom., 34. 74 (1963).

65. E. Frąckowiak, K. Jurewicz, in: F. Lapicque, A. Storck, A. A Wragg (Eds.), Electrochemical Engineering and Energy, Plenum, New York, P. 41 (1994).

66. J.-S. Chen, L.-F- Wang: Evaluation of calcium-containing zinc electrodes in zinc/silver oxide cells, J. Appl. Electrochem., 26, 227 (1996).

67. J. McBreen, E. G. Gagnon: Bismuth oxide as an additive in pasted zinc electrodes, J. Power Sources, 15, 169-177 (1985).

68. L. Yu Gun' ka, N. G. Nikhalenko, V. N. Flerov, Zh. Prikl. Khim., 54, 77 (1981).

69. J. McBreen, E. G. Gagnon: The electrochemistry of metal oxide additives in pasted zinc electrodes, Electrochim. Acta, 26, 1439-1446 (1981).

70. N. Kanani; Electroplating, Elsevier (2004).

71. Mc Breen, J. and Cairns, E., J.: The zinc electrode, in advanced electrochemistry and electrochemical engineering, Vol. 11, H. Gerischer and C. W. Tobias (eds), PP. 273-352, john Wiley & Sons, New York (1978).

72. V. V. Romanov, Zhur. Priklad. Khim., 34, 2692 (1961).

73. R. A. Despic and R. A. Popov: The effect of pulsating potential on the morphology of metal deposits obtained by mass-transport controlled electrodeposition, J. Appl. Electrochem., 1, 275-278 (1971).

74. V . V. Romanov, Zhur. Priklad. Khim., 36, 1050 (1963).

75. R. D. Naybour: The effect of electrolyte flow on the morphology of zinc electrodeposited from aqueous alkaline solution containing zincate ions, J. Electrochem. Soc., 116 520 (1969).

76. E. D. Woumfo, and O. Vittori: Electrochemical behaviour of a zinc electrode in 8 M KOH under pulsed potential loading, J. Appl. Electrochem., 21, 77-83 (1991).

77. F. Mansfeld and S. Gilman: The Effect of Tin and Tetraethylammonium Ions on the Characteristics of Zinc Deposition on a Zinc Single Crystal in KOH, J. Electrochem. Soc., 117 1154 (1970).

78. C. Cachet, Z. Chami and R. Wiart: The kinetics of zinc deposition at low overpotentials in alkaline electrolytes, Electrochim. Acta 33, 405-416 (1987).

79. C. W. Lee, K. Sathiyanarayanan, S. W. Eom, H. S. Kim, M. S. Yun: Novel alloys to improve the electrochemical behavior of zinc anodes for zinc/air battery, J. Power Sources 159, 1474-1477 (2006).

80. J. Zhu, Y. Zhou, C. Gao: Influence of surfactants on electrochemical behavior of zinc electrodes in alkaline solution, J. Power Sources 72, 231-235 (1998).

81. J. O. Bockris, K. N. Reddy, and M. Gamboa-Aldeco: Modern Electrochemistry2A, 2nd Edition, Kluwer Academic/Plenum Publishers.

82. P. Kritzer, and J.A. Cook: Nonwovens as separators for Alkaline Batteries, J. Electrochem. Soc., 154 (5) A481-A494 (2007).

83. P. Arora, and Z. Zhang: Battery separators, Chem. Rev., 104, 4419-4462 (2004).

84. A. J. Bard and L. R. Faulkner, editors. Electrochemical methods. Wiley, New York (1980).

85. V.S. Bagotsky, editors. Fundamental of Electrochemistry. Wiley, New Jersey (2006).

86. J. R. Macdonald, editor. Impedance spectroscopy. Wiley, New York (1987).

87. D.S Ballantine et al.: Acoustic wave sensor theory, design and physico-chemical applications, Academic Press (1996).

88. Lu and O. Lewis: Investigation of film-thickness determination by oscillating quartz resonators with large mass load, J. Appl. Phys. 43, 4385 (1972).

89. C. Gabrielli et al.: Calibration of the electrochemical quartz crystal microbalance, J. Electrochem. Soc. 139, 2657 (1991).

90. J.O. Bockris et al.: Modern Electrochemistry (2nd Edition), KA/PP, New York (2000).

91. B. Szczesniak, M. Cyrankowska, A. Nowacki: Corrosion kinetics of battery zinc alloys in electrolyte solutions, J. of Power Sources 75,130 – 138 (1998).

92. L. Binder and K. Kordesch: Corrosion of zinc electrode mixtures in alkaline media, J. Electroanal Chem, 180, 495-510 (1984).

93. R.E.F Einerhand, W.H.M.Visscher and E. Barendrecht: Hydrogen production during zinc deposition from alkaline zincate solutions, J. Appl Electrochem 18, 799-806 (1988).

94. K.D. Song, K-B. Kim, S-H. Han, and H. Lee: ElectroChem and Solid State Letters, 7 (2) C20-C24 (2004).

95. T. Trisovic et al: Kinetics of the hydrogen evolution reaction on zinc in sulfate solutions, J. Serb. Chem. Soc. 66 (11/12) 811 – 823 (2001).

96. J. Janata: Principal of Chemical Sensors, Springer (1989).

97. A. Milchev; ElectroCrystallization, Springer Publisher (2002).

98. N. Kanani; Electroplating, Elsevier (2004).

99. T. M. Dantan, R. A. Jones : Alkaline zinc battery having improved shelf-life, United States Patent 4948684.

100. R. Glicksman and C. K. Morehouse: An investigation of the discharge characteristics of groups Ib-Vb oxides in an alkaline electrolyte, J. Electrochem. Soc. 104, 589 (1957).

101. T. L. Broswell: Indium as an Anode Material, J. Electrochem. Soc., Volume 105, Issue 5, pp. 239-241 (1958).

102. A. N. Campbell: The passivity and overvoltage during hydrogen evolution and indium deposition of metallic indium, Can. J. Chem. 55, 1710 (1977).

103. S. B. Saidman, E. C. Bellocq and J. B. Bessone: Stationary and non-stationary electrochemical response of polycrystalline indium in alkaline media, Electrochim. Acta, Vol. 35, 329-338 (1990).

104. A. El Sayed, S. A. El Rehim and H. Mansour: Electrochemical behavior of an indium electrode in concentrated KOH solutions, Chem. Monthly, 122, 1019-1027 (1991).

105. G. M. Budov, V.V. Losev, Dokl. Akad. Nauk. S.S.S.R. 129:6 (1959).

106. R. D. Amstrong, A. B. Suttie, H. R. Thirsk: The electrochemical behaviour of indium amalgams in alkaline solutions, Electrochim. Acta 13, 1 (1968).

107. Yoshizawa, et al.: Method of manufacturing zinc-alkaline batteries, US Patent 5168018 (1991).

108. E.N. Deichman: Study of the properties of indium hydroxide, and the separation of indium from zinc, Russian Chem. Bulletin, 7, 245-252 (1958).

109. H. Zhou, M. Xu, Q. Huang, Z. Cai, W. Li : Anodic behavior of indium in KOH solution, J. Appl. Electrochem. vol. 39, 1739-1744 (2009).

110. L.C.A Thompson, R. Pacer : The solubility of indium hydroxide in acidic and basic media at 25°C, J. Inorg. Nucl. Chem., vol. 25, 1041-1044 (1963).

111. M.-B. Liu, G. M. Cook, and N. P. Yao: Galvanostatic Polarization of Zinc Microanode in KOH Electrolytes, ANL/OEPM-80-1 (1980).

112. R. D. Armstrong and M. F. Bell, Electrochemistry, Vol. 4, Ch. 1. Chemical Society, H R Thirsk, London (1974).

113. R. J. Brodd, and V. E. Leger, Encyclopedia of the Electrochemistry of the Elements, Vol. 5, Ch. V-1.

114. N. A Hampson, M. J. Tarbox, and J. T. Lilley, J. Electrochem. Technol., 2, 1811 (1977).

115. G. O. H. Whillock, B. F Harvey: Ultrasonically enhanced corrosion of 304L stainless steel II: The effect of frequency, acoustic power and horn to specimen distance, Ultrason. Sonochem. 4, 33-38 (1997).

116. A. Al-Ashem, P. G. Gaceres, W. T. Riad, H. M. Shalaby: Cavitation corrosion behaviour of cast nickel aluminium bronze in sea water, Corros. Sci. 51, 331 (1995).

117. V. Ligier, J. Y. Hihn, M. Wery, M. Tachez: The effects of 20 kHz and 500 kHz ultrasound on the corrosion of zinc precoated steels in [Cl^-] [$SO^{2-}{}_4$] [$HCO^-{}_3$] [H_2O_2] electrolytes, J. Appl. Electrochem., 31, 213-222 (2001).

118. M. L. Doche, J. Y. Hihn, F. Touyeras, J. P. Lorimer, T. J. Mason, M. Plattes : Electrochemical behaviour of zinc in 20 kHz sonicated NaOH electrolytes, Ultrason. Sonochemistry, 8, 291-298 (2001).

119. D. J. Walton, S. S. Phull, Adv. Sonochem., 4, 205-284 (1996).

120. Y. Chang, and G. Prentice: A model for the anodic dissolution of the zinc electrode in the prepassive region, J. Electrochem. Soc., 136, 3398-3403, (1989).

121. T. I. Popova, N. A. Simonova, and B. N. Kabanov, Elektrokhimiya, 3, 1419 (1967).